

National Central University

國立中央大學

Taiwan International Graduate Program
Earth System Science
地球系統科學國際研究生博士學位學程

Doctoral Dissertation
博士論文

**Improving Quantitative Precipitation
Forecast by Assimilating
the Retrieved Moisture and Radar Data**

**同化反演的水氣和雷達資料改善定量
降水預報**

Author (研究生): Do Thi Phuong Nghi (杜芳宜)

Advisors (指導教授): Professor Kao-Shen Chung (鍾高陞教授)
Professor Pay-Liam Lin (林沛練教授)

June 2022
中華民國 111年 6 月

National Central University

Taiwan International Graduate Program Earth
System Science

Doctoral Dissertation

Improving Quantitative Precipitation
Forecast by Assimilating
the Retrieved Moisture and Radar Data

Author: Do Thi Phuong Nghi

Advisors: Professor Kao-Shen Chung

Professor Pay-Liam Lin

June 2022

© Do Thi Phuong Nghi

National Central University Library Authorization for Thesis/ Dissertation

Application Date : 2022 / 07 / 13

The latest version since Sep. 2019

Applicant Name	Do Thi Phuong Nghi	Student Number	105621602
Schools / Departments	National Central University/International Ph.D. Graduate Program for Earth System Science	Graduate Degree	<input type="checkbox"/> Master <input checked="" type="checkbox"/> Doctor
Thesis/Dissertation Title	Improving Quantitative Precipitation Forecast by Assimilating the Retrieved Moisture and Radar Data	Advisor Name	Prof. Kao-Shen Chung Prof. Pay-Liam Lin

Authorization for Internet Access of Thesis/ Dissertation

This license authorizes my complete electronic thesis to be archived and read in the

- National Central University Library Electronic Theses & Dissertations System .

- () Released for Internet access immediately
 Released for Internet access starting from: 2022 / 12 / 31 (YYYY / MM / DD)
 () Disagree, because: _____

- NDLTD(National Digital Library of Theses and Dissertations in Taiwan).

- () Released for Internet access immediately
 Released for Internet access starting from: 2022 / 12 / 31 (YYYY / MM / DD)
 () Disagree, because: _____

I hereby agree to authorize the electronic versions of my thesis/dissertation and work to National Central University, University System of Taiwan(UST) and National Central Library(National Digital Library of Theses and Dissertations in Taiwan), in a non-exclusive way and without reimbursement, in accordance with the Copyright Act. The fore-mentioned authorized items can be reproduced by the authorized institution in the form of text, video tape, audio tape, disc and microfilm, or converted into other digital formats, without the limitation of time, places, and frequency for non-commercial uses.

Delayed Public Release for Paper Copy of Thesis/Dissertation

(You do not need to fill out this section if you make the paper copy of your thesis/dissertation available to the public immediately.)

- Reasons for the delayed release (choose one)

- () Filing for patent registration. Registration number: _____
 Submission for publication
 () Your research contains information pertaining to national non-disclosure agreements.
 () Contents withheld according to the law. Please specify _____

- Delayed Until : 2022 / 12 / 31 (YYYY / MM / DD)

You should submit another paper copy to National Central Library (NCL) through the NCU Division of Registrar. If you would like to delay the release of this paper copy in NCL, please fill out the "Application for Embargo of thesis/dissertation" of NCL.

Signature of the Applicant : Do Thi Phuong Nghi

Signature of the Advisor : Pay-Liam Lin

*Please attach this form after the thesis/dissertation cover when submitting your thesis/dissertation.

國立中央大學送存國家圖書館紙本論文延後公開說明書
Application to the National Central Library for Deferring the Public Access to the Thesis/Dissertation

姓名 Name	杜芳宜 (Do Thi Phuong Nghi)	學年 Academic Year	110	學期 Semester	2
學號 Student ID No.	105621602	系所 Department/Institute	International Ph.D. Graduate Program for Earth System Science	電話 Phone Number	0966775134

依教育部107年12月5日教高電二字第1070210758號函及109年3月13日教高電字第1090027810號函 請速將延後論文送交本館辦理並由學校簽發延後公開證明
認定之證明文件，經由學校向國家圖書館提出申請，無效認定證明由學校簽發即可處理
Per Official Document No. 1070210758 of the Division of Educational Quality and Development in the Department of Higher Education (DHE) at the Ministry of Education (MOE) issued on Dec. 5, 2018, and Official Document No. 1090027810 (General) of the DHE at the MOE issued on Mar. 13, 2019, please fill out this application form according to facts and attach the documentation acknowledged by your university or a review institute to this form. Submit this form to your university and the university will submit it to the National Central Library. Any application form without the seal of an institute that has conducted a review on this application will be directly returned to the applicant.

請詳細述明論文延後公開的理由。 Please describe in detail the reason why you need to defer the public access to your dissertation.
Submit paper.

簽章 Signature & Seal

學生簽章 Student's Signature	指導教授簽章 Advisor's Signature	系所章戳 Department/Institute's Seal

相關條文 Related Rules

1. 學位授予法第16條 Article 16 of the Degree Conferral Act

取得博士、碩士學位者，應將其取得學位之論文、書面報告、技術報告或專業實務報告，經由學校以紙本、錄影帶、錄音帶、光碟片或其他電子檔案方式，連同電子檔送交國家圖書館及所屬學校圖書館備查。

國家圖書館保存之博士、碩士論文、書面報告、技術報告或專業實務報告，應是供公眾閱覽之紙本，或透過電子設備讀取電子檔案；經作者同意後，得為複製、透視、影印、錄音、錄影、數位化、公開傳輸、或其他資訊傳播之行為。但涉及機密、專利事項或依法不得揭露，並經學校同意者，得不符提供閱覽之一定期間內不得提供。 A person who obtains a doctoral or master's degree shall give their university a copy of the thesis or dissertation, written report, technical report, or professional practice report which they submitted for the degree to send to the National Central Library and the university's library for storage, as a document, videotape, cassette, disc or in some other form, and they shall also provide an electronic file version. A copy of the dissertation, thesis, written report, technical report, or professional practice report stored by the National Central Library shall be made available to the public to read within the library in print form or by accessing electronic data files using independent equipment. If authority has been given in accordance with the provisions of the Copyright Act such stored items may be reproduced, publicly transmitted inside or outside the library using a network, or handled or used in other ways that are subject to copyright. If, however, the content involves confidential information, patent matters, or is not permitted to be provided on statutory grounds and this has been confirmed by the university, the person is permitted to not provide a copy or public access to the material in question will be placed under embargo for a certain period.

2. 學位論文送存國家圖書館典藏作業要點 Operation Guidelines for the Archiving of Dissertations at the National Central Library

第5點 各校送交本館之學位論文，依學位授予法第十六條規定，應是供公眾閱覽之紙本，或透過電子設備讀取電子檔案；但涉及機密、專利事項或依法不得揭露，並經學校同意者，得不符提供閱覽之一定期間內不得公開。

Point 5 Per Article 16 of the Degree Conferral Act, each dissertation sent by each university to the National Central Library for archiving should come with both a hard and a soft copy for readers to read at the library or to access with an independent device. However, if a dissertation involves confidential information, patent matters, or is not permitted to be provided on statutory grounds and this has been confirmed by the university of the dissertation's author, the author may apply for the nondisclosure of the dissertation or the deferring of public access to the dissertation.

第6點 延後公開申請書，經研究生及指導教授簽章，學校簽發延後公開證明，並檢附證明文件，經由學校向本館提出申請，必要時本館人員可逕向學校查詢處理。

Point 6 This application form should be signed by the applicant and his or her thesis advisor and be affixed a seal by an institute at the applicant's university that has conducted a review on this application. Relevant documentation should also be attached to this form. The applicant should submit this form to his or her university, and then the university will file this application to the National Central Library. The National Central Library may return this application form to the university for reprocessing if need be.

3. 國立中央大學研究生畢業論文格式條例 Thesis Format Regulations of NCU

註冊組代收之紙本論文，將送存國家圖書館，如需延後公開者，須裝訂延後公開申請書，檢附之證明文件請夾附於論文。

檢附證明文件說明如下列：

- 涉及機密：相關證明文件，或填寫本說明書。
- 專利事項：申請表填妥專利案號即可，若正在專利申請審核中，請附專利申請回覆影本。
- 依法不得提供：保密合約影本，或因論文投稿，有新技術發表先後之疑慮者，應填寫本說明書。

Theses and dissertations in printed form collected by the Division of Registrar will be sent to the National Central Library to be archived. If you need to defer the public access to your thesis or dissertation, you should bind the National Central Library's Application for Embargo on Thesis/Dissertation and your thesis/dissertation together and then insert this application into the bound thesis/dissertation along with related documentation (do not bind this application and your thesis together). The instructions on the related documentation are as follows:

- The thesis/dissertation contains national secrets: Please attach related documentation, or fill out this application form.
- Patent registration: Please fill in the patent registration number. If the applicant's patent application is being examined, please attach a copy of the reply concerning the patent application from the Intellectual Property Office.
- The thesis/dissertation is withheld according to the law: Please attach a copy of the non-disclosure agreement. If the author of the thesis/dissertation has concerns in the timing sequence of paper publication or new technology announcement, please fill out this application form.

國家圖書館學位論文延後公開申請書

Application for Embargo of Thesis/Dissertation

申請日期：民國_____年_____月_____日

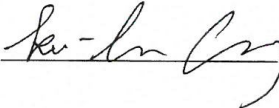
Application Date: 2022 / 7 / 13 (YYYY/MM/DD)

申請人姓名 Applicant Name	杜芳宜 (Do Thi Phuong Nghi)	學位類別 Graduate Degree	<input type="checkbox"/> 碩士 Master <input checked="" type="checkbox"/> 博士 Doctor	畢業年月 Graduation Date (YYYY/MM)	民國 2022 年 6 月
學校名稱 University	National Central University		系所名稱 School/Department	International Ph.D. Graduate Program for Earth System Science	
論文名稱 Thesis / Dissertation Title	Improving Quantitative Precipitation Forecast by Assimilating the Retrieved Moisture and Radar Data				
延後公開原因 Reason for embargo	<input type="checkbox"/> 涉及機密 Contains information pertaining to the secret. <input type="checkbox"/> 專利事項，申請案號： Filing for patent registration. Registration number: <input checked="" type="checkbox"/> 依法不得提供，請說明：Submit paper Withheld according to the law. Please specify.				
申請項目 Options	<input checked="" type="checkbox"/> 紙本論文延後公開 Delay public access to the printed copies of my thesis, but leave the online bibliographic record open to the public.			<input type="checkbox"/> 書目資料延後公開 Delay public access to online bibliographic record of my thesis.	
公開日期 Delayed Until	民國_____年_____月_____日 2022 / 12 / 31 (YYYY/MM/DD)			<input type="checkbox"/> 不公開 Prohibited from public access.	

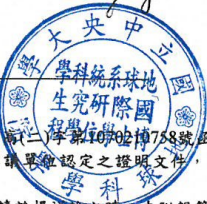
申請人簽名：

Applicant Signature: 

指導教授簽名：

Advisor Signature: 

學校認定/審議單位章戳：

Seal of the Authorization Institute: 

【說明】

- 依教育部107年12月5日臺教高(二)字第1070210758號函及109年3月13日臺教高通字第1090027810號函，請據實填寫本申請書並檢附由學校認定或審議單位認定之證明文件，經由學校向本館提出申請，無認定或審議單位章戳者退回學校處理。
- 論文尚未送交國家圖書館，請於提送論文時，夾附親筆簽名申請書1份。
- 論文已送交國家圖書館，請將親筆簽名申請書一式2份掛號郵寄10001臺北市中山南路20號國家圖書館館藏發展及書目管理組，並於信封註明「學位論文延後公開申請書」。
- 本館保存之學位論文依學位授予法應提供公眾於館內閱覽紙本，或透過獨立設備讀取電子資料庫，二者依表單填寫日期公開。

【Notes】

- Please fill in all blanks and attach the certification documents approved by the university and apply through the university. The application form will not be accepted for processing until all information, signatures, and stamps are included.
- If the thesis or dissertation is not yet submitted to the NCL, please attach the signed application form to the thesis or dissertation.
- If the thesis or dissertation has been submitted to the NCL, please send a registered letter with 2 copies of the signed application form attached. The letter should be addressed to "Collection Development Division", National Central Library with a note in the envelope indicating "Application for delay of public release" to the following address. No.20, Zhongshan S. Rd., Zhongzheng District, Taipei City 10001, Taiwan (R.O.C.)
- The delayed date of printed copies and the independent viewing equipment will synchronize.

(申請者免填，以下由國家圖書館填寫 For Internal Use)

承辦單位_館藏組：_____ 日期/處理狀況：_____

典藏地：_____ 登錄號：_____ 索書號：_____

會辦單位_知服組：_____ 日期：_____ 移送並註記，原上架日期：_____

論文系統：_____ 日期：_____

國立中央大學博士班研究生

論文指導教授推薦書

TIGP-ESS 學系/研究所 Do Thi Phuong

Nghi 研究生所提之論文 Improving Quantitative
Precipitation Forecast by Assimilating the Retrieved
Moisture and Radar Data 係由本人指導撰述，同
意提付審查。

指導教授 鍾高陞 (簽章)

111年6月6日

National Central University

Advisor's Recommendation for Doctoral Students

This thesis is by Do Thi Phuong Nghi of the graduate program in Taiwan International Graduate Program - Earth System Sciences, entitled: Improving Quantitative Precipitation Forecast by Assimilating the Retrieved Moisture and Radar Data, which is written under my supervision, and I agree to propose it for examination.

Advisor  鍾高陞

2022/06/06 (YYYY/MM/DD)

National Central University

Verification Letter from the Oral Examination Committee
for Doctoral Students

This thesis titled Improving Quantitative Precipitation Forecast by Assimilating the Retrieved Moisture and Radar Data, is written by Do Thi Phuong Nghi (杜芳宜) studying in the graduate program in TIGP-ESS (地球系統科學國際研究生博士學位學程). The author of this thesis is qualified for a Doctoral degree through the verification of the committee.

Convener of the Degree Examination Committee

楊舒芝 (Shu-Chih Yang)

Members

廖宇慶 (Yu-Ching Liao)

楊舒芝 (Shu-Chih Yang)

邱沛練 (Pey-Liam Tzu) 鍾高陞 (Kuo-Sheng Chung)

Date: 2022/06/27
(YYYY/MM/DD)

National Central University

Verification Letter from the Oral Examination Committee
for Doctoral Students

This thesis titled Improving Quantitative Precipitation Forecast by Assimilating the Retrieved Moisture and Radar Data, is written by Do Thi Phuong Nghi (杜芳宜) studying in the graduate program in TIGP-ESS (地球系統科學國際研究生博士學位學程). The author of this thesis is qualified for a Doctoral degree through the verification of the committee.

Convener of the Degree Examination Committee

Members



Date: 2022/06/27

(YYYY/MM/DD)

1080618

National Central University

Verification Letter from the Oral Examination Committee
for Doctoral Students

This thesis titled Improving Quantitative Precipitation Forecast by Assimilating the Retrieved Moisture and Radar Data, is written by Do Thi Phuong Nghi (杜芳宜) studying in the graduate program in TIGP-ESS (地球系統科學國際研究生博士學位學程). The author of this thesis is qualified for a Doctoral degree through the verification of the committee.

Convener of the Degree Examination Committee

Members

Chiayi Lu 劉千義

Date: _____

(YYYY/MM/DD)

1080618

Publications and presentations

Peer-reviewed publications

1. Do, Phuong-Nghi, K.-S. Chung, P.-L. Lin, C.-Y. Ke, and S. M. Ellis: Assimilating Retrieved Water Vapor and Radar Data From NCAR S-PolKa: Performance and Validation Using Real Cases. *Mon. Wea. Rev.*, **150**, <https://doi.org/10.1175/MWR-D-21-0292.1>
2. Do, Phuong-Nghi, K.-S. Chung, Y.-C. Feng, P.-L. Lin, B.-A. Tsai: Impact of Radar-Derived Refractivity Assimilation on the Quantitative Precipitation Forecast: Real Cases Study of SoWMEX. (in preparation)

Presentations

1. Do, Phuong-Nghi, K.-S. Chung, P.-L. Lin, C.-Y. Ke, and S. M. Ellis, 12/2021: Assimilating Retrieved Water Vapor and Radar Data From NCAR S-PolKa: Performance and Validation Using Real Cases, *2021 2nd KNU CARE Conference on Radar Meteorology*.
2. Do, Phuong-Nghi, K.-S. Chung, P.-L. Lin, S. M. Ellis, Ya-Chien Feng, 03/2022: Improving The Heavy Rainfall Forecast by Assimilating Retrieved Moisture and Radar Data: Performance and Validation With Real Cases, *International Conference on Heavy Rainfall and Tropical Cyclone in East Asia*.
3. Do, Phuong-Nghi, K.-S. Chung, P.-L. Lin, C.-Y. Ke, and S. M. Ellis, 6/2022: Assimilating Retrieved Water Vapor and Radar Data From NCAR S-PolKa: Performance and Validation Using Real Cases, *TGA-2022 Atmospheric Science Graduate Conference*.
4. Do, Phuong-Nghi, K.-S. Chung, P.-L. Lin, C.-Y. Ke, and S. M. Ellis, 8/2022: Assimilating Retrieved Water Vapor and Radar Data From NCAR S-PolKa: Performance and Validation Using Real Cases, *Asia Oceania Geosciences Society Annual Meeting 2022*.

同化反演的水氣和雷達資料改善定量降水預報

中文摘要

如何改進劇烈天氣系統之定量降水預報是數值預報持續關注的議題與挑戰。而水氣場在對流系統當中為相當重要的資訊。同化都卜勒風與回波資料對提升數值預報有相當程度的改善，但在調整水氣場以獲得最佳分析場與數值預報上有其限制。本論文旨在研究同化掃描式雷達所反演兩種不同類型的水氣資訊，包括 S-PolKa 雙波長反演的垂直剖面水氣與雷達折射指數反演的近地表二為水氣資訊。

本研究第一部分將S-PolKa反演得到低層降水系統周圍的垂直剖面水氣資訊，與雷達回波和都卜勒風一起進行同化。採用 WRF 局地系集轉換卡爾曼濾波資料同化系統，在 Dynamics of the Madden-Julian Oscillation Experiment (DYNAMO)觀測實驗的三個真實個案進行一系列實驗測試。同化時，濕度的垂直剖面被分為平均後之單點單一剖面 and 四個象限上分別提供水氣剖面資訊，並在 1) 與連續 2 小時的雷達資料和 2) 在第一小時單獨同化水氣資訊，然後在第二小時接著同化徑向風和回波。結果顯示，與僅同化雷達資料相比，額外同化水氣資訊顯著地改進了對流尺度的分析場，進而提升定量降水預報的表現。此外，策略上第一小時僅同化水氣資料，而後於第二小時同化徑向風和回波資料其結果呈現出最佳之分析場，且與其他實驗相比，定量降水預報的改進最大。而同化時若將水氣剖面分為四個象限在分析場和預報結果上會更加理想。

本論文的第二部分重點研究同化能代表地表附近水氣資訊的雷達折射指數。利用西南季風觀測實驗中的兩個真實個案，採用高解析度 WRF 局地系集轉換卡爾曼濾波器資料同化系統。測試兩組不同的實驗。在第一組實驗中，探討額外同化雷達折射指數反演水氣之影響。結果顯示，同化反演進地表之水氣除了調整水氣分布之外，也同時增強風場的輻合作用，改進定量降水預報的能力。此外，同化折射指數的影響，取決於背景場之情況，也就是在具有更廣泛折射指數分佈且偏乾背景水氣場中，效果尤為顯著。第二組實驗主要在測試天氣系統著陸前後同化折射指數的效益。結果顯示，降水系統登陸島上後，持續同化雷達折射率對短期預報具有優勢。此外，測試結果亦建議於天氣系統登陸之前便開始同化折射指數，能獲得最佳的定量降水預報表現，尤其在強降雨的區域更為顯著。

Improving Quantitative Precipitation Forecast by Assimilating the Retrieved Moisture and Radar Data

Abstract

Improving the quantitative precipitation forecast is the key ongoing challenge in weather prediction. Despite the positive impact on the enhancement of numerical weather prediction, the assimilation of reflectivity and radial velocity cannot fully adjust the water vapor field to achieve an optimal short-term forecast. However, moisture information is proved to be critical for convection analysis and forecast. This thesis aims to investigate the additional assimilation of two different kinds of moisture data including the S-PolKa-retrieved water vapor and radar-retrieved refractivity.

In the first part of this dissertation, the S-PolKa-retrieved water vapor data which represents the environmental information outside the precipitation at the low level was assimilated with reflectivity and radial wind. The WRF local ensemble transform Kalman filter data assimilation system was employed to examine a series of experiments in three real cases of the Dynamics of the Madden-Julian Oscillation Experiment. The vertical profiles of humidity were thinned into one averaged and four-quadrant profiles and assimilated 1) with radar data for the entire 2 h and 2) alone in the first hour, followed by radial wind and reflectivity assimilation in the second hour. The results revealed that assimilating additional water vapor data more markedly improved the analysis at the convective scale, leading to more significant improvements in the rain forecast compared with assimilating radar data only. In addition, the strategy of assimilating only retrieved water vapor data in the first hour and radial wind and reflectivity data in the second hour achieved the optimal analysis, resulting in the most improvement in rain forecast compared with other experiments. Furthermore, assimilating moisture profiles into four quadrants achieved more accurate analyses and forecasts.

The second part of this dissertation focus on examining the assimilation of radar-retrieved refractivity which carries moisture information near the surface. Two real cases in the Southwest Monsoon Experiment were deployed with the high-resolution WRF

local ensemble transform Kalman filter data assimilation system. Two different sets of experiments were investigated. In the first experimental group, the role of extra refractivity assimilation was investigated. The results indicated that additional refractivity assimilation improved the quantitative precipitation forecasting by generating the optimal moisture, temperature, and wind adjustment and enhancing the wind convergence. Moreover, the level impact of refractivity assimilation on the short-term forecast is markedly notable in dry-biased background moisture with broader refractivity distribution. The second experimental set was utilized for studying the refractivity assimilation before and after the weather system landed. The results revealed that assimilating radar refractivity continuously after the precipitation system landed on the island has advantages for the short-term forecast. Additionally, this study suggested starting assimilating refractivity before the weather system landed to obtain the optimal quantitative precipitation forecasting, particularly for heavy rainfall.

Acknowledgements

I would like to express my deeply grateful to my major advisor, Professor Kao-Shen Chung, for his enthusiastic instruction and enormous support throughout my Ph.D. study. I appreciate his open-minded and abundant patience that let me have creative thinking in designing the experiments and explaining the research results. He also took me back in the right direction every time I got lost in my research. I would not forget to send my thanks to my co-advisor, Professor Pay-Liam Lin, for his financial support and enormously encouragement. Without their guidance and funding, this thesis would not have been completed.

Many sincere thanks to Professor Yu-Chieng Liou and Professor Wei-Yu Chang in Radar Meteorology Laboratory for their kindly encouragement, and helpful comments in the group meeting, which inspired plentiful great research ideas for me. Besides, I always feel lucky and grateful to have opportunities to collaborate with Dr. Scott M. Ellis and Dr. Ya-Chien Feng. My knowledge was broadened and my research skills were improved by their comprehensive comments and correction of my works.

I would like to take this opportunity to say thanks to my friends and colleagues from the Radar Meteorology Laboratory for giving me a working place fulfill with interesting and fantastic. They are always willing to share their experiences and help me to solve the difficulties during my research. Much particularly thanks send to Haidy, Chieh-Ying, Xiao-Na, and Xiao-Yu, our “girl-dorm” members in the Radar lab, who together shared both stress and happy time with me as my sisters. My heartfelt thanks to my good friends Mai-Han, Hien Bui, Lan-Phuong, Trong-Hoang, and Lien Nguyen, who kept patient to share my frustrations and gave me lots of useful advice.

From bottom of my heart, I would like to thank Taiwan International Graduate Program (TIGP) at Academia Sinica and National Central University to give me a chance to study in such a beautiful and friendly country. Special thanks to our secretaries Yuwen and Catherine for helping me to handle a bunch of documents related to the administrative tasks.

This acknowledgment cannot end without sending my most sincere thanks to my Dad, Mom, older sister, and brothers who always unconditionally trust in me with their endless love. I also greatest thanks to my sister-in-law and my cutest nephews and nieces. Thank you for staying by my side and encouraging me to pursue my dream.

Contents

中文摘要.....	i
Abstract	ii
Acknowledgements.....	iv
Contents.....	v
List of Figures.....	viii
List of Tables.....	xiii
Chapter 1 Introduction	1
1.1 Overview of radar assimilation	1
1.2 Limitation of radar assimilation in moisture correction.....	3
1.3 Overview of assimilating moisture information based on radar	4
1.4 Motivation and goals of the study	5
1.5 Dissertation outline	7
Chapter 2. Assimilating Retrieved Water Vapor and Radar Data From NCAR S- PolKa: Performance and Validation Using Real Cases.....	8
2.1 Introduction	9
2.2 Assimilation system and data description	11
2.2.1 WRF-Local ensemble transform Kalman filter radar assimilation system	11
2.2.2 Model configuration.....	12
2.2.3 Radar observations	14
2.2.4 S-PolKa–retrieved water vapor density.....	14
2.2.5 Observation operator	15
2.3 Case description and experimental design	16

2.3.1	Description of the three study cases	16
2.3.2	Experimental design.....	18
2.4	Results of the analysis and forecast.....	23
2.4.1	Performance of the analysis	23
2.4.2	Performance of the short-term deterministic forecast	31
2.5	Summary and Conclusions	39
Chapter 3. Impact of Radar-Derived Refractivity Assimilation on the Quantitative Precipitation Forecast: Real Cases Study of SoWMEX		41
3.1	Introduction	42
3.2	Study cases and assimilation observations.....	44
3.2.1	The two heavy rainfall events of SoWMEX: 02 June and 14 June 2008..	44
3.2.2	Observations for assimilation.....	46
3.3	Assimilation system and experimental design	49
3.3.1	Model configuration.....	49
3.3.2	WRF-Local ensemble transformed Kalman filter Radar Assimilation System	51
3.3.3	Observation operators	51
3.3.4	Experimental design.....	52
3.4	Results.....	55
3.4.1	Data and methods for performance verification.....	55
3.4.2	Results of the first experimental set	56
3.4.2.1	Case 1: IOP 4.....	56
a.	<i>Results of the analysis</i>	56
b.	<i>Results of the forecast</i>	64
3.4.2.2	Case 2: IOP 8.....	67
a.	<i>Results of the analysis</i>	67

<i>b. Results of the forecast</i>	71
3.4.2.3 Comparison of the two cases.....	72
3.4.3 Results of the second experimental set	73
3.4.3.1 Assimilating refractivity before the precipitation system landed over the island (0300 UTC).....	73
3.4.3.2 Assimilating refractivity after the precipitation system landed over the island (0400 UTC).....	78
3.5 Summary and conclusions.....	80
Chapter 4 Conclusions and Future Work	82
4.1 General conclusions	82
4.2 Future Works.....	84
Bibliography.....	86

List of Figures

- Figure 2.1: (a) The WRF model domains. The black dot indicates the S-PolKa location. The horizontal grid spacing of domains 1, 2, and 3 are 27 km (131×129 points), 9 km (175×169 points), and 3 km (139×133 points), respectively. (b) The experimental design schematic. The triple dash lines represent the model spin-up period and the triple dotted lines and solid lines represent the ensemble forecast and data assimilation period, respectively. The single solid lines indicate the mean forecast. The vertical dash bars represent the assimilation cycles.13
- Figure 2.2: Hourly column maximum Z observation of the three cases. The first case (a, d, g, j, m, p) from 1600 to 2100 UTC 18 Oct 2011; the second case (b, e, h, k, n, q) from 0000 to 0500 UTC 16 Oct 2011; and the third case (c, f, i, l, o, r) from 1030 to 1530 UTC 12 Oct 2011. Two convective lines in the first case are denoted by two black boxes with the letters A and B. The encircled black cross indicates the S-PolKa location.17
- Figure 2.3: (a) The original S-PolKa-retrieved Q_v location for all levels. (b) and (d) The vertical profiles of one averaged Q_v profile and four-quadrant Q_v profiles (solid color lines), and the original retrieved Q_v values (black crosses). (c) and (e) The location of one averaged Q_v profile and four-quadrant Q_v profiles (black dot); the encircled blue cross indicates the radar location, and the red triangle represents the Gan sounding station. These figures are plotted at 0000 UTC 16 Oct 2011.....19
- Figure 2.4: The standard deviation (SD) between Q_v derived through the average profile method (i.e., one averaged Q_v profile) and four-quadrant method (i.e., northeast, southeast, southwest, and northwest) for the three study cases: 18 Oct 2011 (a–e), 16 Oct 2011 (f–j), and 12 Oct 2011 (k–o). The figures are plotted every 30 min in each case beginning from the first cycle.....20
- Figure 2.5: The BECRs estimated using the ensemble between Q_v and Q_v (a, d, g), Q_v and U (b, e, h), and Q_v and V (c, f, i) at 1 km, with the S-PolKa location (encircled black cross) serving as the reference point for the first case (a–c), second case (d–f), and third case (g–i). The correlations are presented at the time of the first cycle before assimilation.21
- Figure 2.6: The Q_v analysis increment at 1 km at the first cycle for the first case (a–c), second case (d–f), and third case (g–i). The increments are from experiment

ZVr (a, d, g), ZVrQv_a (b, e, h), and ZVrQv_4q (c, f, i). The encircled black cross indicates the S-PolKa location.	24
Figure 2.7: RMSEs of Q_v verified against S-PolKa-retrieved Q_v across nine assimilation cycles for the three cases.	25
Figure 2.8: Column maximum Z (a–f). The difference between the observation and analysis mean of the Z at 1 km (g–l) at the final cycle of the first case (1800 UTC 18 Oct 2011). (a, g) NODA; (b, h) ZVr; (c, i) ZVrQv_a; (d, j) Qv_ZVr_a; (e, k) ZVrQv_4q; and (f, l) Qv_ZVr_4q. The encircled black cross indicates the S-PolKa location.	27
Figure 2.9: As in Fig. 2.8, but for the second case at 0200 UTC 16 Oct 2011.	28
Figure 2.10: As in Fig. 2.8, but for the third case at 1230 UTC 12 Oct 2011.	30
Figure 2.11: Accumulated 3-h rainfall from 1800 to 2100 UTC 18 Oct 2011 for the first case. Observation (a); ZVr (b); ZVrQv_a (c); Qv_ZVr_a (d); ZVrQv_4q (e); and Qv_ZVr_4q (f). The encircled black cross represents the S-PolKa location. The black boxes denote the more accurate heavy rain forecasts of Qv_ZVr_a and Qv_ZVr_4q compared with those of the other experiments.	32
Figure 2.12: As in Fig. 2.11, but for 3 h (from 0200 to 0500 UTC 16 Oct 2011) for the second case.	34
Figure 2.13: As in Fig. 2.11, but for 3 h (from 1230 to 1530 UTC 12 Oct 2011) for the third case.	35
Figure 2.14: The FSS score of the (a) 1-h, (b) 2-h, (c) 3-h, and (d) 4-h accumulated rainfall. Scores are averaged across the three cases.	36
Figure 2.15: The 1–4-h RMSEs of the data assimilation experiments of (a) accumulated rainfall compared with surface rainfall at the Gan station; (b–e) the RH , T , U , and V compared with the Gan sounding station data, averaged for the entire profile; and (f) the Q_v compared with the S-PolKa-retrieved Q_v . The Q_v RMSE is only calculated for the third case; other RMSEs are averaged across the three cases.	38
Figure 3.1: The Quantitative Precipitation Estimation and Segregation Using Multiple Sensors (QPESUMs) observation of two cases: (a–h) the first case from 0200 to 0900 UTC 02 Jun 2008 and (i–p) the second case from 0800 to 1500 UTC 14 Jun 2008.	45
Figure 3.2: The 12-h accumulated rainfall of (a) the first case from 0000 to 1200 UTC 02 Jun 2008; (b) the second case from 0600 to 1800 UTC 14 Jun 2008.	46

Figure 3.3: (a) Example of radar data superobbing at 0.5 elevation angle; (b) Example of N superobbing; (c) Locations of sounding (encircled purple crosses) and surface (red crosses) stations utilized for forecast verification. The black stars in (a) and (c) denote the radar locations. These figures were plotted at 1000 UTC 14 Jun 2008.48

Figure 3.4: The N (color shading) and Z (> 40 dBZ, gray contours) observations (every 30 minutes) for two cases: (a–g) the first case from 0300 to 0600 UTC 02 Jun 2008 and (h–n) the second case from 0900 to 1200 UTC 14 Jun 2008.49

Figure 3.5: (a) The WRF model domains setting in this study. The horizontal grid spacing of domains 1, 2, 3, and 4 are 27 km (181×151 points), 9 km (166×157 points), 3 km (211×211 points), and 1 km (250×250 points), respectively. (b) The schematic of experiments design. The triple dash lines indicate the model spin-up period, the triple and single solid lines stand for the data assimilation period and the mean forecast, respectively. The vertical blue arrows denote Z and Vr observations, and the vertical red arrows refer to N observations utilized for assimilation.50

Figure 3.6: The background of Qv (a,b) and N (c,d) of the first case at 0400 UTC 02 June 2008 (a,c) and the second case at 1000 UTC 14 June 2008 (b,d); the N difference between the observation and the first case (e) and second case (f). These figures were plotted at the second eta model level.54

Figure 3.7: The analysis increments of Qv (a–b), T (c–d), and wind speed (e–f) at the first cycle of the first case (i.e., 0400 UTC 02 June 2008) for experiments ZVr_2h (a,c,e) and $ZVr\&N$ (b,d,f). The figures were plotted at the second eta model level. The three black dash lines with characters A and B indicate the cross-sectional location for Fig. 3.9.57

Figure 3. 8: The column maximum Z over 35 dBZ at the first cycle of the first case (i.e., 0400 UTC 02 June 2008; a,c,e) and the second case (i.e., 1000 UTC 14 June 2008; b,d,f). Observation (a–b), analysis of experiment ZVr_2h (c–d), analysis of experiment $ZVr\&N$ (e–f). The dash black boxes denote the more accurate Z analysis of $ZV\&N$ compared with ZVr_2h59

Figure 3. 9: Vertical cross-section of analysis increment of Qv (a–b), T (c–d), and wind speed (e–f) at the first cycle of the first case (i.e., 0400 UTC 02 June 2008) along 3 lines with characters A and B (illustrated in Fig. 3.7) for experiments ZVr_2h (a,c,e) and $ZVr\&N$ (b,d,f).60

Figure 3. 10: The difference between the observation and analysis mean of the N at the second eta model level at the first cycle of the first case (i.e., 0400 UTC 02 June 2008; a–b) and the second case (i.e., 1000 UTC 14 June 2008; c–d) for experiments ZVr_2h (a,c) and ZVr&N (b,d). The numbers in the black boxes denote the RMSEs of N compared with the observation.62

Figure 3. 11: The Qv ($g\ kg^{-1}$, color shading) and wind ($m\ s^{-1}$, arrows) analysis (a,b,e,f) and convergence field at 1.5 km (c,d,g,h) at the final cycle of the first case (i.e., 0600 UTC 02 June 2008; a–d) and the second case (i.e., 1200 UTC 14 June 2008; e–h) for experiments ZVr_2h (a,c,e,g) and ZVr&N (b,d,f,h). The figures were plotted at the second eta model level.63

Figure 3.12: The 3 h (a–c; g–i) and 6 h (d–f; j–l) accumulated rainfall from 0600 UTC 02 June 2008 of the first case (a–f) and 1200 UTC 14 June 2008 of the second case (g–l). Observation (a,d,g,j); ZVr_2h (b,e,h,k); ZVr&N (c,f,i,l).....65

Figure 3.13: The FSS during 6-h accumulated rainfall of the first case (i.e., 02 June 2008; a–d) and the second case (i.e., 14 June 2008; e–h) for thresholds 10 mm (a,e), 20 mm (b,f), 30 mm (c,g), and 40 mm (d,h).....66

Figure 3.14: The RMSEs of rainfall (a,b), N (c,d) during 6-h forecast, and Qv at 3- (e,f) and 6-h forecast (g,h) for the first case (i.e., 02 June 2008; a,c,e,g) and the second case (i.e., 14 June 2008; b,d,f,h).67

Figure 3.15: As in Fig. 3.7, but those for the second case (i.e., 1000 UTC 14 June 2008). The three black dash lines with characters C and D indicate the cross-sectional location for Fig. 3.16.69

Figure 3. 16: As in Fig. 3.9, but those for the second case (i.e., 1000 UTC 14 June 2008) along 3 lines with characters C and D (illustrated in Fig. 3.15).70

Figure 3.17: The second eta model level BECRs (a,b) and vertical BECRs (red curves; c,d) were estimated by the ensemble between N with Qv for the first case (a,c) and the second case (b,d). The correlations are computed and averaged for all the reference points inside the area denoted by the gray dash line in (a) at the time of the first cycle before assimilating. The cyan stars stand for the S-Pol radar.73

Figure 3. 18: As in Fig. 3.11, but those for the first case at 0500 UTC (a–d) and 0600 UTC (e–h) 02 June 2008 of experiments N_ZVr (a,c,e,g) and N_ZVrN (b,d,f,h). ..75

Figure 3. 19: The analysis of N of the first case at 0500 UTC (a,b) and 0600 UTC (c,d) 02 June 2008 for experiments N_ZVr (a,c) and N_ZVrN (b,d). The gray

contours denote the maximum Z values larger than 40 dBZ. The numbers in the black boxes denote the RMSEs of N compared with the observation. The figures were plotted at the second eta model level.76

Figure 3. 20: As in Fig. 3.12, but those accumulated from 0500 UTC (a–f) and 0600 UTC (g–l) 02 June 2008 of the first case. Observation (a,d,g,j); N_ZVr (b,e,h,k); N_ZVrN (c,f,i,l).77

Figure 3. 21: The FSS improvement rate (%) for 3-h (a) and 6-h (b) accumulated rainfall from 0500 UTC (orange columns) and 0600 UTC (green columns) 02 June 2008 of the first case for thresholds 10 mm, 20 mm, 30 mm, and 40 mm.78

List of Tables

Table 2.1: Summary of experiments, the symbols “_” and “x” indicate that the information was not assimilated and was assimilated, respectively.22

Table 2.2: Summary of study cases and time period settings for each case.23

Table 2.3: RMSEs of the Z , Vr (compared with S-band radar), and Qv (compared with S-PolKa–retrieved Qv) at the final analysis cycle for the three cases. The smallest RMSEs of these three variables in each case are indicated in bold font. ...31

Table 3.1: Summary of experimental design, symbols “x” and “—” denoted the observation was and was not included in the assimilation cycle, respectively.....55

Table 3.2: RMSEs of the Qv (g kg^{-1}), T (K), and wind speed (wspd ; m s^{-1}) compared with surface stations at the first analysis cycle for the two cases. The smaller RMSEs in each case are indicated in bold font.....58

Table 3.3: The RMSE improvement rate (%) of the N (N_{ZVrN} versus N_{ZVr}) from the sixth to ninth analysis cycle for the two assimilation periods. The higher improvement in each assimilation period is indicated in bold font.79

Chapter 1 Introduction

Weather radar provides valuable information about the three-dimensional structures of a meso- or convective-scale weather system with high temporal (every 5-10 min) and spatial resolution (a few hundred meters). Additionally, this instrument is capable of probing the kinematic and hydrometeor fields inside storms. Therefore, radar observations have been successfully applied for identifying, observing, and warning of severe storms and other hazardous events. The knowledge of the lifecycle, dynamics, and microphysical characteristics of convection could be obtained by relying on radar observations. Moreover, the radar observations of reflectivity (Z) and radial velocity (V_r) were proved to be advantaged for enhancing the numerical weather prediction (NWP) performance by being assimilated into various assimilation algorithms (Fabry and Meunier 2020).

However, the assimilation of Z and V_r has some limitations in the quantitative precipitation forecast. Such assimilation can only modify the moisture inside the precipitation system and may not obtain the optimal analysis to launch the short-term forecast. Moreover, Z and V_r information are only available after the convection begins to develop. In this chapter, the literature review of radar assimilation is presented in section 1.1, followed by the limitation of radar assimilation in correcting the moisture field in section 1.2. Section 1.3 gives an overview of assimilating moisture based on the radar data. The motivation and goals of this thesis are presented in section 1.4. The structure of the thesis is described in section 1.5.

1.1 Overview of radar assimilation

Data assimilation (DA) is a procedure to achieve the optimal initial condition for the NWP model by combining observation and short-range forecast. The high spatiotemporal resolution of radar data (Z and V_r) which can provide adequate information for the convective system has been successfully assimilated by using several DA approaches. Applying the complex cloud analysis schemes which is the simplest way to ingest radar data into the NWP. In this method, reflectivity is used to adjust the in-cloud moisture and temperature, resulting in spinup problem alleviation and short-term forecast improvement (Hu et al. 2006). The cloud analysis approach has the benefit of

saving the computation cost, but it bases only on the empirical relation that misses the forecast background information. Other DA methods include three- or four-dimensional variational DA (3DVAR or 4DVAR), ensemble Kalman filter (EnKF), and hybrid ensemble-variational also popular for applying radar data.

The 3DVAR (Sasaki, 1958) based on climatological background error covariances has been applied to assimilate radar observations in operational NWP systems for a long time because of its stability and saved computational cost (Lindskog et al. 2004; Montmerle and Faccani 2009). The benefits of 3DVAR radar assimilation on the short-term forecast were proved in many studies. Xiao et al. (2005) assimilated the V_r from a single radar in the framework of 3DVAR and indicated the improvement of rainband forecast generated by the Doppler velocity assimilation. The Z and V_r were implemented in the 3DVAR assimilation system in the studies of Xiao and Sun (2007) and Sugimoto et al. (2009). These studies showed that Z and V_r could adjust the hydrometeor and wind analysis, resulting in positive impacts on quantitative precipitation forecasting (QPF). Despite these benefits, the disadvantage of 3DVAR is that a static background error structure is assumed and utilized for the whole cycling process while at the convective scale, the structure of flow-dependent error has quick spatial and temporal variations (Chung et al. 2013; Jacques et al. 2017).

To overcome the above limitation, the 4DVAR (Dimet and Talagrand 1986) was introduced. This algorithm has been applied in radar data assimilation and showed the ability to produce more precise analyses by taking into account the flow-dependent forecast error. In the 4DVAR approach, the time dimension is added to the cost function to allow the model state and observation comparison. Sun and Crook (1997) developed the Variational Doppler Radar Analysis System (VDRAS) which assimilated radar data in the framework of 4DVAR. Various studies employed VDRAS in different real cases and indicated the improvement of convective scale forecast (Sun and Zhang 2008; Tai et al. 2011; Chang et al. 2014; Chang et al. 2016). The 4DVAR radar assimilation was also developed and applied in WRF (Sun and Wang 2013) and in the Japan Meteorological Agency (Kawabata et al. 2011). However, the drawback of 4DVAR is that it requires respectively running and developing a complex adjoint model which is computation and labor-intensive.

Besides the variational method, the EnKF (Evensen 1994) has gained broad attention in radar data assimilation. This method employs the cross-variable forecast error covariance defined from the ensembles to achieve the relation between the state

variables. The atmospheric uncertainty is estimated based on the multiple forecast and statistics of ensemble schemes without requiring any adjoint model and still maintain the flow-dependent error structures during the assimilation process. By utilizing the Gridpoint Statistical Interpolation-based DA system to assimilate radar and conventional observations, the comparison between EnKF and the 3DVAR was made in the study of Johnson et al. (2015). The results concluded that EnKF could generate better convection forecasts and persevere the prediction for a longer time than 3DVAR. For the comparison between EnKF and 4DVAR, the study of Caya et al. (2005) revealed that both approaches successfully produce the analysis, but the practical implementation of EnKF is easier than 4DVAR. Various studies successfully assimilated radar information in the EnKF system to improve the short-term forecast performance at the convective scale (Snyder and Zhang 2003; Zhang et al. 2004; Tong and Xue 2004; Aksoy et al. 2009; Yussouf and Stensrud 2010; Dowell et al. 2011; Tsai et al. 2014). Nevertheless, EnKF also has some issues. The spurious long-range correlation is caused by the severely ranked deficient because of the background error covariance matrix estimated from the limited ensemble (Hamill and Snyder 2000). Despite the prevention of the addition of long-range balance, covariance localization is a way to lessen this disadvantage.

Apart from the above assimilation approaches, a hybrid method (Hamill and Snyder 2000) was introduced by taking the benefit of the static and flow-dependent ensemble covariance shown to be effective for radar assimilation. In this method, the flow-dependent error covariance is obtained by combining the climatic background error achieved in 3DVAR and by ensemble members. The issues of not considering the real-time model error in 3DVAR and the sampling problem in EnKF can be solved by this method. Additionally, the hybrid method can reduce the computation cost compared with the EnKF system. The assimilation of radar data in a hybrid system was first evaluated by Gao et al. (2013). The authors pointed out that compared with EnKF, the hybrid method outperformed for the analysis of the hydrometer variables but underperformed the dynamic analysis when assimilating single radar data. The enhancement of QPF obtained by radar data assimilated through the hybrid method was proved in many studies (Li et al. 2015; Shen et al. 2016; Kong et al. 2018; Shen et al. 2020; Kong et al. 2020).

1.2 Limitation of radar assimilation in moisture correction

Despite the positive impact on the QPF, radar assimilation remains many

challenges in regards to improving the analysis and forecast of convective weather systems. Weather radar only provides the information on the wind field obtained by Vr and the hydrometeors distribution achieved by Z and dual-polarization observations. However, other model variables forecasted in the NWP model such as moisture and thermodynamic fields which are the main control of storm intensity are not directly observed by radar. Moreover, there is nonunique relationship between radar data (Z and Vr) and moisture variables. In 3DVAR radar assimilation, Z usually cannot generate moisture and temperature increments (Pan et al. 2020). For the EnKF, the radar operator does not contain moisture information. The moisture adjustment is essentially based on the ensemble-background error covariance between water vapor and simulated radar observations. However, this moisture correction only occurs inside the precipitation system and after the convection begins to develop. Fabry and Meunier (2020) also stated that the utilization of radar DA is difficult for temperature and humidity modification. The radar assimilation results in the notable correction of precipitation and wind component in the analysis, but the unobserved variables including temperature and humidity are only slightly updated from the background. Additionally, this updating occurs only inside or very nearby to the location of the precipitation system.

1.3 Overview of assimilating moisture information based on radar

Ge et al. (2013) conducted observing system simulation experiments (OSSEs) to assimilate various state variables, emphasizing the influential roles of humidity in addition to that of horizontal wind in storm analysis and forecast. The author also concluded that the moisture information is more efficient for reconstructing severe storms compared with hydrometeor variables. Taking into account the crucial role of water vapor information in convection forecast, several studies made efforts to assimilate the moisture information obtained from radar at convective scales.

An indirect radar reflectivity assimilation scheme was introduced by Wang et al. (2013). In this scheme, the authors assimilated retrieved rainwater and estimated in-cloud water vapor derived from Z instead of directly assimilating Z . The results revealed that both the location and intensity of convection were well forecasted in four heavy rain cases. Another method to assimilate moisture information relying on radar was employed in the studies of Caumont et al. (2010) and Wattrelot et al. (2014) named as 1D+3DVar method. In this method, the humidity is retrieved based on 1D Bayesian formalism and

the Z is assimilated into the 3DVar system. The results demonstrate the noteworthy improvement of the short-term forecast obtained by applying the 1D+3DVar method. Sun et al. (2020) conducted the assimilation of rainfall observed by radar and surface observation and proved the crucial role of assimilating rainfall in moisture and temperature correction. In contrast, the reflectivity assimilation only partially contributes to humidity correction. Alternatively, a semiempirical complex cloud analysis procedure is capable of modifying the temperature and humidity field (Hu et al. 2006; Pan and Wang 2019; Pan et al. 2020). These studies demonstrated that the semiempirical method could effectively analyze the in-cloud moisture field and resulted in the storm forecast improvement. Besides, Lai et al. (2019) introduced a way to retrieve vertically integrated liquid water based on three-dimensional reflectivity. This moisture information was then assimilated with Z and V_r and showed the ability to lessen the overprediction of storm cells.

1.4 Motivation and goals of the study

By using different assimilation approaches for assimilating various moisture information retrieved by radar, the aforementioned studies proved the positive impact of assimilating humidity information on QPF. However, the utilized moisture data are only available inside precipitation systems and after the development of convection. On the other hand, the minor variation in environmental humidity can lead to the significant modification of rain patterns and intensity (Fabry and Meunier 2020). The information on moisture surrounding the convection system is important for the storm initiation forecast because a change of moisture within 1 g kg^{-1} can determine the occurrence or nonoccurrence of storm initiation (Crook 1996).

Besides, the importance of near-surface moisture information for improving initial conditions in the storm-scale forecast was pointed out in many studies (Fabry and Sun 2010; Hanley et al. 2011; Ha and Snyder 2014; Madaus and Hakim 2016). A change in the low-level moisture can affect the time and location of convection initiation. Additionally, Weckwerth (2000) stated that the moisture measurement in the boundary layer requires a high resolution of spatial (100-m) and temporal (10-min). Nevertheless, the measurement for achieving such high-resolution moisture data is inadequate. The surface-based observing networks (i.e., surface mesonet and thermodynamic profiles) are capable of providing low-level moisture information but they are only employed for certain regions and field experiments. Radiosonde, the traditional measurement of obtaining humidity information, is limited because its spatial and temporal resolutions

are sparse. Alternatively, moisture information with high spatial resolution can be gained by the remote sensing approach but it has limitations in the cloud and precipitation environment (Lindsey et al. 2018; Zhu et al. 2020).

On the other hand, besides providing the information of Z and V_r , radar scanning can be utilized to retrieve moisture information. Ellis and Vivekanandan (2010) introduce a method to retrieve the environmental water vapor profile through the low level relying on the difference in the attenuation between S-band and Ka-band measurements of the National Center for Atmospheric Research (NCAR) S- and Ka-band dual-wavelength (S-PolKa) radar. The retrieved water vapor represents the moisture information outside and nearby the precipitation system. To the author's knowledge, the impact of assimilating this retrieved moisture data has not yet been examined. In addition to the S-PolKa-retrieved water vapor, another moisture information that can be achieved by weather radar is refractivity (N). Fabry et al. (1997) demonstrated the ability to retrieve the N of near-surface air based on the phase change detected from the stationary target located in the vicinity of the weather radar site. The N information can be obtained both before and after the landing of the weather system and carries the moisture information near the surface. Various researches employ N to correct the initial humidity field in the NWP model via data assimilation but most of these studies applied in midlatitude regions. The assimilation of radar-retrieved refractivity has not been extensively explored.

In this thesis, a collection of articles that are either published or in preparation were included to investigate the assimilation of the above two radar-retrieved moisture data with Z and V_r . Chapter 2 examined the effect of assimilating S-PolKa-retrieved water vapor data with Z and V_r data for convective-scale weather systems. The assimilation strategy for the retrieved water vapor information was also figured out. The study of assimilating S-PolKa-retrieved water vapor was conducted based on the Dynamics of the Madden-Julian Oscillation (DYNAMO) field campaign. Because this campaign was organized on Maldives island which lacks the stationary targets for S-Pol to retrieve N , the study of N assimilation could not be applied and investigated. Instead of DYNAMO, the Terrain-influenced Monsoon Rainfall Experiment/Southwest Monsoon Experiment (TiMREX/SoWMEX) in southwestern Taiwan was deployed to investigate the assimilation of radar-retrieved refractivity in Chapter 3 with two objectives. The first objective was to evaluate the impact of assimilating N along with Z and V_r on the QPF in the tropical region. Based on the characteristic of N , the second objective was to examine the N assimilation before and after the weather system landed, which has not

been broadly investigated.

1.5 Dissertation outline

This chapter gave a general overview of radar assimilation including its difficulties in terms of moisture correction and detailed the goal of the dissertation. The rest chapters are organized as follows:

Chapter 2 studies the assimilation of S-PolKa-retrieved water vapor with Z and Vr data. The vertical profile of humidity obtained from S-PolKa which stands for the environmental information before the precipitation system was assimilated in the WRF local ensemble transform Kalman filter data assimilation system (WLRAS) by using three real cases of the Dynamics of the Madden-Julian Oscillation Experiment (DYNAMO). The effect of assimilating additional S-PolKa-retrieved water vapor data was examined and the assimilation strategy for the retrieved water vapor information was investigated. It was found that the humidity information nearby precipitation systems is critical for further improving the analysis and forecast of convection. Our study figured out that the strategy of assimilating only retrieved water vapor data in the first hour and radial wind and reflectivity data in the second hour achieved the optimal analysis and short-term forecast.

In Chapter 3, the assimilation of radar-retrieved refractivity which carries the moisture information near the surface was investigated. Two cases in the Southwest Monsoon Experiment were employed with the high-resolution WLRAS to examine the effect of assimilating radar-retrieved refractivity along with Z and Vr and study the refractivity assimilation before and after the weather system landed. The results revealed the positive impact of additional refractivity assimilation in low-level moisture corrections and wind convergence enhancement, leading to better QPF. The results also pointed out the further improvement of QPF when continuing to assimilate extra refractivity after the weather system approached.

Chapter 4 summarizes the results of this dissertation research and discusses the assimilation of other moisture information which can be explored in the future.

Chapter 2. Assimilating Retrieved Water Vapor and Radar Data From NCAR S-PolKa: Performance and Validation Using Real Cases

This study investigated the effect of the assimilation of the S- and Ka-band dual-wavelength-retrieved water vapor data with radial wind and reflectivity data. The vertical profile of humidity, which provides environmental information before precipitation occurs, was obtained at low levels and thinned into averaged and four-quadrant profiles. Additionally, the following two strategies were examined: (1) assimilation of water vapor data with radar data for the entire 2 h and (2) assimilation of water vapor data in the first hour, and radial velocity and reflectivity data in the second hour. By using the WRF local ensemble transform Kalman filter data assimilation system, three real cases of the Dynamics of the Madden-Julian Oscillation Experiment were examined through a series of experiments. The analysis results revealed that assimilating additional water vapor data more markedly improved the analysis at the convective scale than assimilating radial wind and reflectivity data alone. In addition, the strategy of assimilating only retrieved water vapor data in the first hour and radial wind and reflectivity data in the second hour achieved the optimal analysis with which to launch the very short-term forecast. The evaluation of quantitative precipitation forecasting demonstrated that assimilating additional retrieved water vapor data more markedly improved the rain forecast compared with assimilating radar data only. When moisture data were assimilated, improved nowcasting could be extended up to 4 h. Furthermore, assimilating moisture profiles into four quadrants achieved more accurate analysis and forecast. Overall, our study demonstrated that the humidify information in nonprecipitation areas is critical for further improving the analysis and forecast of convective weather systems.

2.1 Introduction

The primary purpose of data assimilation at convective scales is to improve short-term forecasts, especially for severe weather events with heavy precipitation. The weather radar is a remote sensing tool that provides high temporal and spatial data useful for analyzing extreme weather phenomena (Houze et al. 1989; Germann and Zawadzki 2002, 2004). Numerous studies have discussed the advantages of including radar observations in various assimilation algorithms. For instance, radar data have been successfully assimilated 3DVAR algorithms (Xiao and Sun 2007; Chung et al. 2009; Sugimoto et al. 2009), 4DVAR algorithms (Sun and Crook 1997, 2001; Sun and Zhang 2008; Sun et al. 2010; Tai et al. 2011; Chang et al. 2014; Chang et al. 2016), and ensemble-based data assimilation systems (Snyder and Zhang 2003; Zhang et al. 2004; Tong and Xue 2004; Aksoy et al. 2009; Yussouf and Stensrud 2010; Dowell et al. 2011; Tsai et al. 2014). These studies have indicated that the assimilation of radar data (e.g., radial wind [V_r] and reflectivity [Z]) in numerical weather prediction (NWP) can enhance the simulated structure of the weather system and improve QPF for severe weather events, such as squall lines, supercell storms, and typhoons.

However, the assimilation of Z and V_r from weather radar has some limitations in regards to improving the analysis and forecast of convective weather systems. Ge et al. (2013) conducted observing system simulation experiments (OSSEs) to assimilate various state variables, emphasizing the influential roles of humidity in addition to that of horizontal wind in storm analysis and forecast. The assimilation of Z and V_r offers an opportunity to adjust the hydrometeors and wind fields inside precipitation systems; however, how such assimilation properly modifies temperature and humidity remains an active research topic. Many studies have applied various approaches to obtain and assimilate humidity information at convective scales. Wang et al. (2013) introduced a scheme to assimilate retrieved rainwater and water vapor data derived from Z and demonstrated that both the location and intensity of convection were accurately forecast in four cases of convective heavy rain. Caumont et al. (2010) and Wattrelot et al. (2014) employed the 1D+3DVar method in which the retrieved humidity is based on 1D Bayesian formalism and the observed Z is assimilated with the conventional 3DVar assimilation system. Their results indicated a notable enhancement in the performance of short-term accumulated precipitation forecasting. Through the assimilation of rainfall observed by radar and surface observations, Sun et al. (2020) revealed that rainfall data

are critical for adjusting humidity and temperature; reflectivity assimilation, however, only partially contributes to humidity correction. Alternatively, temperature and humidity fields can be modified through a semiempirical complex cloud analysis procedure. This semiempirical method demonstrates the ability to effectively analyze the in-cloud humidity field and improve storm forecasting (Hu et al. 2006; Pan and Wang 2019; Pan et al. 2020). Lai et al. (2019) derived vertically integrated liquid water from three-dimensional reflectivity and assimilated it with Z and V_r , alleviating the overprediction of storm cells. Despite the positive effects of assimilating retrieved moisture information, the aforementioned studies have largely focused on providing humidity information inside precipitation systems.

Crook (1996) and Fabry and Meunier (2020) indicated that slight changes in environmental humidity can modify rain patterns and intensity considerably. Information on the humidity surrounding severe weather systems is crucial for the prediction of storm initiation. Through assimilating the zenith total delay of ground-based global navigation satellite systems and radar data, Yang et al. (2020) demonstrated that assimilating the extra humidity in radar data-void regions can enhance moisture convergence, resulting in short-term forecast improvements. Furthermore, radar-derived refractivity, which provides near-surface humidity information nearby the precipitation system, was assimilated and investigated by Gasperoni et al. (2013). A series of sensitivity tests based on the OSSEs revealed that refractivity assimilation can correct low-level moisture errors. In addition to these two types of humidity information, Ellis and Vivekanandan (2010) demonstrated the ability to infer environmental water vapor profiles through the lower troposphere by using the attenuation difference between the S-band and Ka-band measurements of the National Center for Atmospheric Research (NCAR) S- and Ka-band dual-wavelength (S-PolKa) radar. The retrieved humidity was obtained outside the precipitation system and represented the moisture of the nonprecipitation area at low levels. The potential for utilizing dual-frequency for retrieving moisture information has been investigated in other studies (Tian et al. 2007; Ellis and Vivekanandan 2011), but the impact of retrieved water vapor data from S-PolKa has not yet been examined.

This study examined the effect of assimilating S-PolKa-retrieved water vapor data with Z and V_r data for convective-scale weather systems. The assimilation strategy for the retrieved water vapor information was also investigated. Two organized heavy rainfall events and a scattered convection event from the Dynamics of the Madden-Julian Oscillation (DYNAMO) field campaign (Yoneyama et al. 2013) were selected for

analysis. The organization of this paper is as follows. Section 2.2 introduces the assimilation system and observational dataset for assimilation. The experimental design and three case studies are described in Section 2.3. Section 2.4 details the improvement in rain forecasting using different strategies of retrieved moisture assimilation. Finally, Section 2.5 presents the summary and discussion.

2.2 Assimilation system and data description

2.2.1 WRF-Local ensemble transform Kalman filter radar assimilation system

The experiments in this study are based on the local ensemble transform Kalman filter (LETKF) algorithm (Hunt et al. 2007). The algorithm first calculates the ensemble mean and perturbation to define the state variables and their uncertainty:

$$\bar{\mathbf{x}}_a = \bar{\mathbf{x}}_b + \mathbf{X}_b \bar{\mathbf{w}} \quad (2.1)$$

$$\mathbf{X}_a = \mathbf{X}_b \mathbf{W} \quad (2.2)$$

where $\bar{\mathbf{x}}$ is a column vector with information on the ensemble mean of model variables and \mathbf{X} is a matrix containing the perturbation of ensemble members; the subscripts a and b denote analysis and background, respectively. $\bar{\mathbf{w}}$ and \mathbf{W} represent the analysis mean weighted vector and analysis perturbation weighted matrix, respectively, which can be obtained as follows:

$$\bar{\mathbf{w}} = \widetilde{\mathbf{P}}_a \mathbf{Y}_b^T \mathbf{R}^{-1} (\mathbf{y}_o - \bar{\mathbf{y}}_b) \quad (2.3)$$

$$\mathbf{W} = \sqrt{(K-1) \widetilde{\mathbf{P}}_a} \quad (2.4)$$

In Eqs. (2.3) and (2.4), the column vector $\bar{\mathbf{y}}_b$ and matrix \mathbf{Y}_b are the background ensemble mean and perturbation in the observation space, respectively; vector \mathbf{y}_o is the observation; matrix \mathbf{R} is the observation error covariance; K is the ensemble size. Matrix $\widetilde{\mathbf{P}}_a$ is the analysis error covariance, which is computed as follows:

$$\widetilde{\mathbf{P}}_a = \left[\frac{(K-1)\mathbf{I}}{\rho} + \mathbf{Y}_b^T \mathbf{R}^{-1} \mathbf{Y}_b \right]^{-1} \quad (2.5)$$

In Eq. (2.5), \mathbf{I} is an identity matrix and ρ is a multiplicative covariance inflation factor (Anderson 2001). This study assigned a covariance inflation of 1.08 (Tsai et al. 2014) to reduce underdispersiveness.

Yang et al. (2009) developed a system that combines the LETKF algorithm with the WRF model. Tsai et al. (2014) extended this system to assimilate radar data in their WRF-Local ensemble transform Kalman filter radar assimilation system (WLRAS) and improve the very short-term forecast for the convective scale. Several studies (Cheng et al. 2020; Tsai and Chung 2020; Wu et al. 2020; Yang et al. 2020) have successfully applied the WLRAS to examine severe weather cases. The WLRAS updates every single model variable, including wind, geopotential height, potential temperature perturbation, and the mixing ratio of water vapor (Q_v) and hydrometeors; different model variables use different error covariance localization radii. The localization radius set up for the system in this study is based on that by Tsai et al. (2014), with the exception of Q_v localization, which adapts retrieved Q_v assimilated in nonprecipitation areas. The localization for horizontal wind (U and V) was set as 36 km, the temperature and hydrometeor mixing ratio of cloud as 24 km, and the vertical velocity and hydrometeor mixing ratio of rain, snow, and graupel as 12 km. The study utilized a broader localization for the radius for updating moisture (i.e., 48 km), as suggested by Yang et al. (2020). The features of background error correlations (BECRs) in this study also supported this setup (see Section 2.3.2). For the vertical localization, 4 km was set for all variables, following Tsai et al. (2014).

2.2.2 Model configuration

The two-way nesting WRF model version 3.9.1 was employed in the experiments. The model uses three nested domains, with horizontal grid spacing of 27 km, 9 km, and 3 km for domain 1 (131×129 grid points), domain 2 (175×169 grid points), and domain 3 (139×133 grid points), respectively (Fig. 2.1a). The outermost and innermost domains cover the northern part of the Indian Ocean and the Maldives, respectively. All experiments were performed with 52 vertical levels (top at 10 hPa), and all physics parameterizations remained unchanged. In particular, the longwave and shortwave

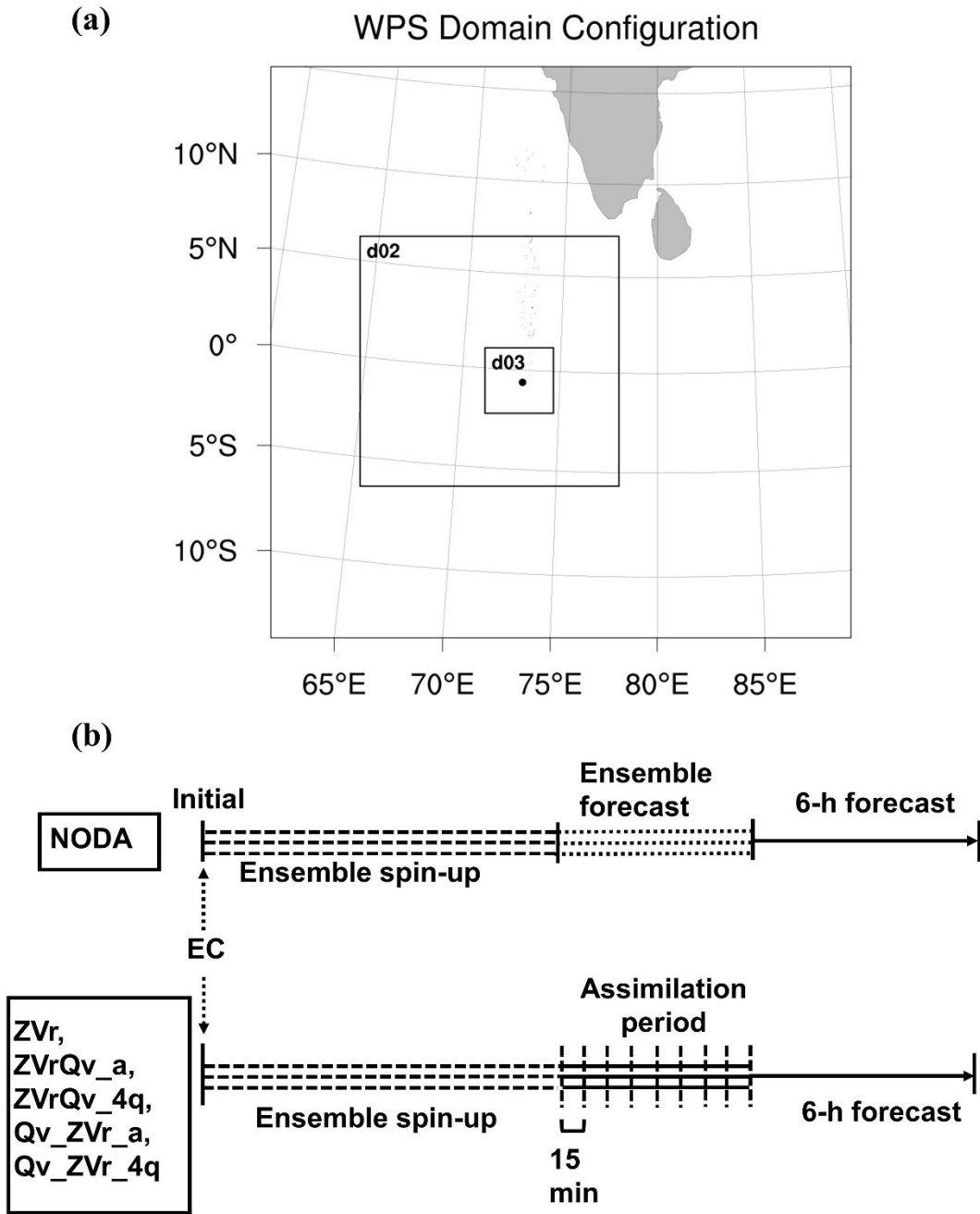


Figure 2.1: (a) The WRF model domains. The black dot indicates the S-PolKa location. The horizontal grid spacing of domains 1, 2, and 3 are 27 km (131×129 points), 9 km (175×169 points), and 3 km (139×133 points), respectively. (b) The experimental design schematic. The triple dash lines represent the model spin-up period and the triple dotted lines and solid lines represent the ensemble forecast and data assimilation period, respectively. The single solid lines indicate the mean forecast. The vertical dash bars represent the assimilation cycles.

radiation parameterization schemes were the Rapid Radiative Transfer Model (RRTM, Mlawer et al. 1997) and Dudhia scheme (1989), respectively. The Yonsei University planetary boundary layer scheme was also employed (Hong et al. 2006). The Grell–Dévényi cumulus scheme (Grell and Dévényi 2002) was only used in domain 1 and

domain 2. To manage microphysics explicitly, the Goddard Cumulus Ensemble (GCE) scheme (Tao et al. 2003) was used for domain 3.

2.2.3 Radar observations

The Z and V_r datasets from the NCAR S-Pol (10-cm wavelength) located at Addu Atoll (0.63°S, 73.10°E) in the Maldives were utilized for this study. The NCAR/Earth Observing Laboratory (EOL) provides quality-controlled radar data. The beam width and maximum range of the S-Pol radar are 0.91° and 150 km, respectively. The plan position indicator (PPI) scanning covers 360° of azimuth with eight elevation angles (from 0.5° to 11.0°) and 1° azimuthal resolution. The superobbing strategy (Lindskog et al. 2004; Alpert and Kumar 2007) was adopted to thin the data and avoid spatial correlations between observations. The Z and V_r were gridded to 3 km and 3° intervals in the radial and azimuthal directions. The observation errors were set as 3 m s⁻¹ and 5 dB(Z) for V_r and Z , respectively (Tsai et al. 2014).

2.2.4 S-PolKa–retrieved water vapor density

Ellis and Vivekanandan (2010) introduced a method to retrieve water vapor density based on the difference in atmospheric attenuation at two different wavelength radar observations. The Ka-band (8-mm wavelength) attenuation has a much stronger dependence on water vapor than S-band attenuation. Therefore, S-band attenuation can be neglected, and the mean water vapor content can be estimated based on Ka-band atmospheric attenuation. Through a cloud- and precipitation-free atmosphere, at the end of radar ray segments, the Ka-band Z value is subtracted from the S-band Z and combined with the range to obtain the Ka-band total atmospheric attenuation. Of the two types of ray segments, the more common primary rays start at the radar and end at the closest edge of an echo, whereas secondary rays connect between the back edge of an echo and the front edge of another echo further in range. To obtain ray segments, the data must be from Rayleigh scatterers at both the Ka- and S-bands, and the effect of measurement noise must be small compared with the attenuation. Furthermore, ray segments must be at least 15 km in length, with a minimum of 10 radar range gates averaged in a 2D patch at the front edge of the echoes. With the attenuation obtained on several ray segments, the water vapor density is estimated using the relation between humidity and attenuation that was identified with Liebe’s microwave propagation model. The Liebe (1985) model was run numerous times to compute the water vapor density under different pressures, temperatures, and attenuations, and a polynomial fit was used to develop an equation for

humidity as a function of attenuation. The estimated water vapor density could then be assigned to the height of the midpoint of the ray segment. This retrieved water vapor was fundamentally unbiased compared with the sounding measurements (Ellis and Vivekanandan 2017). However, when heavy rain spreads over the radar, the identification of usable ray segments may not be possible, and this retrieval method thus cannot be applied. The observation error of the Q_v was 1.5 g kg^{-1} in this study.

2.2.5 Observation operator

This study estimated the Q_v from the S-PolKa–retrieved water vapor density (ρ_w) and sounding data from the Atmospheric Radiation Measurement (ARM) M1 Airport (Addu Atoll, Gan Island, Maldives site, provided by NCAR/EOL). With the use of the temperature (T) and pressure of dry air (P) obtained through subtraction of the actual vapor pressure from the total air pressure at Gan station (0.69°S, 73.15°E), the density of the dry air can be calculated as follows:

$$\rho_d = \frac{P}{RT} \quad (2.6)$$

where R is the ideal gas constant and equals $287.05 \text{ J (kg K)}^{-1}$. Then, the Q_v can be obtained as follows:

$$Q_v = \frac{\rho_w}{\rho_d} \quad (2.7)$$

The selected time of Gan sounding data must be closest to the time of the S-PolKa–retrieved water vapor density (15 min frequency).

In this study, the model used the three-category ice scheme of the GCE, in which the Z factors associated with rainwater (Z_r), snow (Z_s), and graupel (Z_g) were computed as follows:

$$Z_r = 3.63 \times 10^9 (\rho_a q_r)^{1.75} \quad (2.8)$$

$$Z_s = 1.21 \times 10^{11} (\rho_a q_s)^{1.75}, \text{ when } T > 0^\circ\text{C}, \quad (2.9)$$

$$Z_s = 2.79 \times 10^8 (\rho_a q_s)^{1.75}, \text{ when } T \leq 0^\circ\text{C}, \quad (2.10)$$

$$Z_g = 1.12 \times 10^9 (\rho_a q_g)^{1.75} \quad (2.11)$$

where ρ_a is the air density, and q_r , q_s , and q_g represent the hydrometeor mixing ratio of rain, snow, and graupel, respectively. In the WLRAS, the forward model for Z (Dowell et al. 2011) is expressed as

$$Z = Z_r + Z_s + Z_g \quad (2.12)$$

In terms of the Vr , the forward model is described as

$$Vr = [ux + vy + (w - V_t)z] (x^2 + y^2 + z^2)^{-1/2} \quad (2.13)$$

where x , y , and z are the Cartesian coordinates with the origin at the radar site, and u , v , and w are the zonal, meridional, and vertical winds, respectively. The terminal velocity V_t can be computed by assuming a Marshall–Palmer drop size distribution (Marshall and Palmer 1948) as follows:

$$V_t = 5.40 \left(\frac{p_0}{p} \right)^{0.4} (\rho_a q_r)^{0.125} \quad (2.14)$$

where p_0 and \bar{p} denote the surface pressure and base-state pressure, respectively.

2.3 Case description and experimental design

2.3.1 Description of the three study cases

In this study, three cases were selected for investigation. The first two cases occurred on 18 October 2011 and 16 October 2011, and constituted the two events with the most rain during the DYNAMO campaign (Zuluaga and Houze 2013). In the first case (i.e., 18 October 2011), two cyclones were detected over the Arabian Sea, west of the S-PolKa location. The Inter-Tropical Convergence Zone (ITCZ) remained to the south of Gan Island, with a low-pressure system over the north causing the development of many convective systems around the island. Within the S-PolKa domain, from 1600 to 1700 UTC (Figs. 2.2a,d), two strong convective lines oriented southwest-northeast (denoted by two black boxes with the letters A and B in Fig. 2.2a) formed to the southeast

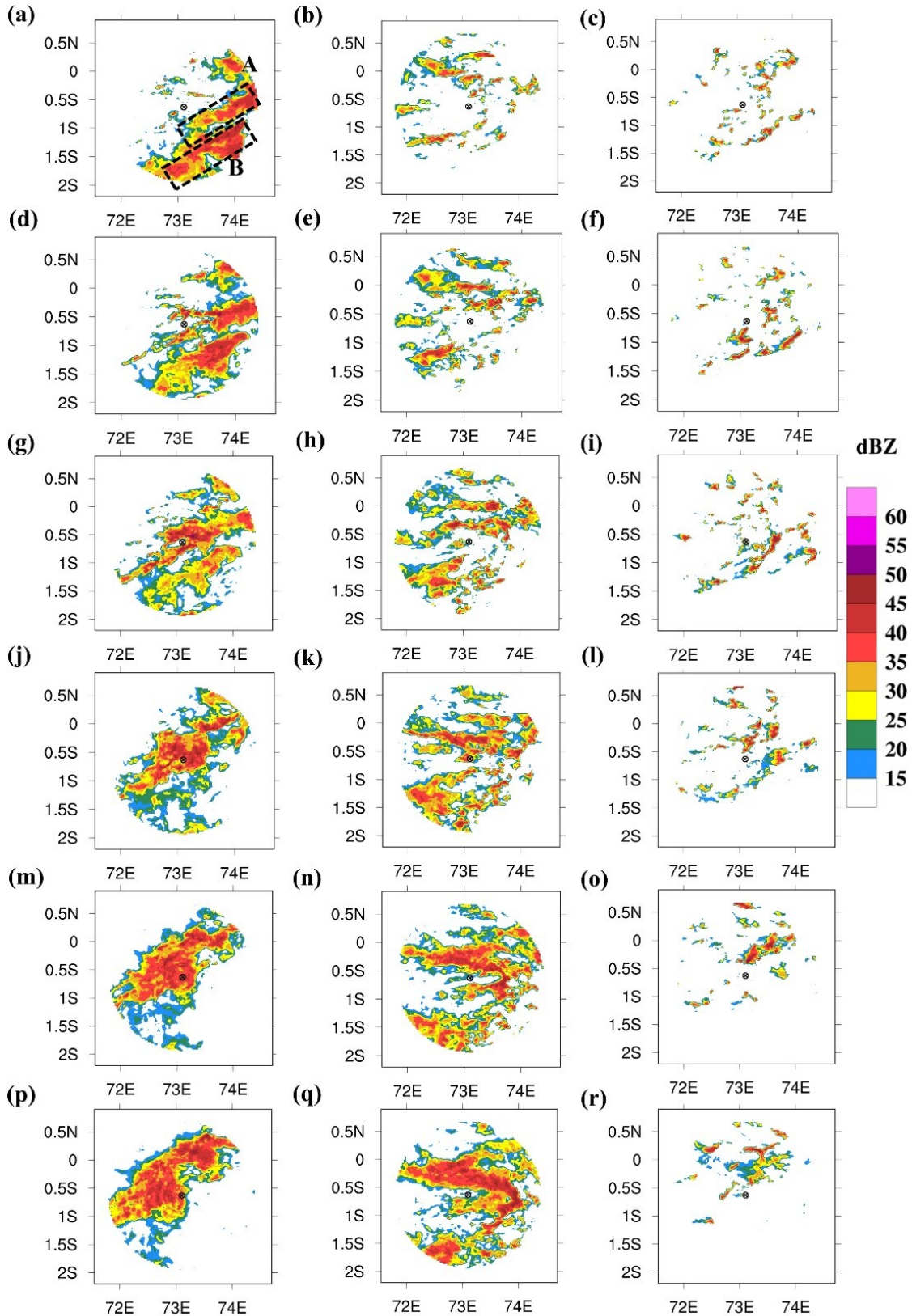


Figure 2.2: Hourly column maximum Z observation of the three cases. The first case (a, d, g, j, m, p) from 1600 to 2100 UTC 18 Oct 2011; the second case (b, e, h, k, n, q) from 0000 to 0500 UTC 16 Oct 2011; and the third case (c, f, i, l, o, r) from 1030 to 1530 UTC 12 Oct 2011. Two convective lines in the first case are denoted by two black boxes with the letters A and B. The encircled black cross indicates the S-PolKa location.

of S-PolKa. Convective lines continued to develop, strengthen, and move toward the radar site. Convection A approached and covered the radar at approximately 1800 UTC (Fig. 2.2g). From 1900 to 2100 UTC (Figs. 2.2j,m,p), convection A intensified and moved to the northwest and convection B dissipated.

In the second case (i.e., 16 October 2011), weak twin cyclones were situated to the south and north of the equator. Low-level northwesterly winds at 925 hPa appeared between the cyclones and covered the Gan site. At the surface, a strong westerly wind component was dominant. At 0000 UTC (Fig. 2.2b), large clusters of convective cells developed within the S-PolKa domain, and in the following 3 h, these clusters continued developing, expanding and merging to form intensive rain bands at 0300 UTC (Figs. 2.2e,h,k). The convection strengthened and covered almost the entire radar domain from 0400 to 0500 UTC (Figs. 2.2n,q), with the most robust convective line located to the north of S-PolKa.

The third case (i.e., 12 October 2011; Figs. 2.2c,f,i,l,o,r) is different from the first two cases, with easterly winds between two anticyclonic gyres at 200 hPa dominating over Gan Island. At low levels, moderate southwesterly winds covered the S-PolKa domain, over which convective cells were scattered and localized. Some convective cells formed in the S-PolKa domain at approximately 1030 UTC (Fig. 2.2c), intensified and continued to move northwest until 1530 UTC (Fig. 2.2r).

2.3.2 Experimental design

This study used the high-resolution ($0.75^\circ \times 0.75^\circ$, every 6 h) ERA-interim reanalysis data as the initial and lateral boundary conditions. Based on the ERA-interim and WRF-3DVar random perturbation (Barker et al. 2004), 40 ensemble members were generated in domain 1, then downscaled to domains 2 and 3. After the 10 to 16 h of spin-up for each case, observations of the Z , V_r , and retrieved Q_v from the NCAR S-PolKa were assimilated in domain 3.

To design an effective strategy for assimilating retrieved moisture information, the Q_v in the second case (i.e., at 0000 UTC 16 October 2011) was selected to demonstrate the Q_v distribution. Figure 2.3a depicts the original retrieved Q_v locations for all levels, which were all within 25 km from the radar center. Two approaches for thinning the Q_v were employed because of the close distance between each Q_v location. The first method combined the average of all observations and results in one Q_v profile (Fig. 2.3b); the

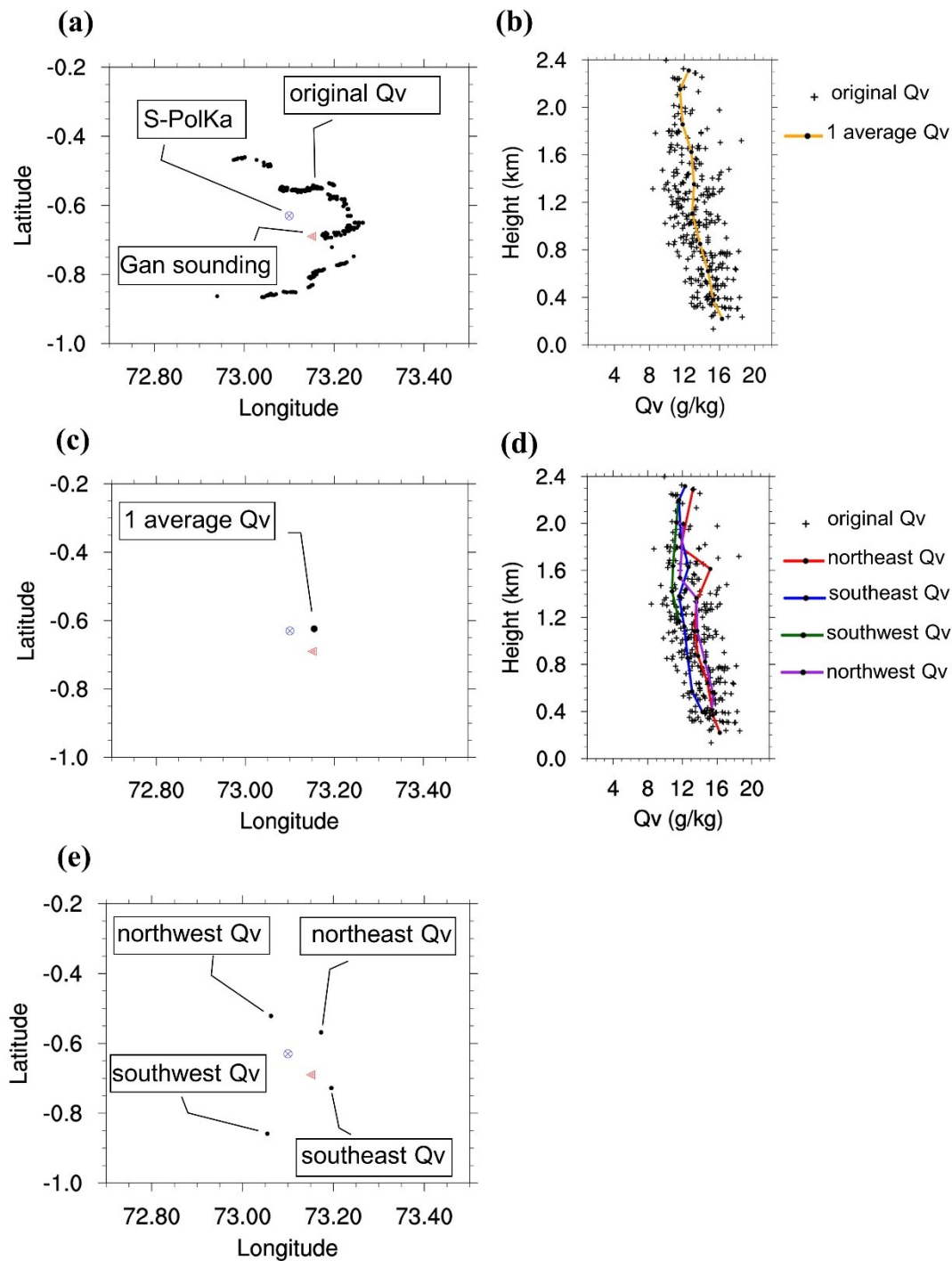


Figure 2.3: (a) The original S-PolKa–retrieved Q_v location for all levels. (b) and (d) The vertical profiles of one averaged Q_v profile and four-quadrant Q_v profiles (solid color lines), and the original retrieved Q_v values (black crosses). (c) and (e) The location of one averaged Q_v profile and four-quadrant Q_v profiles (black dot); the encircled blue cross indicates the radar location, and the red triangle represents the Gan sounding station. These figures are plotted at 0000 UTC 16 Oct 2011.

averaged Q_v was then located at the mean latitude and longitude of all points (Fig. 2.3c). The second method consisted of separating the Q_v data into four quadrants (northeast, southeast, southwest, and northwest of the radar site; Ellis and Vivekanandan 2017),

computing an averaged Q_v profile in each quadrant, and locating it at the point of the mean latitude and longitude of points in the same quadrant (Figs. 2.3d,e). Figure 2.4 depicts the standard deviation between the vertical profile observations of one averaged Q_v profile and four-quadrant Q_v profiles used for the three cases. The retrieved Q_v height ranged between 0.05 and 2.5 km. Among the three cases, the deviation of four-quadrant Q_v profiles relative to the averaged Q_v profile was more evident in the second case than in the other two cases.

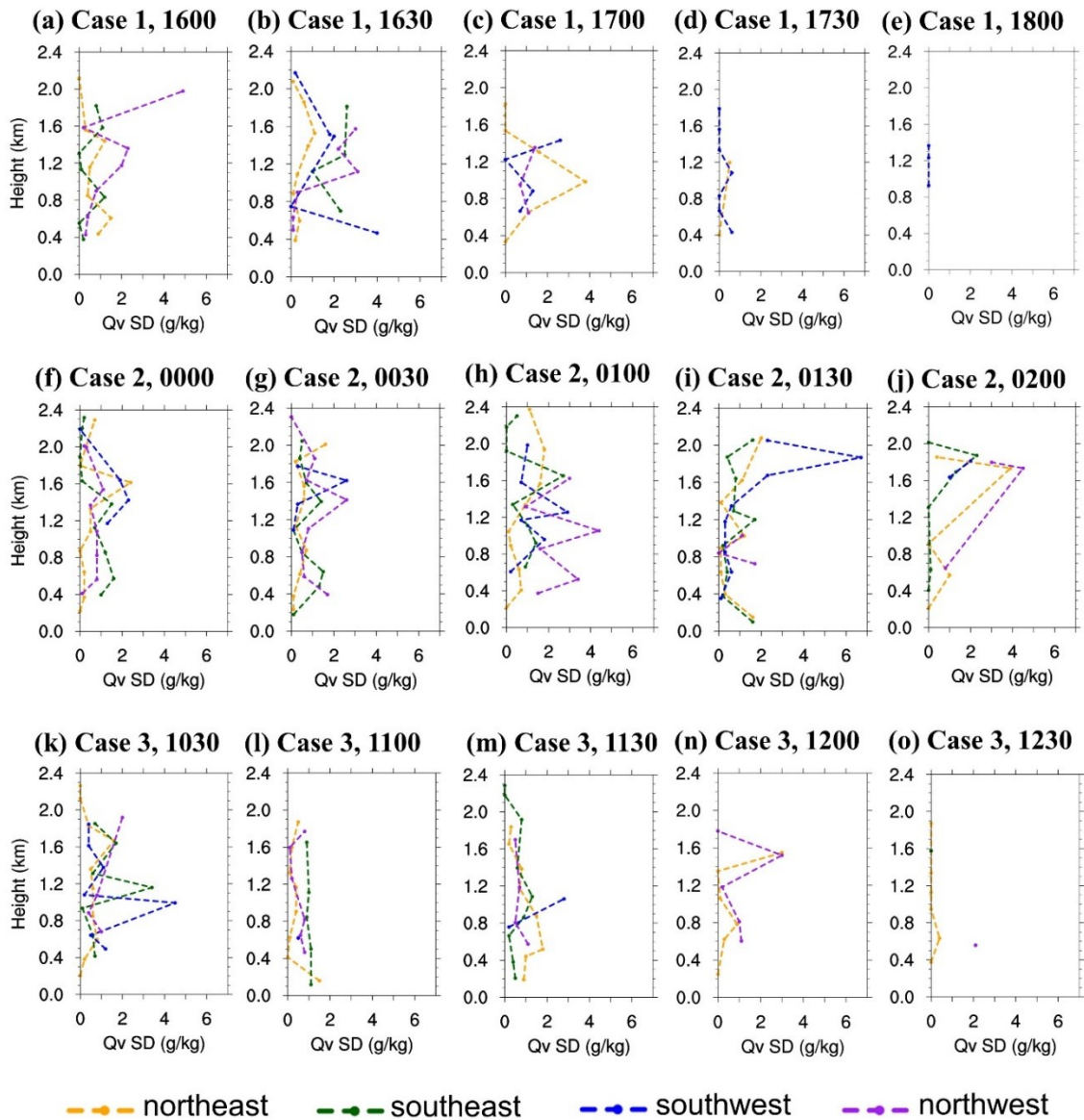


Figure 2.4: The standard deviation (SD) between Q_v derived through the average profile method (i.e., one averaged Q_v profile) and four-quadrant method (i.e., northeast, southeast, southwest, and northwest) for the three study cases: 18 Oct 2011 (a–e), 16 Oct 2011 (f–j), and 12 Oct 2011 (k–o). The figures are plotted every 30 min in each case beginning from the first cycle.

To properly set up the localization radius for updating moisture information, the BECRs between the Q_v and itself and with U and V , computed with respect to the reference point at the S-PolKa location (nonprecipitation area), are illustrated in Fig. 2.5. The BECRs are presented at the time of the first cycle before assimilation. The high values and long correlation lengths in the space of the BECRs were demonstrated in all three cases, except for the BECR between the Q_v and wind (U and V) in the third case. This indicated that the humidity field in nonprecipitation areas can propagate the information to adjust the moisture and wind fields in broad ranges. Because the retrieved Q_v was only

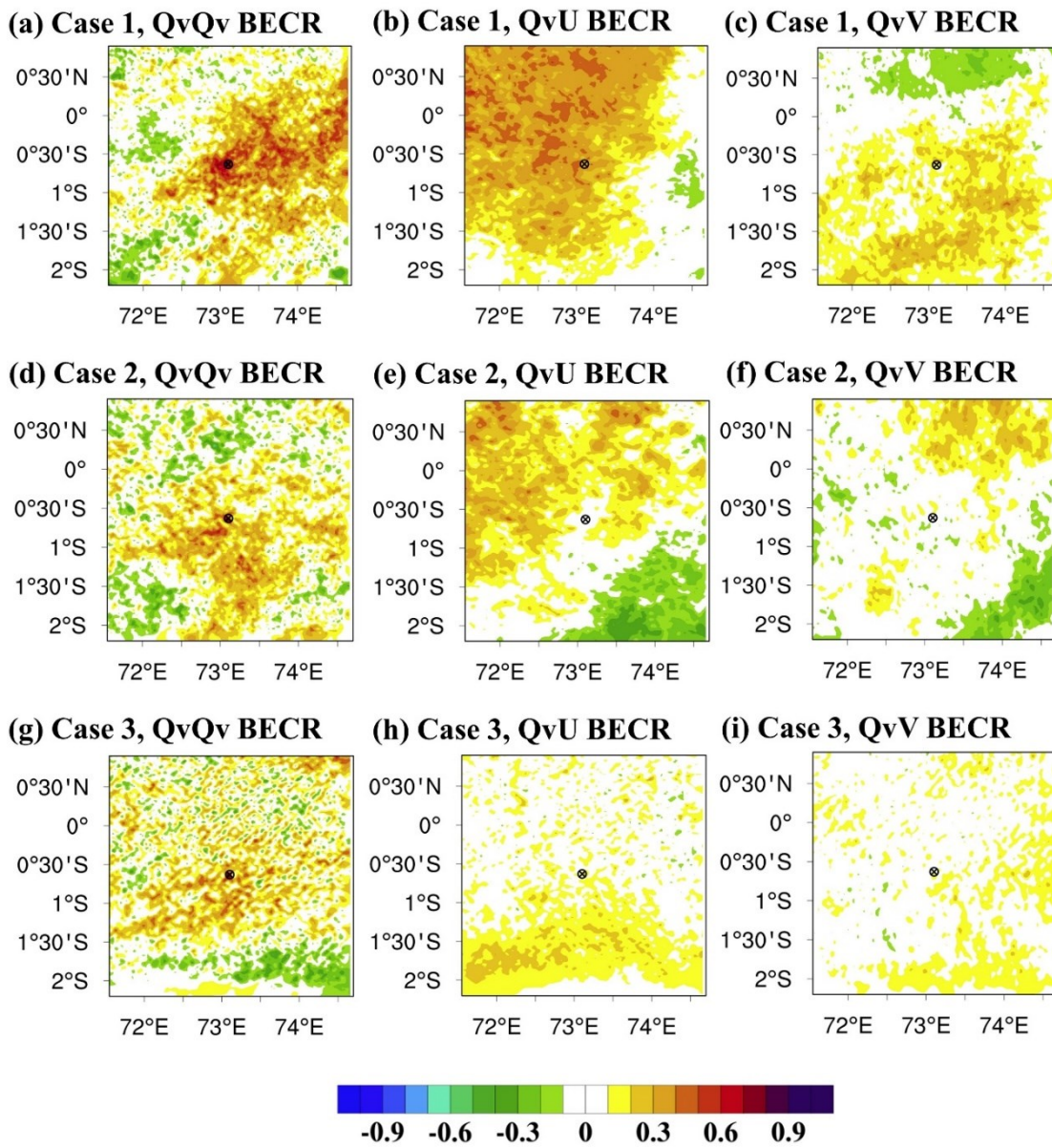


Figure 2.5: The BECRs estimated using the ensemble between Q_v and Q_v (a, d, g), Q_v and U (b, e, h), and Q_v and V (c, f, i) at 1 km, with the S-PolKa location (encircled black cross) serving as the reference point for the first case (a–c), second case (d–f), and third case (g–i). The correlations are presented at the time of the first cycle before assimilation.

available in the nonprecipitation area, experiments were conducted for each case based on the characteristics of the retrieved water vapor. The NODA experiment entailed downscaling ensemble forecasts to domain 3. In experiment ZVr, radar data (Z and Vr) were assimilated, and in experiments ZVrQv_a and ZVrQv_4q, radar data were assimilated with the retrieved Qv (Z and Vr were assimilated sequentially after Qv assimilation); ZVrQv_a used one averaged Qv profile, and ZVrQv_4q used four-quadrant Qv profiles. The information of one averaged Qv profile and four-quadrant Qv profiles was utilized in experiments Qv_ZVr_a and Qv_ZVr_4q, respectively, assimilating only water vapor information in the first hour and Z and Vr data in the second hour. The six experiments are summarized in Table 2.1. The assimilation period for all data assimilation experiments was 2 h, with a 15-min frequency (i.e., nine cycles). All experiments were initialized with an ensemble mean analysis of the final cycle to obtain a 6-h deterministic forecast. The experimental design diagram is presented in Fig. 2.1b, and the study case and each case's experimental time setting are detailed in Table 2.2.

Table 2.1: Summary of experiments, the symbols “_” and “x” indicate that the information was not assimilated and was assimilated, respectively.

No.	Experiments	Data assimilated in the first hour				Data assimilated in the second hour			
		Z	Vr	1 Qv profile	4 Qv profiles	Z	Vr	1 Qv profile	4 Qv profiles
1	NODA	–	–	–	–	–	–	–	–
2	ZVr	x	x			x	x		
3	ZVrQv_a	x	x	x		x	x	x	
4	Qv_ZVr_a			x		x	x		
5	ZVrQv_4q	x	x		x	x		x	
6	Qv_ZVr_4q				x	x	x		

Table 2.2: Summary of study cases and time period settings for each case.

Cases	Convective Properties	Spin-up time	Assimilation time	Short forecast time
18 Oct 2011	Southwest-northeast lines convection, large convective portion eastern S-PolKa domain	0000 - 1600 UTC	1600 -1800 UTC	1800 - 0000 UTC 19 Oct
16 Oct 2011	No obvious organization, large convective portion northern S- PolKa domain	0600 UTC 15 Oct - 0000 UTC 16 Oct	0000 -0200 UTC	0200 - 0800 UTC
12 Oct 2011	Scattered convective cells, westward moving	0000 - 1030 UTC	1030 -1230 UTC	1230 - 1830 UTC

2.4 Results of the analysis and forecast

The effect of assimilation of S-PolKa-retrieved Q_v , V_r , and Z for convective scale is evaluated in this section. First, the accuracy of the analysis was examined using the radar observations and the S-PolKa-retrieved Q_v . Then, the short-term forecast was assessed using the S-Pol-derived estimated rainfall (Dolan et al. 2017) and Gan station data.

2.4.1 Performance of the analysis

To investigate the impact of assimilating additional retrieved Q_v , we first examined experiments ZV_r , $ZV_rQ_v_a$, and $ZV_rQ_v_4q$. Figure 2.6 depicts the Q_v increment of these three experiments at 1 km at the first assimilation cycle for the three cases. In the first case (Figs. 2.6a–c), at the first cycle (i.e., 1600 UTC 18 October 2011), experiments $ZV_rQ_v_a$ and $ZV_rQ_v_4q$ increased the moisture of the nonprecipitation area near the S-PolKa location, with a marked enhancement observed in $ZV_rQ_v_a$. Figure 2.7a illustrates a comparison of the Q_v Root Mean Square Errors (RMSEs) with the S-PolKa-retrieved Q_v for the first case. The Q_v correction of experiment $ZV_rQ_v_a$ and $ZV_rQ_v_4q$ was more precise than that of ZV_r for most assimilation cycles. Additionally, assimilating four-quadrant Q_v profiles could more accurately represent the moisture

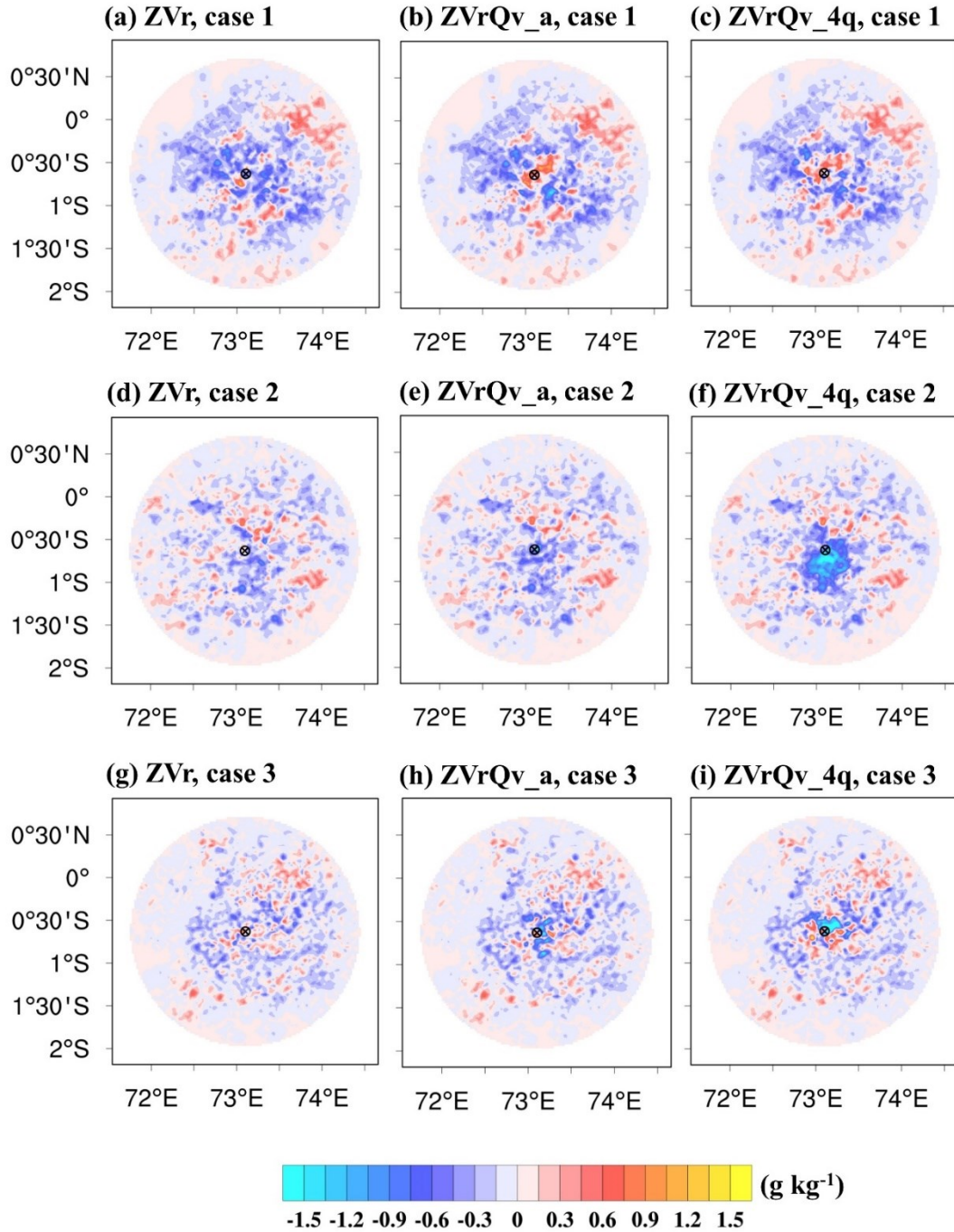


Figure 2.6: The Q_v analysis increment at 1 km at the first cycle for the first case (a–c), second case (d–f), and third case (g–i). The increments are from experiment ZVr (a, d, g), ZVrQv_a (b, e, h), and ZVrQv_4q (c, f, i). The encircled black cross indicates the S-PolKa location.

environment than assimilating one averaged Q_v profile. In the second case, at the first cycle (i.e., 0000 UTC 16 October 2011), similar to the first case, retrieved Q_v assimilation could adjust the moisture in the nonprecipitation areas (Figs. 2.6e,f versus Fig. 2.6d). The moisture corrections generated through assimilating four-quadrant Q_v profiles were more notable than those generated through assimilating one averaged Q_v

profile. The Q_v modifications in the ZVrQv_a and ZVrQv_4q experiments were verified to be more precise than that in ZVr across nine assimilation cycles (Fig. 2.7b). Moreover, ZVrQv_4q had a lower Q_v RMSE than ZVrQv_a. The Q_v increments in experiments ZVr, ZVrQv_a, and ZVrQv_4q for the third case at the first cycle (i.e., 1030 UTC 12 October 2011) are presented in Figs. 2.6g–i. The retrieved Q_v assimilation could modify the moisture environment near S-PolKa, and the more obvious moisture corrections occurred in the experiment utilizing the four-quadrant Q_v profiles (Fig. 2.6i). The RMSEs illustrated in Fig. 2.7c verified that the Q_v adjustment in experiments ZVrQv_a and ZVrQv_4q was more accurate than that in ZVr. Among these three experiments, the lowest Q_v errors occurred in experiment ZVrQv_4q for most assimilation cycles.

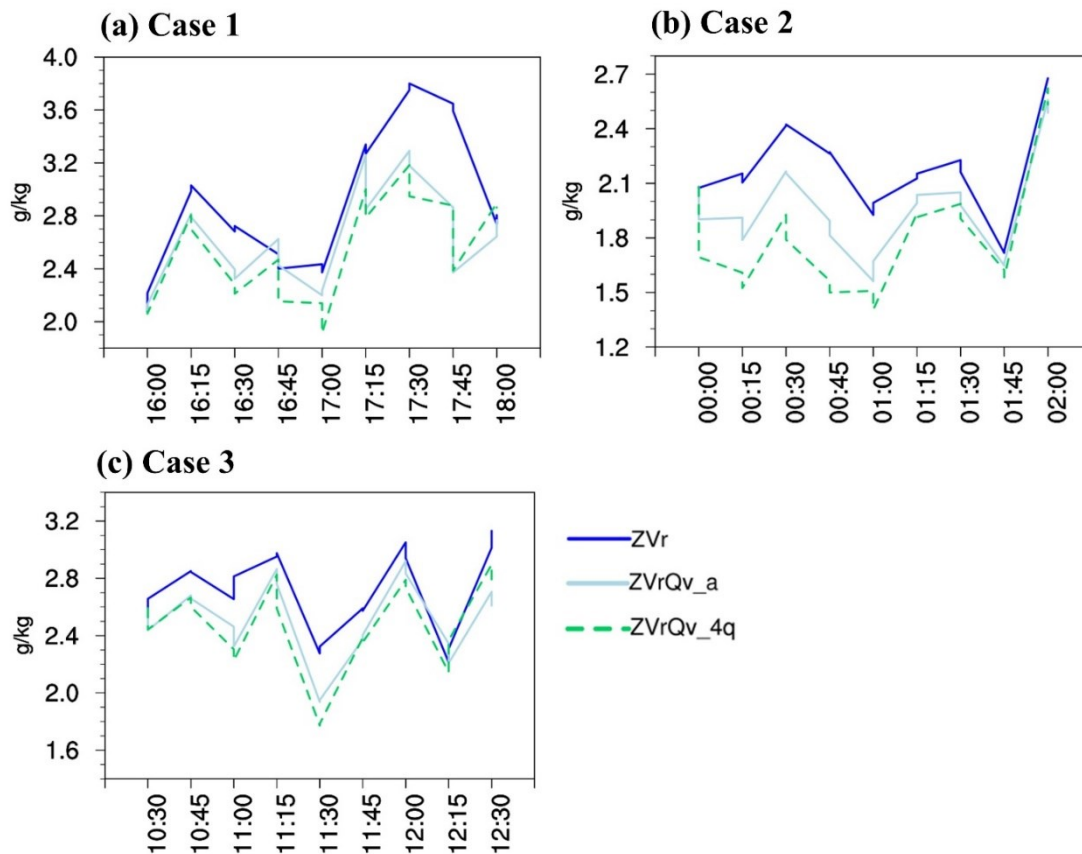


Figure 2.7: RMSEs of Q_v verified against S-PolKa-retrieved Q_v across nine assimilation cycles for the three cases.

The moisture increment in all three cases indicated that assimilating one averaged Q_v profile or four-quadrant Q_v profiles more effectively modifies the moisture environment than assimilating only Z and Vr . More accurate modifications occurred when four-quadrant Q_v profiles were included in the assimilation process. Furthermore, among the three cases, the second case exhibited more marked Q_v improvement in $ZVrQv_4q$ than in $ZVrQv_a$ and ZVr . The benefit was most like related to the more complete four-quadrant Q_v profiles in the second case. Additionally, this case had more variety in the humidity profiles in different directions (Fig. 2.4).

Figures 2.8a–f present the analysis of the column maximum Z at 1800 UTC 18 October 2011, for the six experiments. Compared with the observations in Fig. 2.2g, the NODA experiment (Fig. 2.8a) could not capture strong convection in the right positions. By contrast, all experiments assimilating the Z and Vr simulated the intense convection in the right area (Figs. 2.8b–f). Additionally, most false alarms in the convective area of NODA could be alleviated in the data assimilation experiments. The difference between the observation and analysis mean of the Z at 1 km in the final cycle is illustrated in Figs. 2.8g–l; the greatest Z deviation was noted in NODA (Fig. 2.8g). Slight improvements were observed in terms of the Z deviation in $ZVrQv_a$ and $ZVrQv_4q$ compared with that in ZVr after nine assimilation cycles (Figs. 2.8h,i,k). Conversely, experiments Qv_ZVr_a and Qv_ZVr_4q (Figs. 2.8j,l) generated Z simulations that most closely matched the observations among the six experiments.

Figures 2.9a–f depict the column maximum Z of the six experiments for the second case at the analysis time of 0200 UTC 16 October 2011. Compared with the observed convective lines (Fig. 2.2h), the simulated convection was weaker but more widespread, covering the entire NODA experiment domain. Conversely, all experiments resulted in strong convective cells after radar data assimilation (Figs. 2.9b–f). Some false alarms occurred in the southeast corner domain in experiments ZVr , $ZVrQv_a$, and $ZVrQv_4q$ (Figs. 2.9b,c,e) but were slightly improved in Qv_ZVr_a and Qv_ZVr_4q (Figs. 2.9d,f). Additionally, Qv_ZVr_a and Qv_ZVr_4q enhanced the most intense convective line to the north of the radar compared with other experiments. Figures 2.9g–l describe the deviation between the observation and analysis mean of the Z in the six experiments at 1 km in the final cycle. The results indicated that the simulated Z in the Qv_ZVr_a and Qv_ZVr_4q experiments was more accurate than that in the NODA, ZVr , $ZVrQv_a$, and $ZVrQv_4q$ experiments (Figs. 2.9j,l versus Figs. 2.9g,h,i,k).

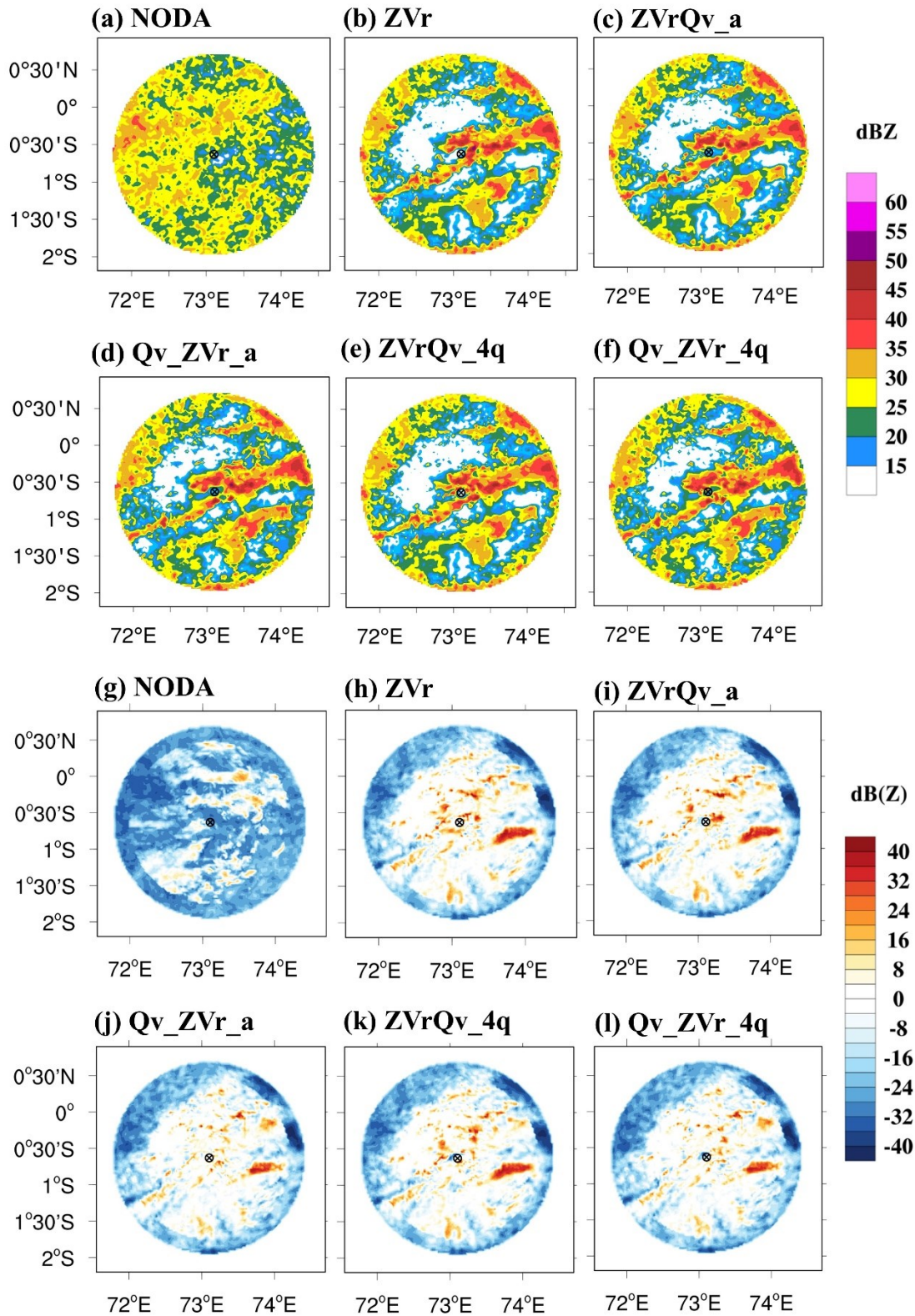


Figure 2.8: Column maximum Z (a–f). The difference between the observation and analysis mean of the Z at 1 km (g–l) at the final cycle of the first case (1800 UTC 18 Oct 2011). (a, g) NODA; (b, h) ZVr; (c, i) ZVrQv_a; (d, j) Qv_ZVr_a; (e, k) ZVrQv_4q; and (f, l) Qv_ZVr_4q. The encircled black cross indicates the S-PolKa location.

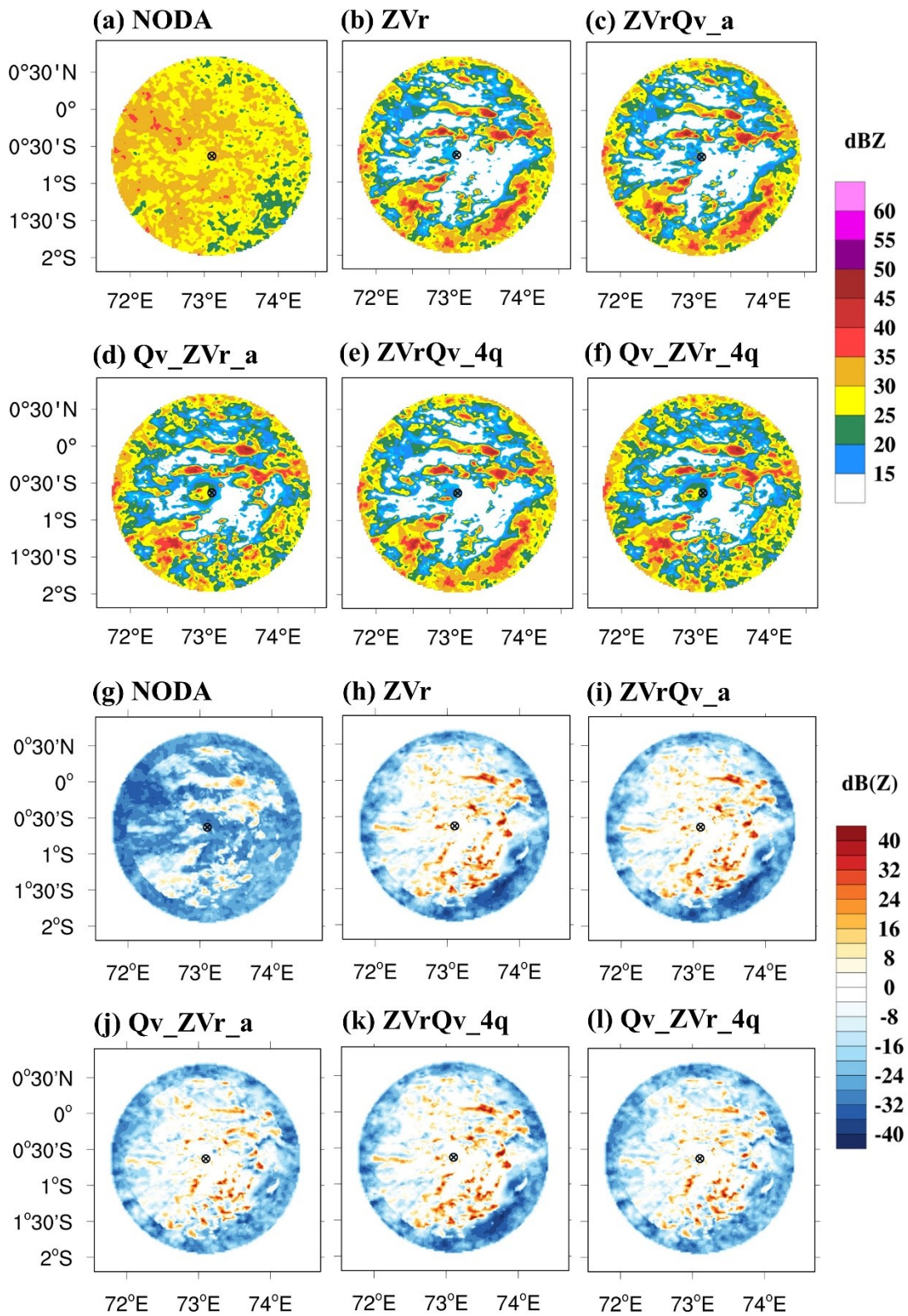


Figure 2.9: As in Fig. 2.8, but for the second case at 0200 UTC 16 Oct 2011.

Figure 2.10 presents the column maximum Z in the final analysis step of the third case (1230 UTC 12 October 2011). Compared with the observation (Fig. 2.2i), the NODA experiments exhibited widespread coverage of Z from 10 to 20 dBZ (Fig. 2.10a). The highest Z in NODA was less than 30 dBZ; however, in all the data assimilation experiments, the highest Z value ranged between 45 and 50 dBZ (Figs. 2.10b–f). The comparison between the observation and analysis mean of the Z in the six experiments at 1 km in the final cycle is depicted in Figs. 2.10g–l. Some improvements were noted near S-PolKa in experiments ZVrQv_a and ZVrQv_4q. The least deviation from the observation was observed in experiments Qv_ZVr_a and Qv_ZVr_4q.

For a more detailed comparison, the RMSEs of the Z , Vr , and Qv in the final analysis cycle were calculated and are listed in Table 2.3; the smallest RMSEs of these three variables in each case are indicated in bold font. Overall, the Qv assimilation experiments had lower Z , Vr , and Qv RMSEs compared with the experiments assimilating only the Z and Vr in all three cases. The most marked improvement in the assimilation of the Qv was obtained in the second case, which may be attributed to the more varied humidity profiles in this case, as mentioned in section 2.3.2. Additionally, experiments Qv_ZVr_a and Qv_ZVr_4q resulted in more accurate Z , Vr , and Qv simulations than did ZVrQv_a and ZVrQv_4q.

The analysis results indicated that the assimilation of additional S-PolKa–retrieved Qv can enhance the modification of moisture more effectively than the assimilation of Z and Vr alone. However, assimilating only the Qv in nonprecipitation areas in the first hour of the assimilation period generated a more precise moisture environment than assimilating all data over the entire 2 h and resulted in the outperformed simulation of Z , Vr , and Qv . Furthermore, in the comparison of the two thinning methods (i.e., one averaged Qv profile and four-quadrant Qv profiles), moisture was more significantly and precisely modified in the four-quadrant Qv profile assimilation.

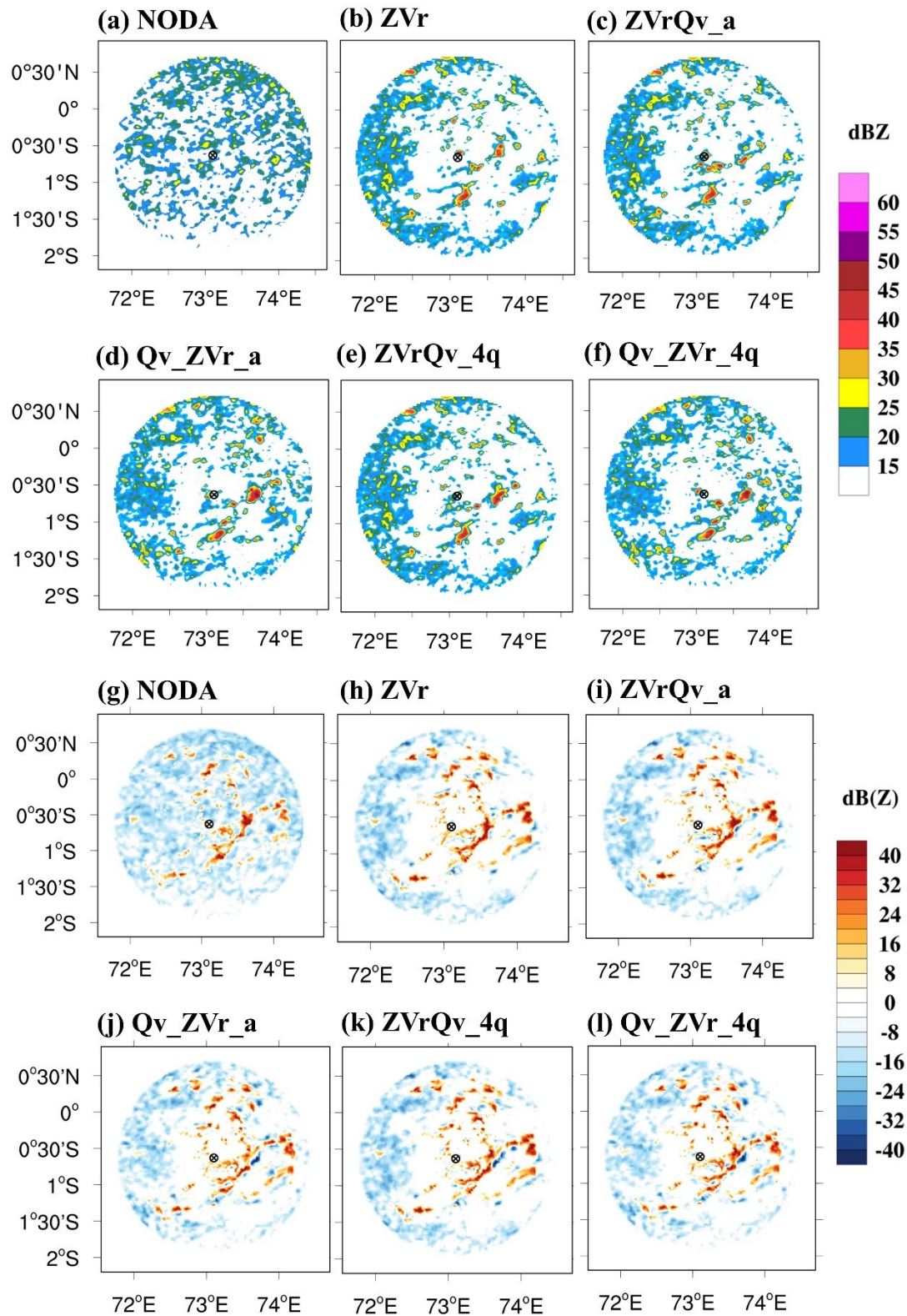


Figure 2.10: As in Fig. 2.8, but for the third case at 1230 UTC 12 Oct 2011.

Table 2.3: RMSEs of the Z , V_r (compared with S-band radar), and Q_v (compared with S-PolKa-retrieved Q_v) at the final analysis cycle for the three cases. The smallest RMSEs of these three variables in each case are indicated in bold font.

		ZVr	ZVrQv_a	Qv_ZVr_a	ZVrQv_4q	Qv_ZVr_4q
Case 1	Z (dB(Z))	9.5	9.2	7.2	8.5	7.1
	V_r (m s ⁻¹)	2.0	1.9	1.9	1.9	1.8
	Q_v (g kg ⁻¹)	2.8	2.7	2.7	2.8	2.6
Case 2	Z (dB(Z))	10.5	10.1	8.1	10.2	7.9
	V_r (m s ⁻¹)	2.0	1.9	1.8	1.9	1.8
	Q_v (g kg ⁻¹)	2.7	2.5	2.3	2.5	2.3
Case 3	Z (dB(Z))	19.3	18.1	16.4	17.3	16.7
	V_r (m s ⁻¹)	2.1	2.1	2.1	2.2	2.2
	Q_v (g kg ⁻¹)	3.1	2.6	2.4	2.7	2.9

2.4.2 Performance of the short-term deterministic forecast

The analysis results revealed the outperformance of the data assimilation experiments (i.e., ZVr, ZVrQv_a, ZVrQv_4q, Qv_ZVr_a, and Qv_ZVr_4q) compared with the NODA experiment. Therefore, we focused on evaluating the short-term forecast performance of the data assimilation experiments. Figure 2.11 depicts the 3-h (from 1800 to 2100 UTC 18 October 2011) accumulated rainfall in the first case. Compared with the radar-derived total rainfall (Dolan et al. 2017; Fig. 2.11a), all data assimilation experiments predicted heavy rainfall in this event. In addition, these experiments exhibited similar rainfall patterns to the observation despite some overestimated areas (Figs. 2.11b–f). The more accurate analysis of the Z , V_r , and Q_v in experiments Qv_ZVr_a and Qv_ZVr_4q (Table 2.3, Figs. 2.8j,l) resulted in more precise heavy precipitation areas than those in experiments ZVr, ZVrQv_a, and ZVrQv_4q (in the north domain, denoted by the black boxes).

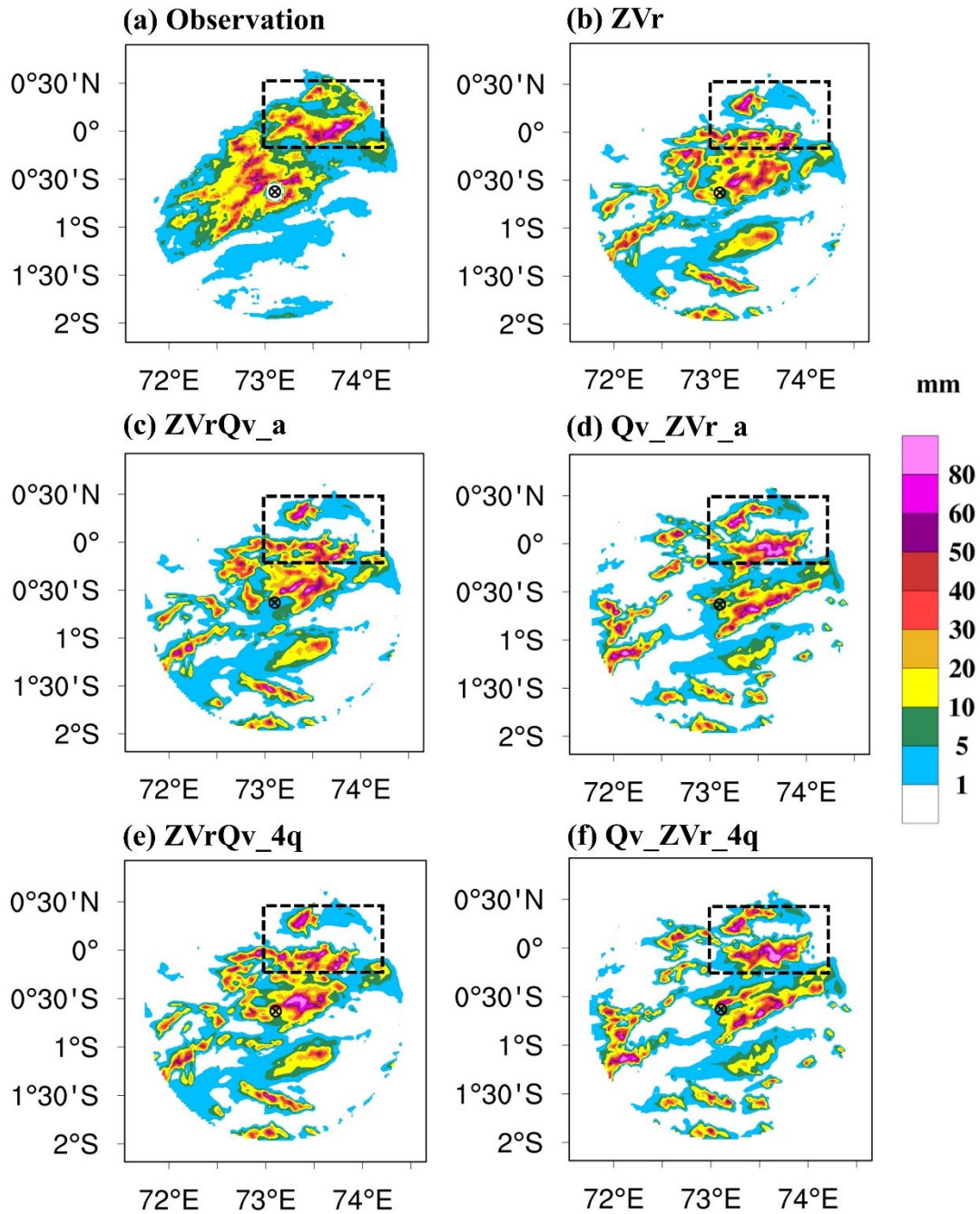


Figure 2.11: Accumulated 3-h rainfall from 1800 to 2100 UTC 18 Oct 2011 for the first case. Observation (a); ZVr (b); ZVrQv_a (c); Qv_ZVr_a (d); ZVrQv_4q (e); and Qv_ZVr_4q (f). The encircled black cross represents the S-PolKa location. The black boxes denote the more accurate heavy rain forecasts of Qv_ZVr_a and Qv_ZVr_4q compared with those of the other experiments.

Figure 2.12 presents the 3-h accumulated rainfall for the second case. As in the first case, all data assimilation experiments predicted heavy rainfall. The main rainband in the northern S-PolKa coverage area was captured in these experiments. However, the forecast rainband moved faster than the observation, resulting in underestimated and overestimated rainfall to the southwest and southeast of the domain, respectively (Figs. 2.12b–f versus Fig. 2.12a). As revealed in the analysis results, experiments Qv_ZVr_a and Qv_ZVr_4q exhibited less overestimation in the southeast corner domain and less underestimation at the most intense convective line to the north of the radar (Figs. 2.9j,l versus Figs. 2.9h,i,k). Therefore, these two experiments alleviated overprediction in the southeast domain and enhanced the intensity of the main rainband (Figs. 2.12d, f). Consequently, among the five data assimilation experiments, Qv_ZVr_a and Qv_ZVr_4q generated the results closest to the observations.

Figure 2.13 details the 3-h cumulative precipitation distribution for the third case. All data assimilation experiments (Figs. 2.13b–f) could predict heavy rainfall greater than 20 mm. However, the location of the scattered convective system was difficult to identify accurately. Compared with experiment ZVr , more heavy rain was forecast in the southeast domain in all Qv assimilation experiments (Figs. 2.13c–f versus Fig. 2.13b). The most complete and heaviest rainfall occurred in Qv_ZVr_a and Qv_ZVr_4q (Figs. 2.13d,f), which generated results that were the most consistent with the observation. This may link to the closer analysis of Qv_ZVr_a and Qv_ZVr_4q to the observation compared with that of ZVr , $ZVrQv_a$, and $ZVrQv_4q$ (Figs. 2.10j,l versus Figs. 2.10h,i,k).

Based on the qualitative evaluation of the accumulated rainfall of these three cases, the enhancement of applying the Z , Vr , and retrieved Qv information for assimilation was demonstrated. Additionally, the assimilation of the Qv with radar data for the entire 2 h resulted in suboptimal rain prediction compared with only assimilating the Qv prior to Z and Vr assimilation in the first hour of the assimilation period. To verify the improvement achieved through the assimilation of the extra Qv information, the Fractions Skill Score (FSS), a neighborhood spatial verification method (Roberts and Lean 2008), was applied to examine the QPF quantitatively. The FSS formula is written as follows:

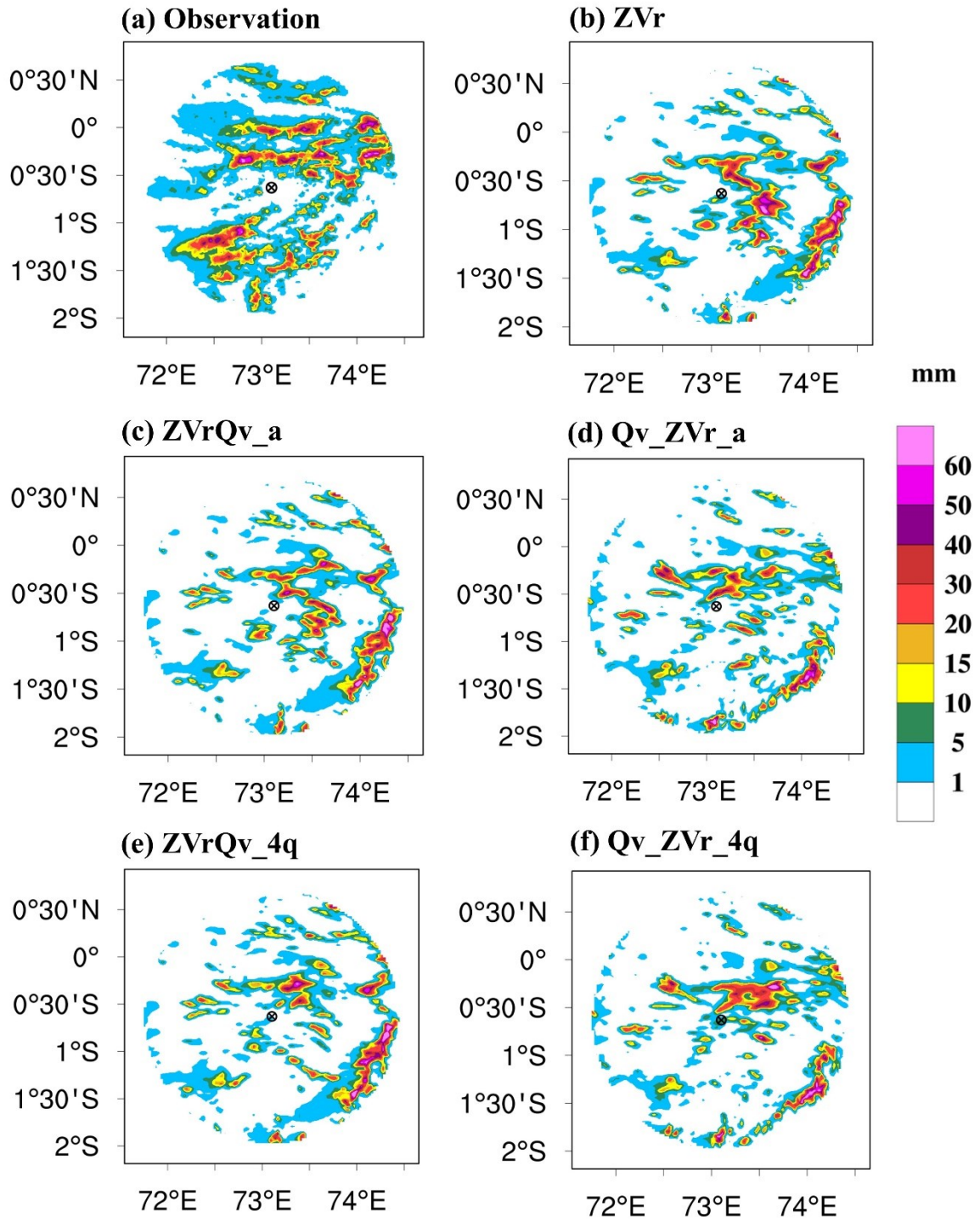


Figure 2.12: As in Fig. 2.11, but for 3 h (from 0200 to 0500 UTC 16 Oct 2011) for the second case.

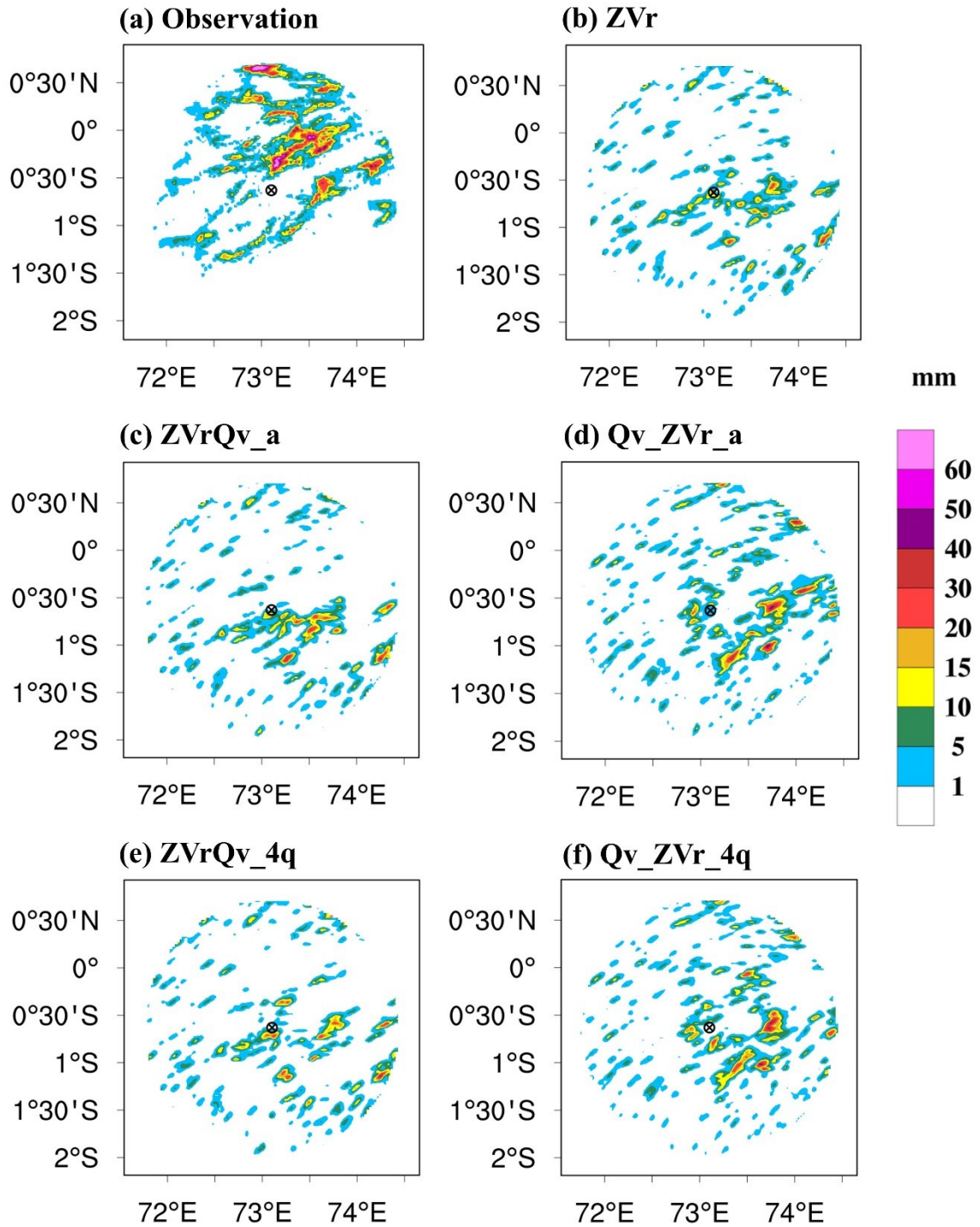


Figure 2.13: As in Fig. 2.11, but for 3 h (from 1230 to 1530 UTC 12 Oct 2011) for the third case.

$$FSS = 1 - \frac{\frac{1}{N} \sum_{i=1}^N (P_f - P_o)^2}{\frac{1}{N} \sum_{i=1}^N P_f^2 + \frac{1}{N} \sum_{i=1}^N P_o^2} \quad (2.15)$$

where P_f and P_o denote the forecast and observed fraction of each neighborhood grid box (five grid points in this study), respectively, and N is the total number of grid points. The value of the FSS ranges from 0 to 1, with 1 representing a perfect forecast and 0 indicating no forecast skill.

Figure 2.14 presents the FSS of accumulated rainfall from 1 to 4 h averaged over the three cases. In general, the FSS decreases with increasing rainfall thresholds. The most obvious enhancement occurred in experiment Qv_ZVr_4q for almost all thresholds throughout the 2-to-4-h forecast. In the comparison among the other four experiments, generally, assimilating either one averaged Q_v profile or four-quadrant Q_v profiles provided higher FSSs than assimilating only the Z and Vr during the first 3 h.

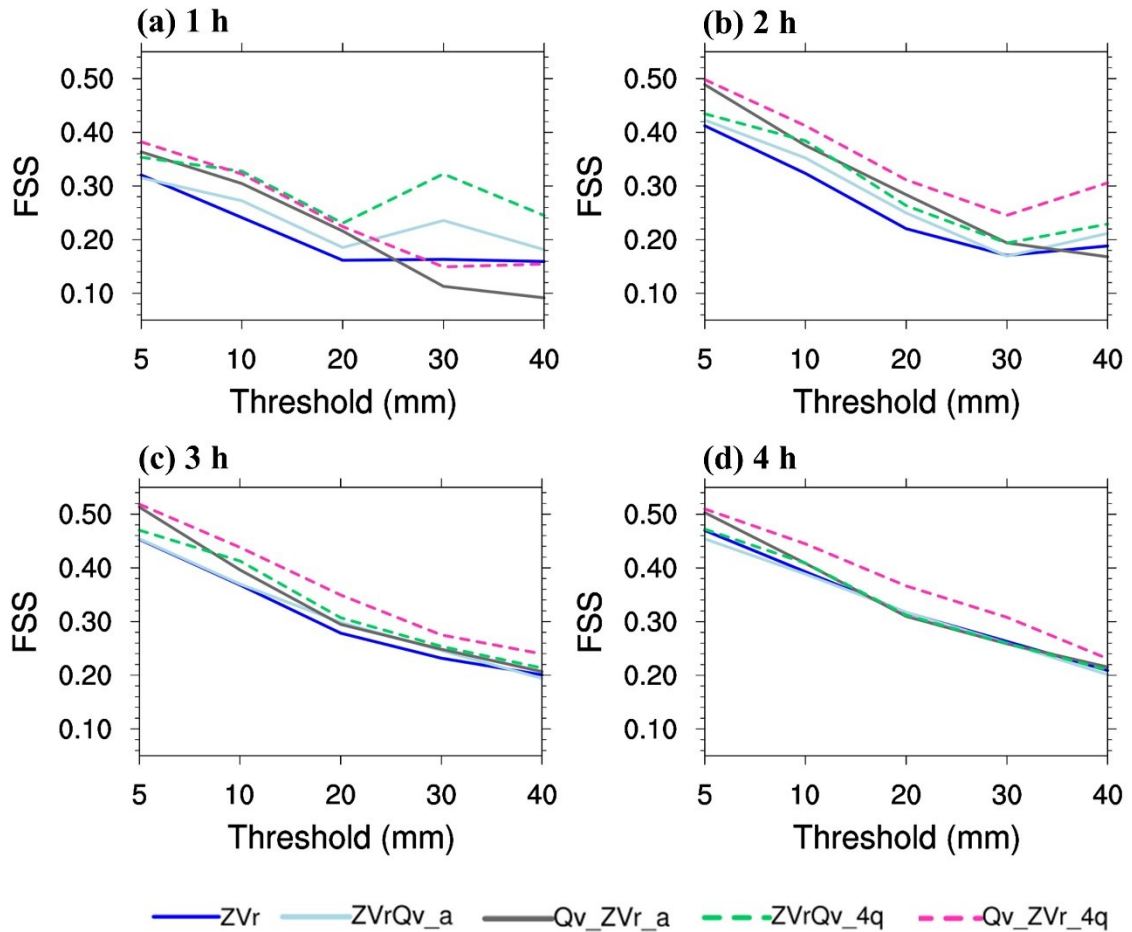


Figure 2.14: The FSS score of the (a) 1-h, (b) 2-h, (c) 3-h, and (d) 4-h accumulated rainfall. Scores are averaged across the three cases.

Furthermore, in the 1-h forecast, assimilating four-quadrant Q_v profiles with Z and V_r for the entire assimilation period produced a more favorable forecasting of heavy rain greater than 20 mm than the assimilation in the other experiments. Moreover, the FSS revealed that the assimilation of four-quadrant Q_v profiles generated more accurate rain forecasts than the assimilation of one averaged Q_v profile.

For further evaluation, the surface and sounding data from the Gan station and the S-PolKa-retrieved Q_v were compared with the output from the data assimilation experiments. Figures 2.15a–e illustrate the RMSEs of the accumulated rainfall and that of the relative humidity (RH), T , U , and V variables at the Gan sounding station. The RMSEs were calculated during 1–4-h forecasts and were averaged across the three cases. In the prediction of accumulated rainfall at the Gan station (Fig. 2.15a), experiments $Q_v_ZVr_a$ and $Q_v_ZVr_4q$ exhibited lower RMSEs than the other three experiments during the 4-h forecast; the most accurate forecast was generated in the $Q_v_ZVr_a$ experiment. Among the other three experiments, $ZVrQv_4q$ had the lowest RMSE in the first 2 h, but the RMSE later increased, eventually becoming the largest RMSE in the last 2 h. In comparison with the Gan sounding data (Figs. 2.15b–e), in general, all experiments that assimilated the additional Q_v alternately offered the lowest RMSEs for the RH , T , U , and V during the first 3-h forecast, except for the least accurate forecast of the V in experiment $ZVrQv_4q$. Because the S-PolKa-retrieved Q_v was unavailable for the 4-h forecast time in the first and second cases, the Q_v RMSE was only calculated for the third case, as detailed in Fig. 2.15f. The results revealed that more improvement in the Q_v forecast was achieved in experiments $Q_v_ZVr_4q$ and $Q_v_ZVr_a$ in the first 2 h. In the last 2 h, lower RMSEs were exhibited in experiments $ZVrQv_a$ and $ZVrQv_4q$.

The quantitative evaluation results further verified the effect of assimilating radar data and the S-PolKa-retrieved Q_v for convective scales. The assimilation of Z and V_r with the retrieved Q_v generates more accurate forecasts than the assimilation of Z and V_r only. Optimal forecasts can be obtained if the retrieved Q_v is assimilated before Z and V_r in the first hour of the assimilation period. Furthermore, the assimilation of four-quadrant Q_v profiles resulted in more accurate forecasts than the assimilation of one averaged Q_v profile.

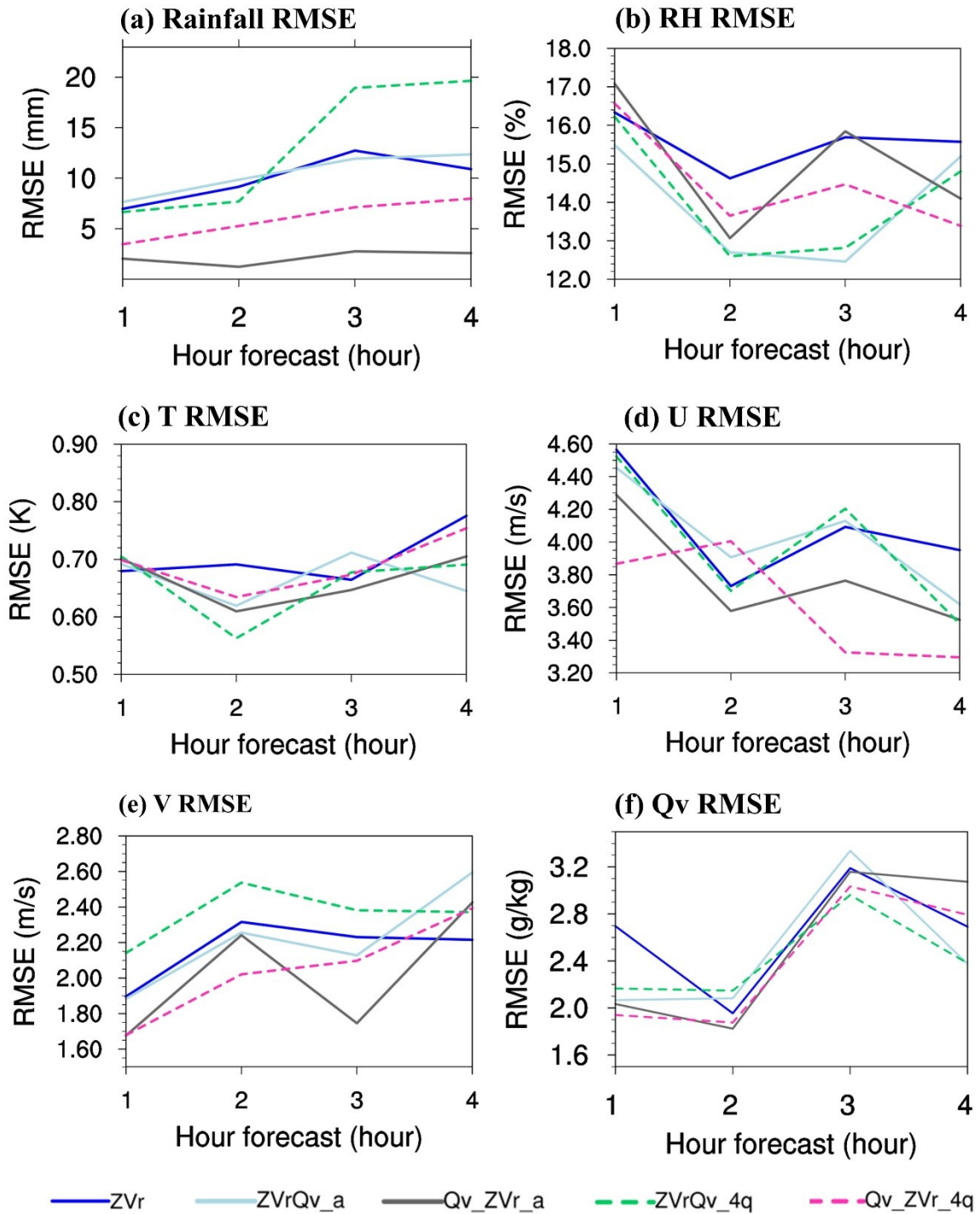


Figure 2.15: The 1–4-h RMSEs of the data assimilation experiments of (a) accumulated rainfall compared with surface rainfall at the Gan station; (b–e) the RH , T , U , and V compared with the Gan sounding station data, averaged for the entire profile; and (f) the Q_v compared with the S-PolKa–retrieved Q_v . The Q_v RMSE is only calculated for the third case; other RMSEs are averaged across the three cases.

2.5 Summary and Conclusions

This study examined the assimilation of the Z , Vr , and retrieved Qv from the NCAR S-PolKa radar in convective forecasts. The retrieved Qv was thinned into one averaged Qv and four-quadrant Qv profiles and then assimilated using two strategies. Three real cases comprising two heaviest rain events and one scattered convection event in the DYNAMO campaign were examined. For each case, six experiments were conducted using the WLRAS. All data assimilation experiments consisted of 2-h assimilation with 15-min frequency and 6-h deterministic forecasts. Our main conclusions are summarized as follows:

- (1) For the retrieved Qv , assimilating thinned humidity information into four quadrants provided a more effective analysis than assimilating the information in one averaged Qv profile, leading to a more markedly improved QPF in $ZVrQv_4q$ and Qv_ZVr_4q than that in $ZVrQv_a$ and Qv_ZVr_a , respectively. The performance results were particularly obvious in the second case because of the greater variety of humidity profiles in different directions in this case.
- (2) The S-PolKa–retrieved Qv was only available when the precipitation system approached but did not cover the radar site. Therefore, the following two strategies were applied when conducting experiments: assimilating the retrieved Qv , Z , and Vr for the entire assimilation period, and assimilating only the retrieved Qv beforehand in the first hour of the assimilation period. Both approaches can more effectively improve the analysis of the environmental moisture nearby precipitation system compared with only assimilating the Vr and Z . In addition, more precise moisture adjustments were obtained when only the retrieved Qv was assimilated in the first hour of the assimilation period prior to other assimilation processes. Consequently, experiments Qv_ZVr_a and Qv_ZVr_4q exhibited more accurate analysis fields than other experiments as compared to the observation. The qualitative and quantitative evaluation for the short-term forecasts indicated that additionally assimilating the Qv with Z and Vr could improve the QPF and obtain a higher FSS in the 0-to-3-h forecast lead time compared with assimilating only the Z and Vr . The two experiments that assimilated the retrieved Qv alone in the first hour of the assimilation period generated the most comparable rainfall to the observations in terms of intensity and pattern, resulting in their highest FSSs. When further compared with the surface observation, sounding data, and S-PolKa–retrieved Qv , the results

demonstrated that the experiments assimilating the retrieved Q_v improved the short-term forecast of wind, temperature, and humidity at least up to 3 h. Overall, the assimilation of the additional S-PolKa-retrieved Q_v is beneficial for short-term forecasting.

Chapter 3. Impact of Radar-Derived Refractivity Assimilation on the Quantitative Precipitation Forecast: Real Cases Study of SoWMEX

Radar-derived refractivity carries moisture information near the surface which plays a crucial role in the convective initiation and heavy rain prediction. This study aimed in investigating 1) the effect of assimilating radar-retrieved refractivity along with reflectivity and radial wind and 2) the refractivity assimilation before and after the weather system landed. The high-resolution WRF local ensemble transform Kalman filter data assimilation system was employed for two cases in the Southwest Monsoon Experiment. The results of two cases revealed that assimilating only reflectivity and radial velocity could modify the near-surface humidity based on the flow-dependent error correlation estimated by the ensemble, but the spatial distribution is not fully accurate, causing the rainfall underestimation. With additional refractivity assimilation, stronger convergence and the optimal corrections of low-level moisture, temperature, and wind fields were obtained, leading to better forecasts for both light and heavy rainfall during 6 h. Additionally, the positive impact of refractivity assimilation is particularly significant in dry-biased background moisture with broader refractivity distribution. Based on the feature of the weather systems, the first case was utilized to examine the refractivity assimilation in different stages of the convection. The results indicated that continuing the assimilation of extra refractivity after the weather system landed could more accurately capture moisture and enhance wind convergence than without refractivity assimilation, resulting in further improvement of the short-term forecast. Moreover, the results suggested assimilating the refractivity before the weather system landing to achieve optimal quantitative precipitation forecasting.

3.1 Introduction

Heavy rainfall events usually accompany flooding that causes life loss and property destruction. The accurate heavy rain forecast is crucial but still a long-lasting scientific challenge in weather forecasting despite the advantage of numerical weather prediction (NWP). To enhance the heavy rainfall forecast, the combination of a high-resolution dynamic model, a data assimilation system, and the available high spatial and temporal resolution observations is the key (Miyoshi et al. 2016). Radar data is one of the information that is ingested in various assimilation systems with different algorithms and improves heavy rainfall prediction. Several studies pointed out the advantages of radar assimilation in different algorithms [e.g., 3DVAR algorithms: Xiao and Sun (2007); Chung et al. (2009); Li et al. (2020); Zhao et al. (2012); 4DVAR algorithms: Sun and Crook (1997); Sun and Zhang (2008); Sun et al. (2010); Thiruvengadam et al. (2020); ensemble-based data assimilation systems: Snyder and Zhang (2003); Tong and Xue (2005); Yussouf and Stensrud (2010); Dowell et al. (2011); Tsai et al. (2014); Yokota et al. (2018); Wang et al. (2021); the hybrid assimilation system: Li et al. (2012); Gao et al. (2013); Gao and Stensrud (2014); Li et al. (2015)].

Although assimilating radar data (Z and Vr) can enhance the NWP performance, these data are only available after the convection begins to develop and cannot fully adjust the water vapor field and guarantee obtaining an optimal convective forecast. Various studies made efforts to overcome the limitations by assimilating different sources of moisture information. Lai et al. (2019) through the assimilation of derived vertically integrated liquid water from three-dimensional Z indicated the ability to lessen the storm cell overprediction. The rainfall observed by radar and surface observations was assimilated in the study of Sun et al. (2020), which pointed out the crucial role of rainfall data in correcting the humidity and temperature. Besides the moisture information retrieved inside the precipitation system, the assimilation of humidity data nearby the precipitation system was also examined. Do et al. (2022) figured out the short-term forecast improvement by assimilating S-PolKa-retrieved water vapor which provides environmental information before precipitation occurs. These studies proved the positive impact of assimilating humidity information on QPF but the utilized moisture data are only available inside precipitation systems or before the weather systems approach. The assimilation of moisture in both periods (before and after convection landing) has not been comprehensively investigated.

On the other hand, many studies indicated that the high spatiotemporal resolution

of near-surface moisture is crucial for improving initial conditions in the storm-scale forecast (Fabry and Sun 2010; Hanley et al. 2011; Ha and Snyder 2014; Madaus and Hakim 2016). The low-level moisture variability is sensitive to the convective initiation and impacts the QPF. A variation of moisture within 1 g kg^{-1} can determine the occurrence or nonoccurrence of storm initiation (Crook 1996). Moreover, the resolution of 100-m spatial and 10-min temporal are necessary for moisture measurement in the boundary layer (Weckwerth 2000). However, the measurements for providing high spatial and temporal resolution of moisture information are limited. Although the surface-based observing networks (i.e., surface mesonet and thermodynamic profiles) can provide low-level moisture information (Wulfmeyer et al. 2015; Brotzge et al. 2020), they are only available for certain regions and field experiments. Radiosondes, which are the traditional measurement of achieving humidity information, are inadequate because of their widely distributed locations and sparse temporal resolution. An alternative approach is remote sensing with higher spatial resolutions of moisture information but its ability is limited in environments with clouds and precipitation (Lindsey et al. 2018; Zhu et al. 2020).

Fabry et al. (1997) introduced a method for retrieving refractivity (N) of near-surface air by weather radars. The N information is available for both before and after the landing of the weather system. The concept is based on the phase change detected from the stationary target located in the vicinity of the radar site. The radar-retrieved N field represents air moisture at about 20 m above the ground and covers about a 40-km range from the radar location (Feng et al. 2021). In the warm condition, N can be utilized as the proxy for two-dimensional near-surface moisture distribution. Additionally, in the afternoon, during the well-mixed boundary layer condition, the N can exhibit atmospheric conditions through the height of 200 m from the surface (Weckwerth et al. 2005). The moist (dry) air is represented by the high (low) N values. The spatial and temporal resolutions of N vary with different scan strategies, and clutter target density (Feng and Fabry 2018). Generally, the spatial and temporal N resolutions are approximately 2–4 km and 4–10 min, respectively.

Many attempts have been made to employ N to correct the initial humidity field in the NWP model via data assimilation. Montmerle et al. (2002) modified the moisture in the lowest model level based on the N . Consequently, the near-surface humidity was enhanced and the more intense convections were generated, leading to closer rain forecasts to the observation. Sun (2006) inferred and assimilated the moisture

information in the low level from the N obtained in the International H2O Project (IHOP 2002). The results revealed that the assimilating humidity data resulted in the enhancement of moisture variability and convection initiation. In the study of (Gasperoni et al. 2013), by assimilating the simulated N data in the Observing system simulation experiments (OSSEs), the low-level moisture errors were reduced, resulting in the improvement of the convective initiation forecast. Seko et al. (2017) conducted the experiments of assimilating temporal variations of N obtained by operational Doppler radar in the Local Ensemble Transform Kalman Filter system. The study pointed out the positive impact of N assimilation on the adjustment of water vapor distribution and QPF improvement.

Despite proving the critical role of N assimilation, most of the aforementioned studies only focused on examining the effect of assimilating N and applied it in midlatitude regions. The assimilation of N with Z and Vr in the tropical region and the strategy to optimize the positive impact of N assimilation on the QPF have not been investigated. Additionally, WMO (2015) encouraged more studies related to the N assimilation for real cases in the operational high-resolution nowcasting NWP model. Therefore, in this study, the N retrieved from the S-band polarimetric Doppler radar of the National Center for Atmospheric Research (NCAR S-Pol) in the Terrain-influenced Monsoon Rainfall Experiment/Southwest Monsoon Experiment (TiMREX/SoWMEX) in southwestern Taiwan in 2008 was assimilated with a high horizontal resolution model (i.e., 1 km). The first objective of this study was to evaluate the impact of assimilating N along with Z and Vr on the QPF in the tropical region. Based on the characteristic of N , the second objective was to investigate the N assimilation before and after the weather system landed, which has not been extensively examined. Two heavy rain events from SoWMEX were employed in this study with a series of experiments. Section 3.2 describes the two cases and the observations utilized for assimilation. The assimilation system and experimental design are described in section 3.3. The results of N assimilation are analyzed in section 3.4. The final section of this chapter gives the summary and conclusion of the study.

3.2 Study cases and assimilation observations

3.2.1 The two heavy rainfall events of SoWMEX: 02 June and 14 June 2008

For evaluating the impact of assimilating additional N information on the heavy rainfall forecast, two events of the SoWMEX were utilized in our study. The SoWMEX campaign was operated in southwestern Taiwan from May to Jun 2008 to investigate the dynamic and thermodynamic characteristics of heavy rainfall during the southwesterly

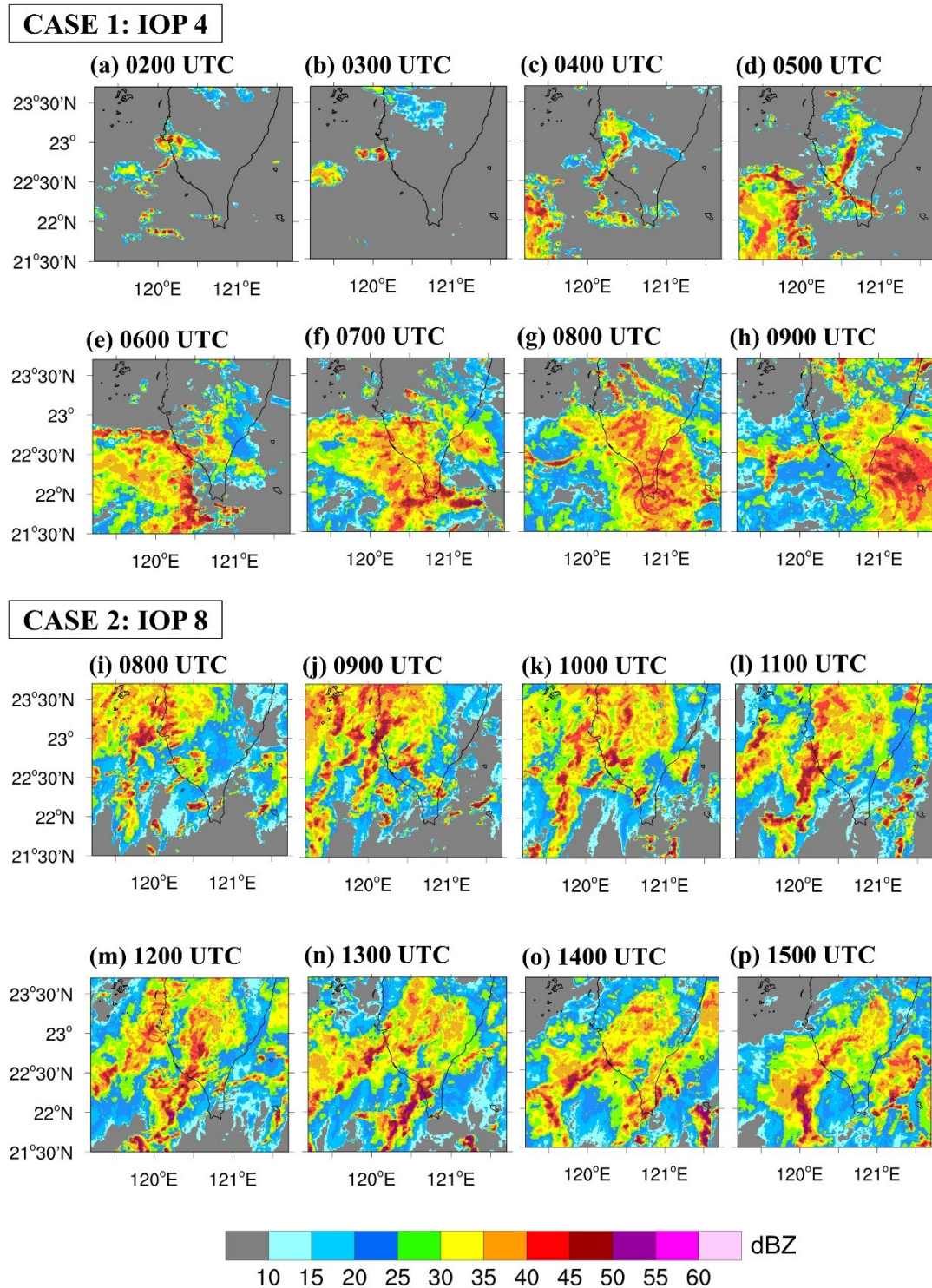


Figure 3.1: The Quantitative Precipitation Estimation and Segregation Using Multiple Sensors (QPESUMs) observation of two cases: (a–h) the first case from 0200 to 0900 UTC 02 Jun 2008 and (i–p) the second case from 0800 to 1500 UTC 14 Jun 2008.

season for the QPF improvement (Davis and Lee 2012). A heavy rain event with more than 6-h duration caused by synoptic-scale forcing was determined as intensive observation periods (IOPs). In this study, IOP 4 and IOP 8 were selected for investigation. The main experiment period of the first case (i.e., IOP 4) was from 2100 UTC 1 June to 1500 UTC 3 June 2008. In this IOP, a stationary front was across Taiwan. Several convections appeared over the ocean, moved easterly toward Taiwan, and then interacted with the topography (Figs. 3.1a–h). The 12-h accumulated rainfall in central mountain Taiwan from 0000 to 1200 UTC on 02 June 2008 was recorded as over 100 mm (Fig. 3.2a). The second case (i.e., IOP 8) began at 0000 UTC 14 June and finished at 0000 UTC 16 June 2008. A front system associated with the north-south-oriented squall line went through Taiwan on 14 June. The southwesterly winds brought moisture from the ocean and moved toward the east and southeast, resulting in heavy rain on the island (Figs. 3.1i–p). The 12-h accumulated rainfall from 0600 to 1800 UTC on 14 June 2008 was more than 100 mm in southwestern Taiwan, especially, the approximate 200-mm rainfall was recorded in some places (Fig. 3.2b).

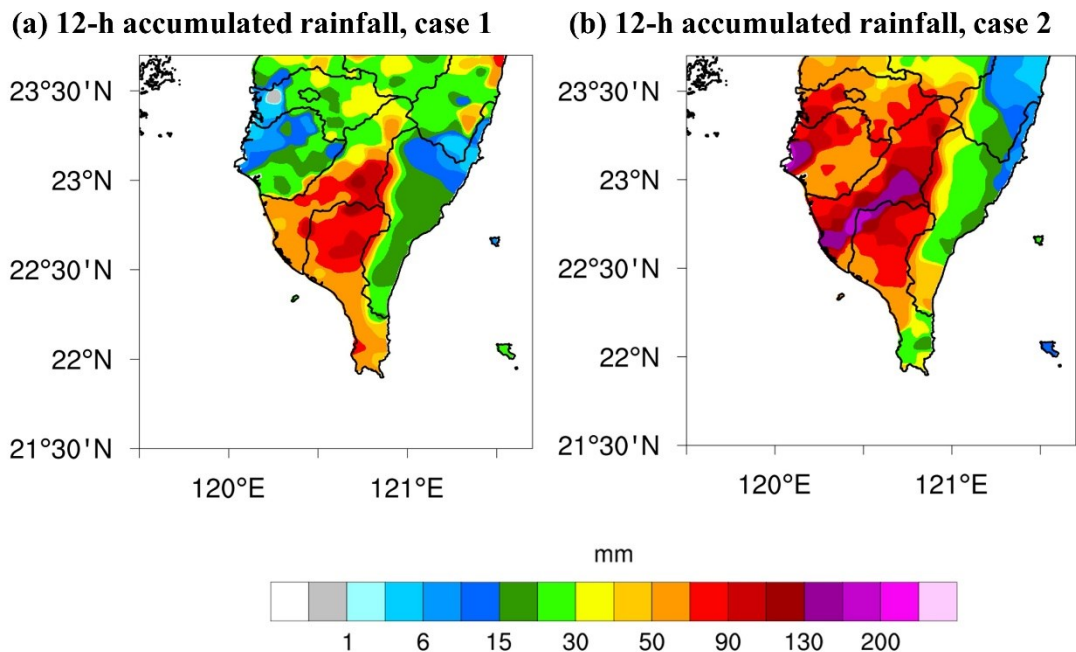


Figure 3.2: The 12-h accumulated rainfall of (a) the first case from 0000 to 1200 UTC 02 Jun 2008; (b) the second case from 0600 to 1800 UTC 14 Jun 2008.

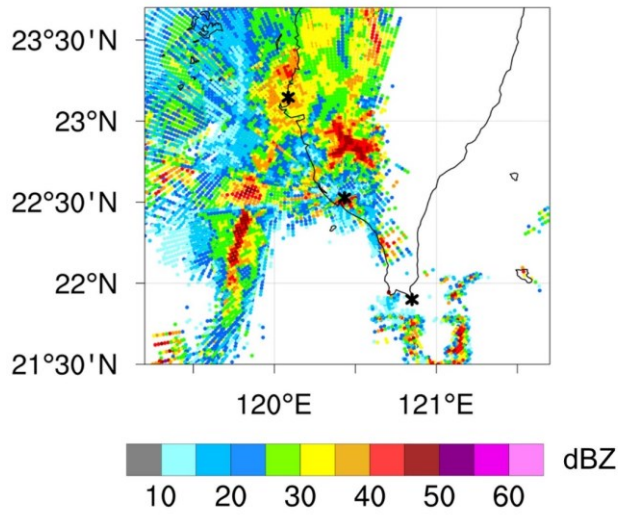
3.2.2 Observations for assimilation

The Z and V_r data used for assimilating were from the Central Weather Bureau (CWB) S-band ground-based Doppler radars [Kentin (RCKT), Chigu (RCCG)], and the NCAR S-Pol radar. Before assimilating, all data underwent quality control processes,

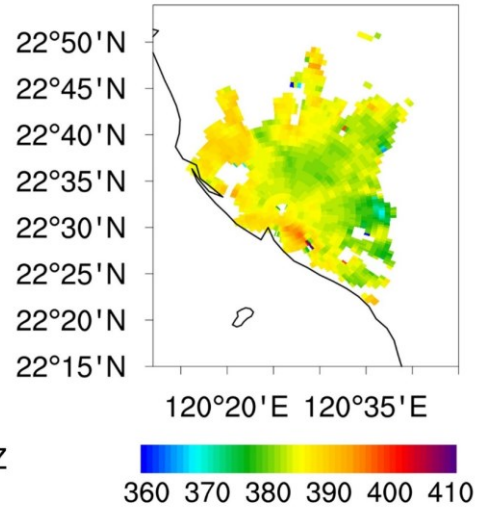
including removing the ground cluster, sea cluster, and noise signal, filtering out the non-meteorological signals, and velocity unfolding, provided by the Radar Meteorology Laboratory at National Central University, Taiwan. For thinning data to avoid spatial correlation between observations, this study adopted the super-observation method (Lindskog et al. 2004; Alpert and Kumar 2007), in which the resolution of 2 km along the radial direction and 2° in the azimuth angle were applied to grid the Z and V_r . Figure 3.3a displays the coverage of three radars in the study domain and the example of superobbing.

For the N observation, Fabry et al. (1997); Feng et al. (2016); Feng and Fabry (2018) gave comprehensive descriptions of N estimation near the surface air by using the Doppler weather radar. This study employed the N fields retrieved by the NCAR S-Pol radar for assimilation (<https://doi.org/10.5065/D6WH2N9T>). The N dimension was 480×300 (480 azimuth angles with a resolution of 0.75-degree, 300 gates with 0.15 km interval). Feng et al. (2021) characterized the N fields in the SoWMEX field experiment. The N was higher in the convective environments than in the non-precipitation environments. Additionally, N increased ahead of the moving in the convective system and changed with the environmental dominant wind. The range of N was from 350 to 405 N-unit and the difference of N compared with the surface stations was about 4.1 N-unit on average. The N observations of the two study cases are described in Fig. 3.4, which were plotted every 30 minutes from 0300 to 0600 UTC in IOP 4 and 0900 to 1200 UTC in IOP 8. The N distribution in the first case (Figs. 3.4a–g) was broader than in the second case (Figs. 3.4h–n). Moreover, compared with IOP 8, the humidity field in IOP 4 evolved faster, which corresponded with the rapid growth and movement of convection (Fig. 1a–h). Before including the N information in assimilating process, this data was thinned by re-gridding into 1.5 degrees in azimuth angle and 1.5 km along the radial direction (Fig. 3.3b). The temporal resolution of N used in our study was 15 minutes, with the coverage within 40 to 60 km.

(a) Example of radar data superobbing



(b) Example of N superobbing



(c) Locations of radars and sounding stations

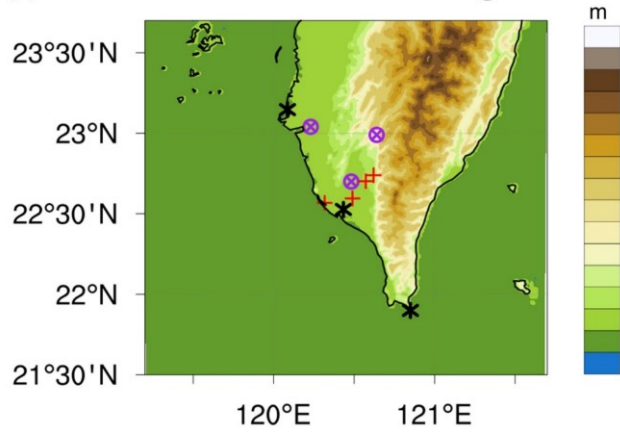


Figure 3.3: (a) Example of radar data superobbing at 0.5 elevation angle; (b) Example of *N* superobbing; (c) Locations of sounding (encircled purple crosses) and surface (red crosses) stations utilized for forecast verification. The black stars in (a) and (c) denote the radar locations. These figures were plotted at 1000 UTC 14 Jun 2008.

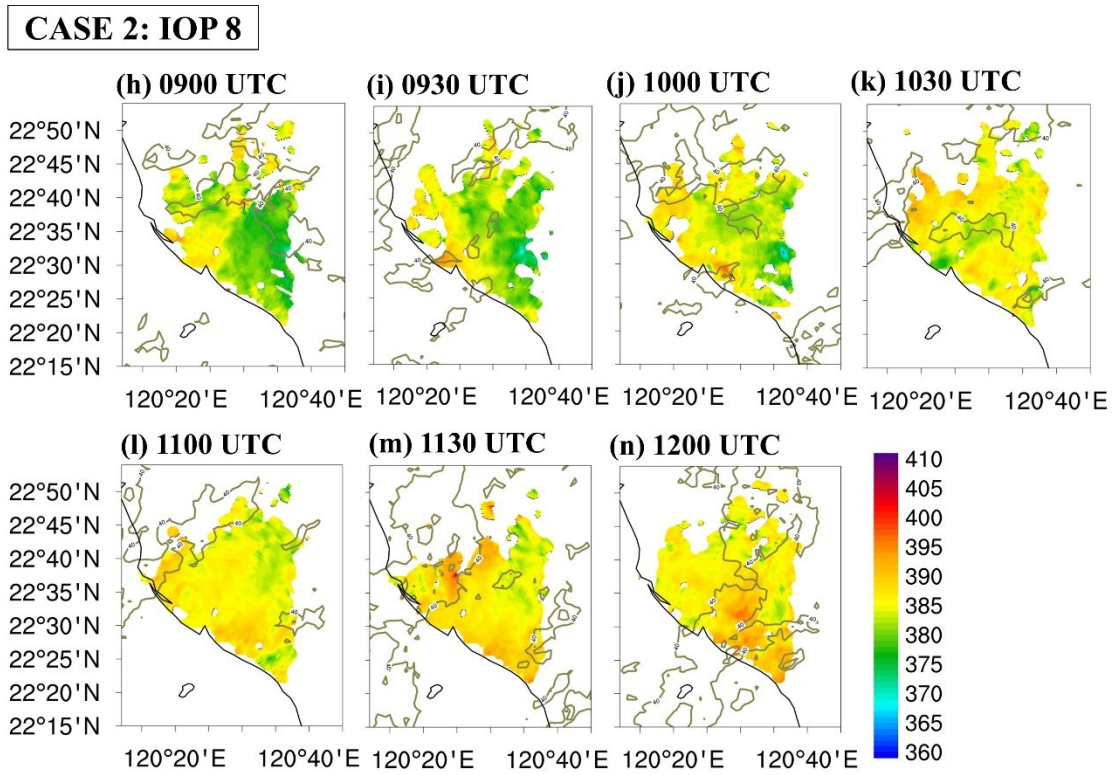
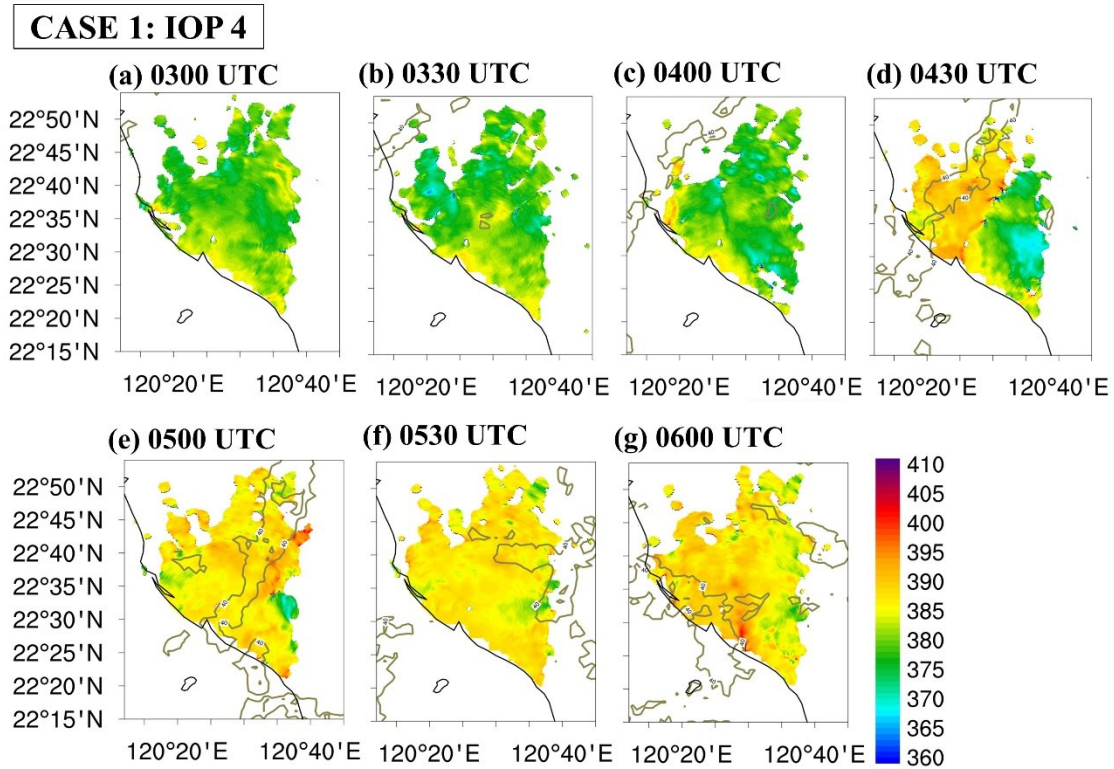


Figure 3.4: The N (color shading) and Z (> 40 dBZ, gray contours) observations (every 30 minutes) for two cases: (a–g) the first case from 0300 to 0600 UTC 02 Jun 2008 and (h–n) the second case from 0900 to 1200 UTC 14 Jun 2008.

3.3 Assimilation system and experimental design

3.3.1 Model configuration

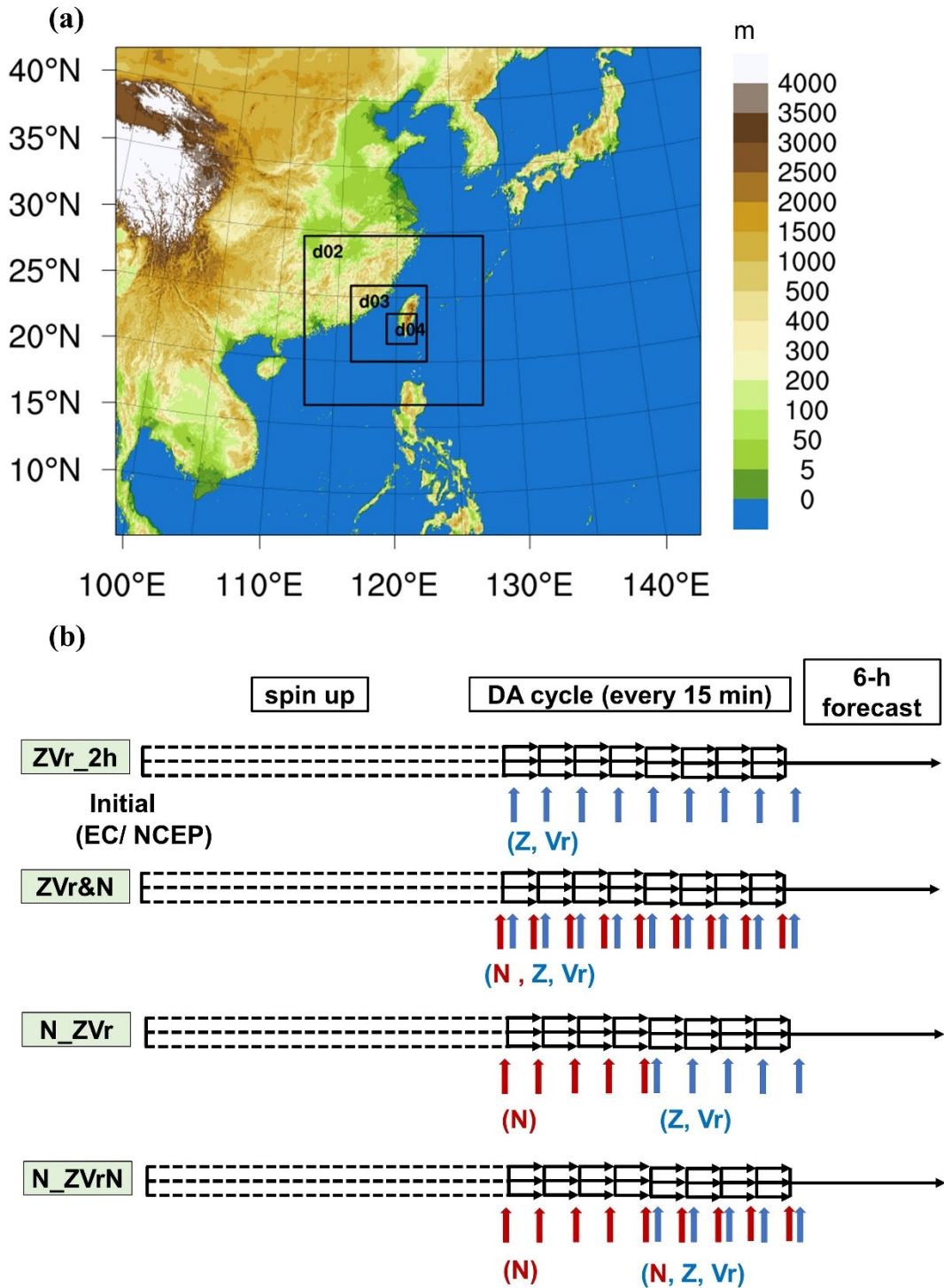


Figure 3.5: (a) The WRF model domains setting in this study. The horizontal grid spacing of domains 1, 2, 3, and 4 are 27 km (181×151 points), 9 km (166×157 points), 3 km (211×211 points), and 1 km (250×250 points), respectively. (b) The schematic of experiments design. The triple dash lines indicate the model spin-up period, the triple and single solid lines stand for the data assimilation period and the mean forecast, respectively. The vertical blue arrows denote Z and Vr observations, and the vertical red arrows refer to N observations utilized for assimilation.

This study employed the two-way interacted WRF model version 3.9.1 to execute all experiments. There were four domains with different horizontal resolutions as 27, 9,

3, and 1 km applied for domain 1 (181×151 grid points), domain 2 (166×157 grid points), domain 3 (211×211 grid points), and domain 4 (250×250 grid points), respectively (Fig. 3.5a). The innermost domains cover the southern part of Taiwan. The vertical level between the surface and 10 hPa was 52 levels. For the physical parameterization, the model used the Rapid Radiative Transfer Model (RRTM) longwave radiation scheme (Mlawer et al. 1997), the Dudhia shortwave radiation scheme (Dudhia 1989), the Yonsei University (YSU) planetary boundary layer scheme (Hong et al. 2006), the Grell–Devenyi cumulus schemes (Grell and Dévényi 2002), and the Goddard Cumulus Ensemble (GCE) scheme (Tao et al. 2003).

3.3.2 WRF-Local ensemble transformed Kalman filter Radar Assimilation System

The study utilized the WRF Local Ensemble Transform Kalman Filter Radar Assimilation System (WLRAS; Tsai et al. 2014) to conduct all experiments. This system was the extension of the coupling local ensemble transform Kalman filter (LETKF) with the WRF model (Yang et al. 2009) to assimilate radar data. The WLRAS updated the wind, geopotential height, potential temperature perturbation, and mixing ratios of water vapor (Q_v) and hydrometers through the cross-variable background error correlations. Different model variables had appropriate error covariance localization radii to define the distance for selecting observation to obtain a more efficient adjustment of variables. In this study, localizations set up for the system were based on Tsai et al. (2014). The horizontal localization was set as 36 km for horizontal wind, 24 km for temperature, the hydrometeor mixing ratio of cloud, and Q_v , and 12 km for vertical velocity, the hydrometeor mixing ratio of rain, snow, and graupel. For the vertical localization, all variables applied the same radii as 4km. In addition, the V_r , Z , and N observation errors were assigned as 3 m s^{-1} , 5 dB(Z) (Tsai et al. 2014), and 4.1 N-unit (approximately 0.8 g kg^{-1} ; Feng et al. 2021), respectively.

3.3.3 Observation operators

The wind components in the model are converted into V_r by the forward model as follows:

$$V_r = [ux + vy + (w - V_t)z] (x^2 + y^2 + z^2)^{-1/2} \quad (3.1)$$

$$V_t = 5.40 \left(\frac{p_0}{p} \right)^{0.4} (\rho_a q_r)^{0.125} \quad (3.2)$$

where x , y , and z denote the Cartesian coordinates with the origin at the radar site, u , v , and w stand for the zonal, meridional and vertical wind, p_0 and \bar{p} are the surface pressure and the base-state pressure, ρ_a is the air density, q_r is the hydrometeor mixing ratio of rain.

The Z which is the sum of the contribution from rainwater (Z_r), snow (Z_s), and graupel (Z_g) (Dowell et al. 2011), were computed as follows:

$$Z = Z_r + Z_s + Z_g \quad (3.3)$$

This study utilized the three-ice scheme of GCE, so three factors in Eq. (3.3) were defined as:

$$Z_r = 3.63 \times 10^9 (\rho_a q_r)^{1.75} \quad (3.4)$$

$$Z_s = 1.21 \times 10^{11} (\rho_a q_s)^{1.75}, \quad (T > 0^\circ C), \quad (3.5)$$

$$Z_s = 2.79 \times 10^8 (\rho_a q_s)^{1.75}, \quad (T \leq 0^\circ C), \quad (3.6)$$

$$Z_g = 1.12 \times 10^9 (\rho_a q_g)^{1.75} \quad (3.7)$$

where q_s and q_g are the hydrometeor mixing ratio of snow and graupel.

The observation operator for N is followed Bean&Dutton (1966):

$$N = (n-1) \times 10^6 = 77.6 \frac{P}{T} + 3.73 \times 10^5 \frac{e}{T^2} \quad (3.8)$$

In Eq. (3.8), n denotes the refractive index, P is the atmospheric pressure (hPa), T is the temperature (K), and e is the water vapor pressure (hPa). Among these terms, the refractivity change is the most dominated by the variation of moisture. Feng et al. (2021) state that during the SoWMEX experiment, a change of 3° in T or 1.2 hPa in e (e.g., 1.2 g kg⁻¹ in Q_v) can make a change of 5 N-unit in N . In other words, compared with the temperature change, the moisture change can result in a five-time sensitivity of the N change.

3.3.4 Experimental design

This study applied the WRF Data Assimilation System (WRFDA; Barker et al., 2004) to create 50 ensemble members for domain 1 from the initial conditions. Then, the completed perturbed members were downscaled to finer domains 2, 3, and 4. Before beginning data assimilation, the convective-scale structures in the ensemble perturbations were spun-up by running 11-h (case 1) and 10-h (case 2) ensemble forecasts. Each assimilation experiment was conducted 2-h assimilating in domain 4 with the 15-minute analysis interval (i.e., nine cycles) for each case. After finishing the

assimilation, the obtained ensemble mean analyses were then adopted to accomplish the 6-h deterministic forecast.

To examine the effect of N assimilation in different background moisture, in the first set of experiments, two scenarios were created by utilizing different initial and lateral boundary conditions. Figure 3.6 depicts the comparison of background Q_v and N in the second eta model level between IOP 4 at 0400 UTC 02 June and IOP 8 at 1000 UTC 14 June. The first case used the high resolution ($0.75^\circ \times 0.75^\circ$) of ERA-interim reanalysis data to generate the dry-biased background moisture (Figs. 3.6a,c,e) while the second case utilized the NCEP FNL (Final) Operational Global Analysis data ($1^\circ \times 1^\circ$) to get the wet-biased background moisture (Figs. 3.6b,d,f). Except for the difference in spin-up time and the initial and boundary conditions, the two cases had the same experimental setting. The impact of assimilating additional N information was analyzed based on experiments ZVr_2h and ZVr&N, in which experiment ZVr_2h assimilated Z and V_r , experiment ZVr&N included Z , V_r , and N in the assimilating process (Z and V_r were assimilated sequentially after N assimilation). In the first case, the assimilation time began at 0400 UTC and ended at 0600 UTC, then continued the forecast up to 1200 UTC 02 June 2008. The second case conducted the assimilation from 1000 UTC to 1200 UTC, followed by the 6-h forecast until 1800 UTC 14 June 2008.

For examining the N assimilation before and after the weather system landed, the second set of two experiments (N_ZVr and N_ZVrN) was conducted. Since N information could be obtained both in precipitation and non-precipitation conditions, the scientific issue would be: 1) Whether continuing the assimilation of N field after the precipitation system landed over the island could have added value and 2) How early to assimilate N field over the land could be to optimize the impact of improving QPF at convective scale (beforehand and afterward the landing of the precipitation system). Because of the convection features, the second experimental group was conducted only in IOP 4 with different starting assimilation times (before and after the convection move inland at 0300 and 0400 UTC, respectively; Figs. 3.1b,c). All two experiments assimilated N in the first hour but in the second hour, N_ZVr assimilated Z and V_r while N_ZVrN assimilated Z , V_r , and N . The four experiments were detailed in Table 3.1, and the experimental design scheme was described in Fig. 3.5b.

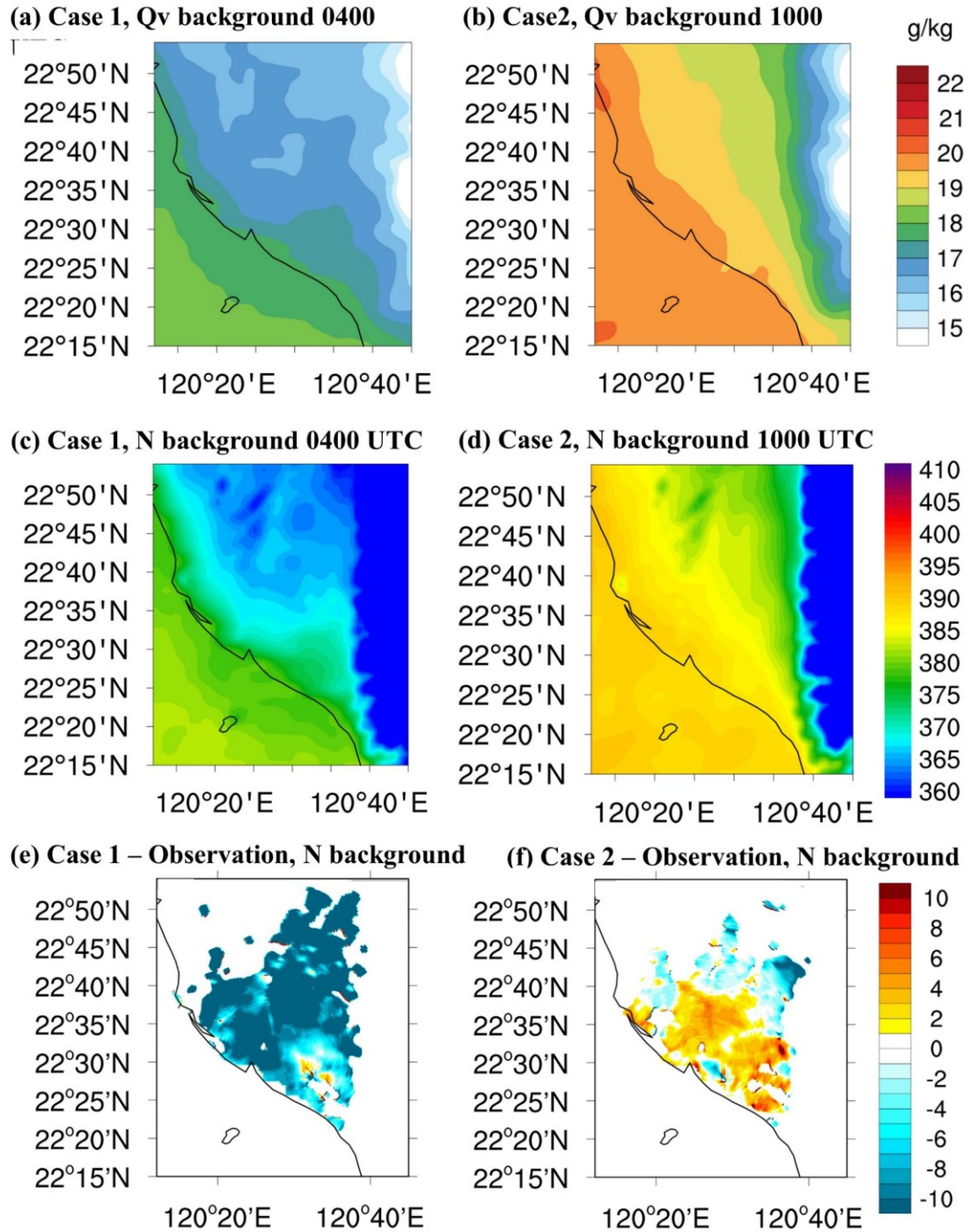


Figure 3.6: The background of Q_v (a,b) and N (c,d) of the first case at 0400 UTC 02 June 2008 (a,c) and the second case at 1000 UTC 14 June 2008 (b,d); the N difference between the observation and the first case (e) and second case (f). These figures were plotted at the second eta model level.

Table 3.1: Summary of experimental design, symbols “x” and “—” denoted the observation was and was not included in the assimilation cycle, respectively.

Set	No.	Experiments	Study cases	Observations assimilated in the first hour			Observations assimilated in the second hour			Assimilation time (UTC)
				Z	Vr	N	Z	Vr	N	
I	1	ZVr_2h	IOP 4	x	x	—	x	x	—	0400 -0600
			IOP 8	x	x	—	x	x	—	1000 -1200
	2	ZVr&N	IOP 4	x	x	x	x	x	x	0400 -0600
			IOP 8	x	x	x	x	x	x	1000 -1200
II	3	N_ZVr	IOP 4	—	—	x	x	x	—	0300 -0500
	4	N_ZVr&N	IOP 4	—	—	x	x	x	x	0300 -0500

3.4 Results

3.4.1 Data and methods for performance verification

The evaluation was based on the observations of N , rain gauge, and sounding data. The N information was retrieved from the NCAR S-Pol. The rain gauge data were interpolated to the 1-km resolution domain 4 to evaluate the QPF. Additionally, the sounding data from three stations (Fig. 3.3c) were used to compare with the forecasted moisture.

The indices utilized for verification include the Root Mean Square Errors (RMSEs), the Fraction Skill Score (FSS; N. M. Roberts & Lean, 2008), and the improvement rate (%) of RMSE and FSS. The RMSE formula is written as follows:

$$RMSE = \sqrt{\frac{\sum (A_P - A_O)^2}{M}} \quad (3.9)$$

In (3.9), A_p and A_o stand for the predicted and observed values for a variable A , respectively, and M denotes the total number of grid points applied for the computation. The FSS is expressed as

$$FSS = 1 - \frac{\frac{1}{N} \sum_{i=1}^N (P_f - P_o)^2}{\frac{1}{N} \sum_{i=1}^N P_f^2 + \frac{1}{N} \sum_{i=1}^N P_o^2} \quad (3.10)$$

In (3.10), the forecast and the observed fraction of each neighborhood grid box (five grid points in this study) are defined by P_f and P_o , respectively, and N is the total number of grid points. The lowest and highest FSS values are 0 and 1, which respectively represent no forecasting skill and a perfect forecast. The improvement rate (%) of RMSE and FSS are computed as follows:

$$RMSE \text{ improvement rate (\%)} = \frac{RMSE_B - RMSE_A}{RMSE_B} \times 100 \quad (3.11)$$

$$FSS \text{ improvement rate (\%)} = \frac{FSS_A - FSS_B}{FSS_B} \times 100 \quad (3.12)$$

The positive and negative values of the improvement rate (%) refer to the improvement and degradation of forecast A compared with forecast B, respectively.

In the rest of section 3.4, the radar-retrieved N assimilation was investigated. The role of assimilating additional N information was examined first by utilizing two cases SoWMEX IOP 4 and IOP 8. In each case, the moisture, temperature, and wind correction of different experiments were examined then followed by the evaluation of the deterministic forecast performance. These techniques were also applied in analyzing IOP 4 for studying the effect of N assimilation before and after the convection system landed.

3.4.2 Results of the first experimental set

3.4.2.1 Case 1: IOP 4

a. Results of the analysis

To examine the ability of additional N assimilation to correct the moisture, temperature, and wind field, the analysis increment of Q_v , T , and wind speed (wspd) of the second eta model level at the first cycle (i.e., 0400 UTC 02 June 2008) are detailed

in Figs. 3.7. In the assimilation of Z and V_r (Fig. 3.7a), the positive Q_v increment appeared near the southwest coast and over south Taiwan, the opposite sign of the Q_v correction occurred in the southwest offshore and mountain area. The temperature field decreased to the northwest domain and increased in the central mountain and the southern coastal area (Fig. 3.7c). Additionally, the wind field in experiment ZVr_2h was adjusted

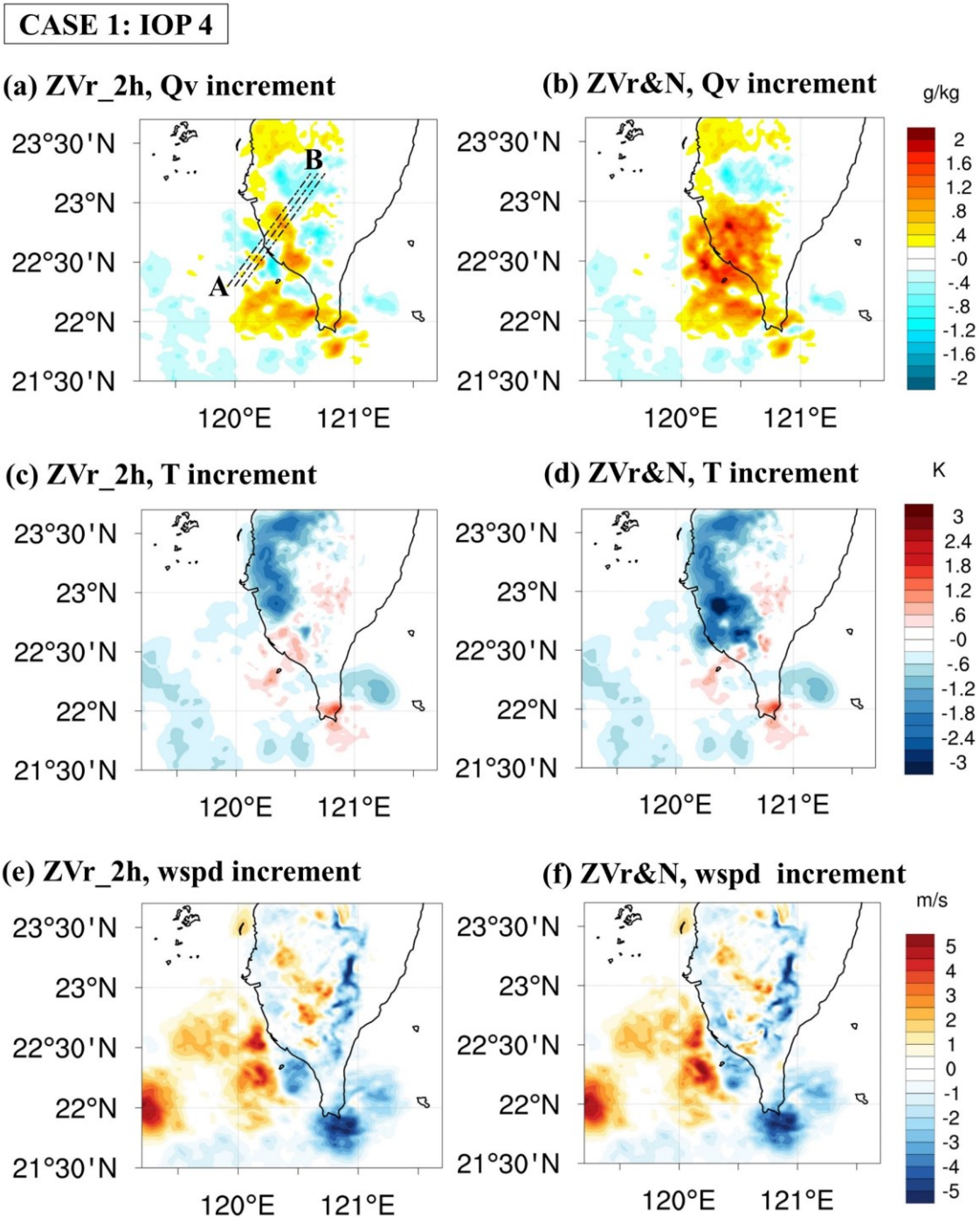


Figure 3.7: The analysis increments of Q_v (a–b), T (c–d), and wind speed (e–f) at the first cycle of the first case (i.e., 0400 UTC 02 June 2008) for experiments ZVr_2h (a,c,e) and $ZVr\&N$ (b,d,f). The figures were plotted at the second eta model level. The three black dash lines with characters A and B indicate the cross-sectional location for Fig. 3.9.

both inland and offshore (Fig. 3.7e). The assimilation of extra N information with Z and V_r (i.e., $ZV_r\&N$) almost increased the moisture inland and offshore of southwestern Taiwan (Fig. 3.7b). Moreover, in these regions, the temperature field was much colder by 1-3 K compared with ZV_r_2h (Fig. 3.7d). The additional N assimilation is also capable of modifying the wind field (Fig. 3.7f). To evaluate these corrections, the RMSEs of Q_v , T , and wind speed compared with the surface stations (red crosses in Fig. 3.3c) in the first cycle were calculated and listed in Table 3.2; the smallest RMSEs are indicated in bold font. Experiment $ZV_r\&N$ produced a greater reduction in RMSE of Q_v (around 1.2 g kg^{-1}), compared with ZV_r_2h . In addition, the corrections of temperature and wind field in $ZV_r\&N$ were better than those in ZV_r_2h with an improvement of RMSE of approximately 0.7 K and 0.4 m s^{-1} .

Table 3.2: RMSEs of the Q_v (g kg^{-1}), T (K), and wind speed (wspd; m s^{-1}) compared with surface stations at the first analysis cycle for the two cases. The smaller RMSEs in each case are indicated in bold font.

Experiments	Case 1: IOP 4			Case 2: IOP 8		
	Q_v	T	wspd	Q_v	T	wspd
ZV_r_2h	2.5	3.1	1.1	0.9	2.3	4.9
$ZV_r\&N$	1.3	2.4	0.7	0.3	1.9	4.7

The positive effect of assimilating additional N assimilation was further proved when examining the analysis column maximum Z (larger than 35 dBZ) at the first cycle (Fig. 3.8a,c,e). The results revealed that the strong convection line in the observation (denoted by the dash black box in Fig. 8a) was better captured in $ZV_r\&N$ than ZV_r_2h (Fig. 3.8e versus Fig. 3.8c). The location of strong convection corresponded well with the wetter and colder areas in $ZV_r\&N$. This means that the adjustment generated by assimilating additional N information was more precise than those by assimilating only Z and V_r . Three cross lines within this convection (denoted by three black dash lines with characters A and B in Fig. 3.7) were selected to examine the vertical distribution of the humidity, temperature, and wind field increments (Fig. 3.9). Compared with ZV_r_2h ,

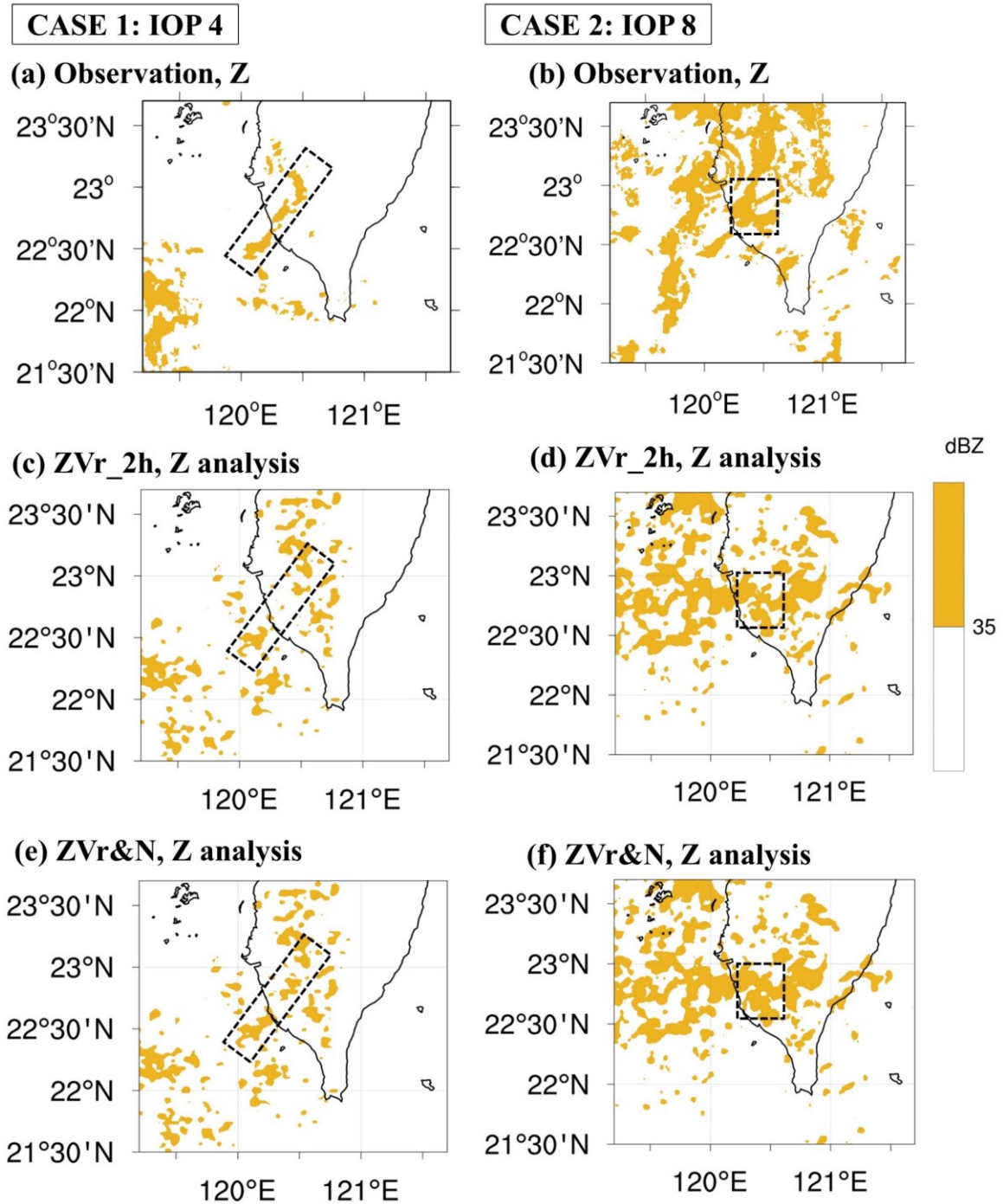
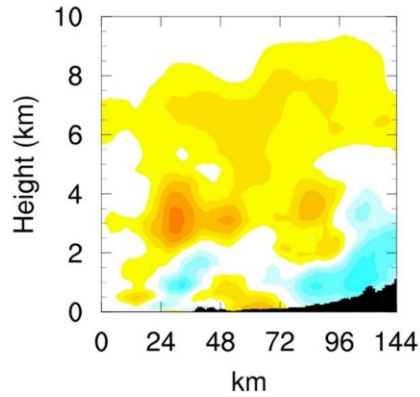


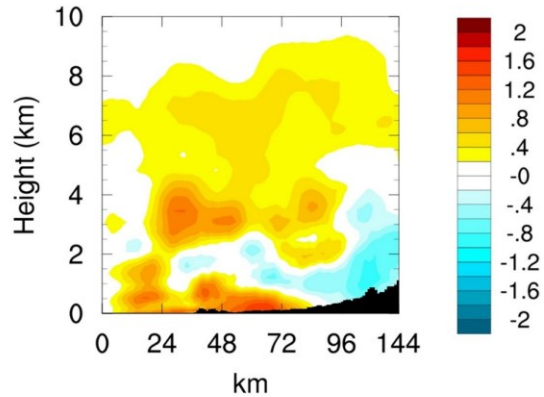
Figure 3. 8: The column maximum Z over 35 dBZ at the first cycle of the first case (i.e., 0400 UTC 02 June 2008; a,c,e) and the second case (i.e., 1000 UTC 14 June 2008; b,d,f). Observation (a–b), analysis of experiment ZVr_2h (c–d), analysis of experiment ZVr&N (e–f). The dash black boxes denote the more accurate Z analysis of ZV&N compared with ZVr_2h.

CASE 1: IOP 4

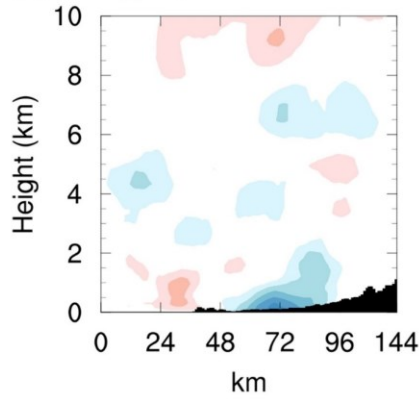
(a) ZVr_2h, Q_v increment



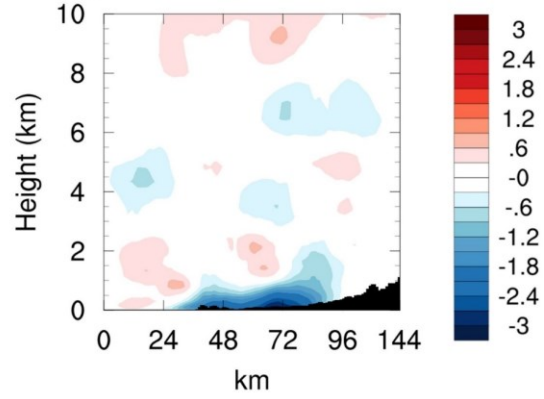
(b) ZVr&N, Q_v increment g/kg



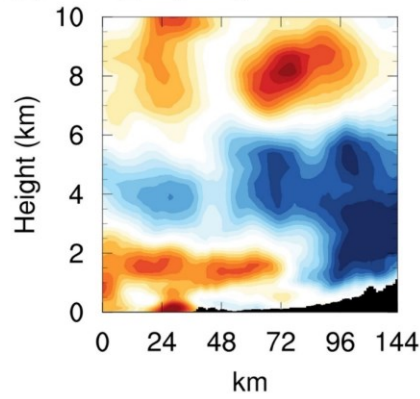
(c) ZVr_2h, T increment



(d) ZVr&N, T increment



(e) ZVr_2h, wspd increment



(f) ZVr&N, wspd increment

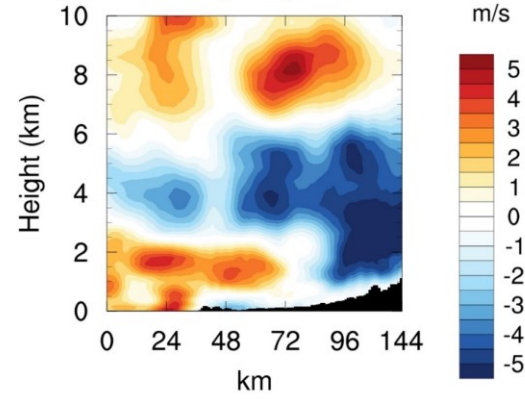


Figure 3. 9: Vertical cross-section of analysis increment of Q_v (a–b), T (c–d), and wind speed (e–f) at the first cycle of the first case (i.e., 0400 UTC 02 June 2008) along 3 lines with characters A and B (illustrated in Fig. 3.7) for experiments ZVr_2h (a,c,e) and ZVr&N (b,d,f).

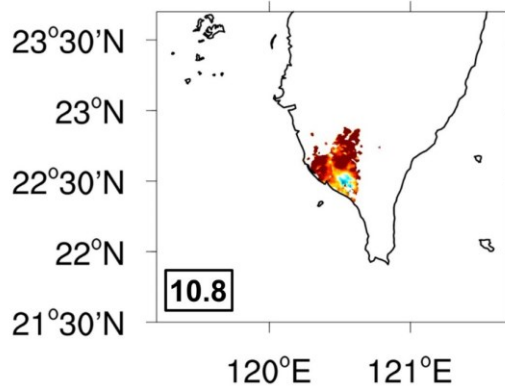
the wetter humidity, and colder temperature appeared at almost all levels below 4 km in ZVr&N with the most significant influence below 1 km. In terms of the wind field, the impact of assimilating additional N information also mainly occurred below 4 km with the stronger wind below 2 km.

To more comprehensively evaluate the correction generated by assimilating extra N information, the difference between the observation and analysis mean of the N at the first cycle is illustrated in Fig. 3.10a,b. Compared with the observation, the N analysis in experiments ZVr_2h was drier in both inland and coastal area (Fig. 3.10a). Conversely, in the experiments of assimilating N (i.e., ZVr&N), the N analysis was more enhanced and closer to the observation (Fig. 3.10b). The RMSEs of N (values in black boxes) indicated that experiment ZVr&N produced a greater reduction in RMSE of N (approximately 5 N-unit, around 1.2 g kg^{-1}) compared with ZVr_2h.

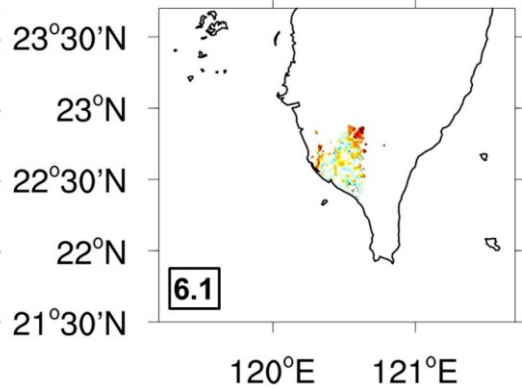
For a more detailed investigation of the assimilating additional N information along with Z and Vr, the Q_v analysis at the final cycle (i.e., 0600 UTC 02 June 2008) is described in Figs. 3.11a,b. Compared with assimilating only Z and Vr (Fig. 3.11a), assimilating additional N information for the entire 2 h produced higher moisture and greater southwesterly wind both on the land and offshore in southwestern Taiwan with the largest moisture localized near the mountain region (Fig. 3.11b). Figures 3.11c,d illustrate the convergence field at 1.5 km for the two experiments at the final cycle. The convergence occurred both over land and ocean to southwest Taiwan in both experiments, but the stronger convergence appeared near the mountain area in ZVr&N compared with ZVr_2h. Overall, the analysis results indicated that assimilating additional N information could better correct the moisture, temperature, and wind field and enhanced the convergence compared with only assimilating Z and Vr.

CASE 1: IOP 4

(a) ZVr_2h, O – A of N field

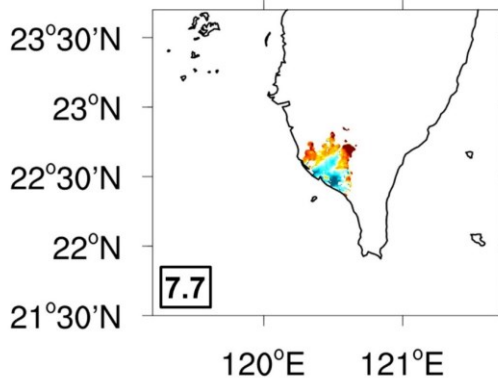


(b) ZVr&N, O – A of N field



CASE 2: IOP 8

(c) ZVr_2h, O – A of N field



(d) ZVr&N, O – A of N field

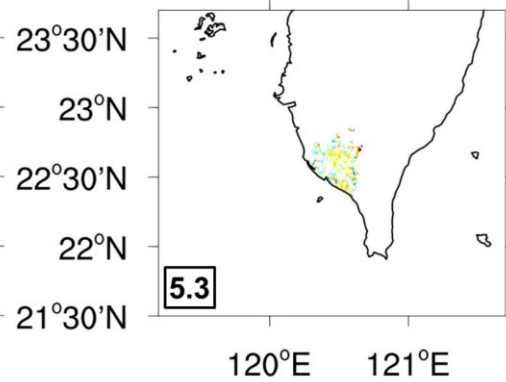


Figure 3. 10: The difference between the observation and analysis mean of the N at the second eta model level at the first cycle of the first case (i.e., 0400 UTC 02 June 2008; a–b) and the second case (i.e., 1000 UTC 14 June 2008; c–d) for experiments ZVr_2h (a,c) and ZVr&N (b,d). The numbers in the black boxes denote the RMSEs of N compared with the observation.

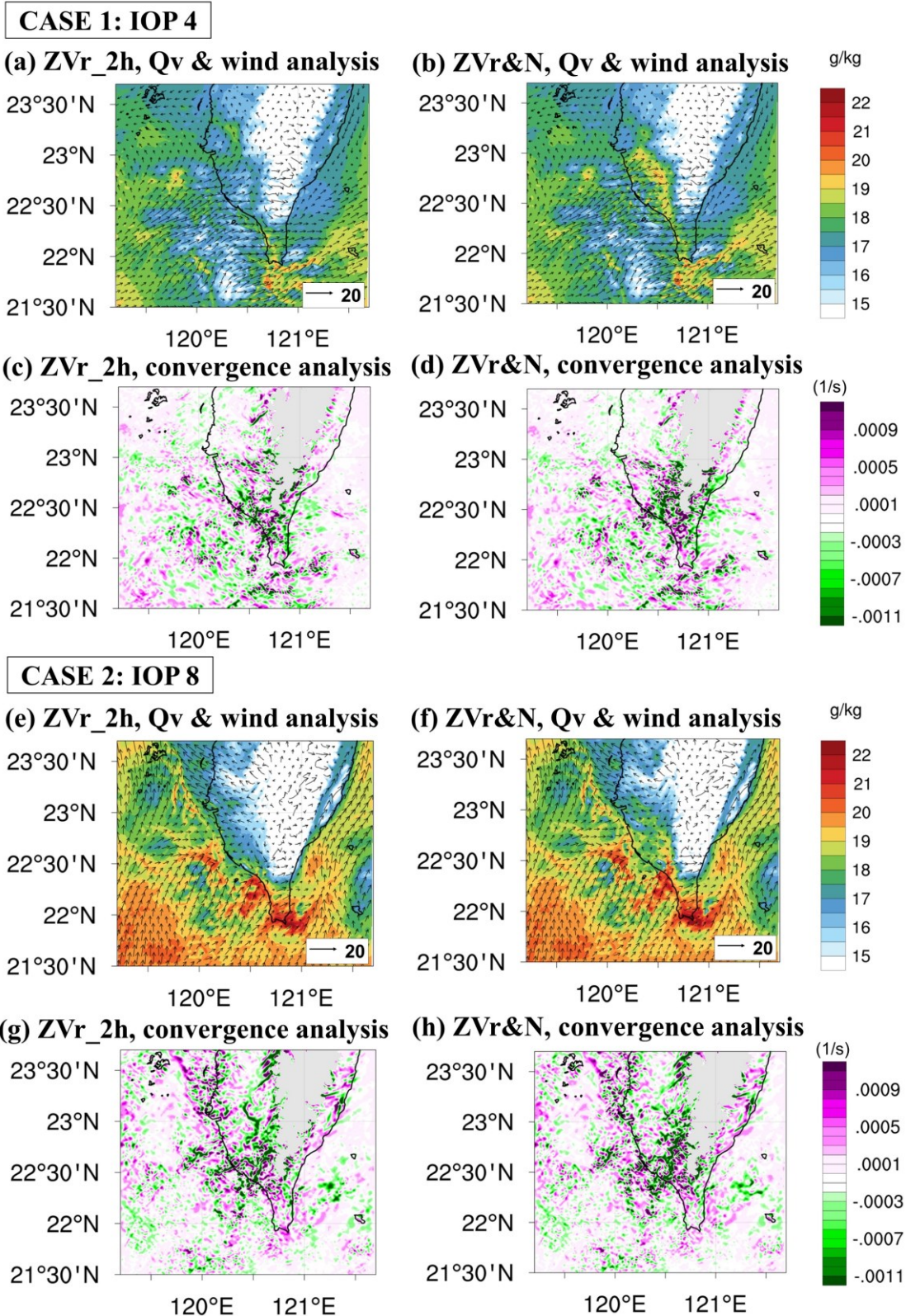


Figure 3. 11: The Q_v (g kg^{-1} , color shading) and wind (m s^{-1} , arrows) analysis (a,b,e,f) and convergence field at 1.5 km (c,d,g,h) at the final cycle of the first case (i.e., 0600 UTC 02 June 2008; a–d) and the second case (i.e., 1200 UTC 14 June 2008; e–h) for experiments ZVr_2h (a,c,e,g) and ZVr&N (b,d,f,h). The figures were plotted at the second eta model level.

b. Results of the forecast

Figures 3.12a–f depict the 3-h and 6-h accumulated rainfall of the first case (i.e., 02 June 2008). Compared with the 3-h accumulated rainfall observation (Fig. 3.12a), two experiments could produce heavy rain in the mountain but underestimated the heavy precipitated area on the west and south coast of Taiwan (Figs. 3.12b,c). For the intercomparison between the two experiments, ZVr_2h could not capture the rainfall larger than 40 mm in the mountainous region (Fig. 3.12b). In contrast, experiment ZVr&N could enhance and obtain the heavy rain in the mountain and eastern Taiwan with the heaviest rainfall over 40 mm (Fig. 3.12c). This may link to the better capturing main convection (Fig 3.8e), the enhancement of moisture, and the strengthening of wind convergence in ZVr&N compared with ZVr_2h (Fig. 3.11b versus Fig. 3.11a). For the 6-h lead time forecast, two experiments increased rainfall in eastern Taiwan, which had a similar trend to the observation (Figs. 3.12d–f). The closest forecast to the observation was ZVr&N, which captured well the heavy rain (Fig. 3.12f). Conversely, experiment ZVr_2h underestimated rainfall both in mountain areas and eastern Taiwan, leading to the worst short-term forecast (Fig. 3.12e).

The improvement achieved by assimilating additional N information is further proved in the quantitative evaluation. Figures 3.13a–d describe the FSSs of accumulated rainfall from 1 to 6 h of different thresholds for the first case. Overall, two experiments decreased FSSs as the rainfall thresholds increased. Because of the better performance in forecasting both light and heavy rain, experiment ZVr&N outperformed ZVr_2h during 6 h. Compared with assimilating only Z and Vr (i.e., ZVr_2h), the extra N information assimilation (i.e., ZVr&N) generated noteworthy enhancements in the QPF with three to four times higher FSS, especially for heavy rain. For further evaluation, the comparisons with rain gauges, S-Pol N, and sounding data were drawn in Figs. 3.14a,c,e,g. For the rainfall (Fig. 3.14a), the growth trend for RMSEs occurred as the lead time increased. Assimilating additional N information (ZVr&N) could reduce the rain RMSE during the period of 3- to 6-h forecast compared with assimilating Z and Vr alone (ZVr_2h). In the N evaluation (Fig. 3.14c), the lower RMSE was achieved in ZVr&N for most 6 h, except for the period from 1- to 2-h forecast. For the Qv sounding comparison, in 3 h (Fig. 3.14e), the better forecast was presented in experiment ZVr&N below 1.5 km. In the 6-h forecast (Fig. 3.14g), assimilating additional N information obtained lower Qv RMSE in comparison with ZVr_2h for most of the levels below 5 km.

The qualitative and quantitative evaluation indicated the forecast improvement obtained by assimilating additional N information than assimilating only Z and V_r .

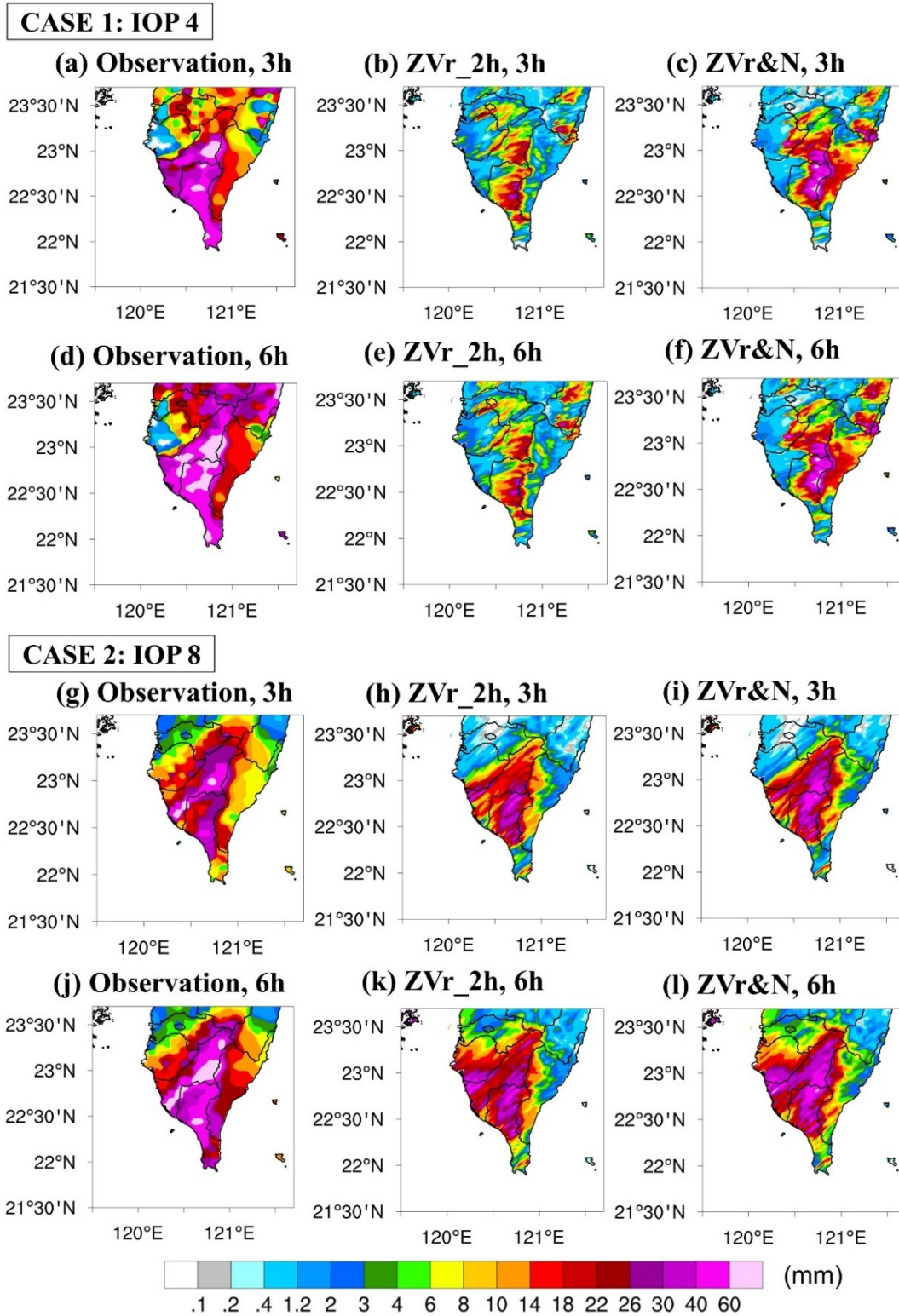
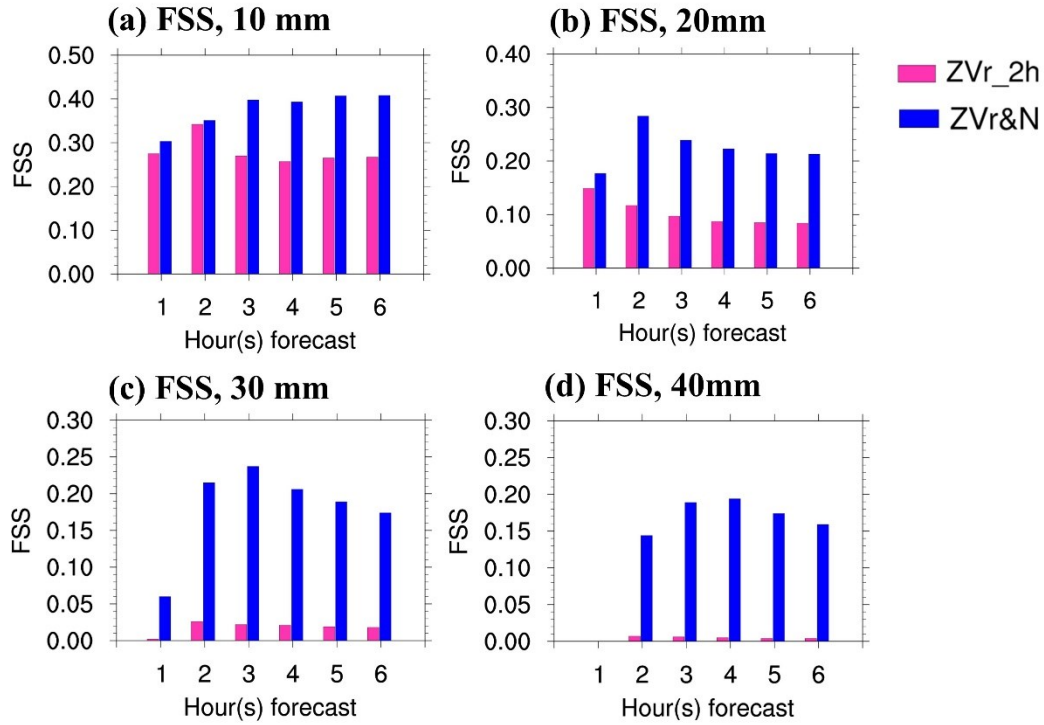


Figure 3.12: The 3 h (a–c; g–i) and 6 h (d–f; j–l) accumulated rainfall from 0600 UTC 02 June 2008 of the first case (a–f) and 1200 UTC 14 June 2008 of the second case (g–l). Observation (a,d,g,j); ZVr_2h (b,e,h,k); ZVr&N (c,f,i,l).

CASE 1: IOP 4



CASE 2: IOP 8

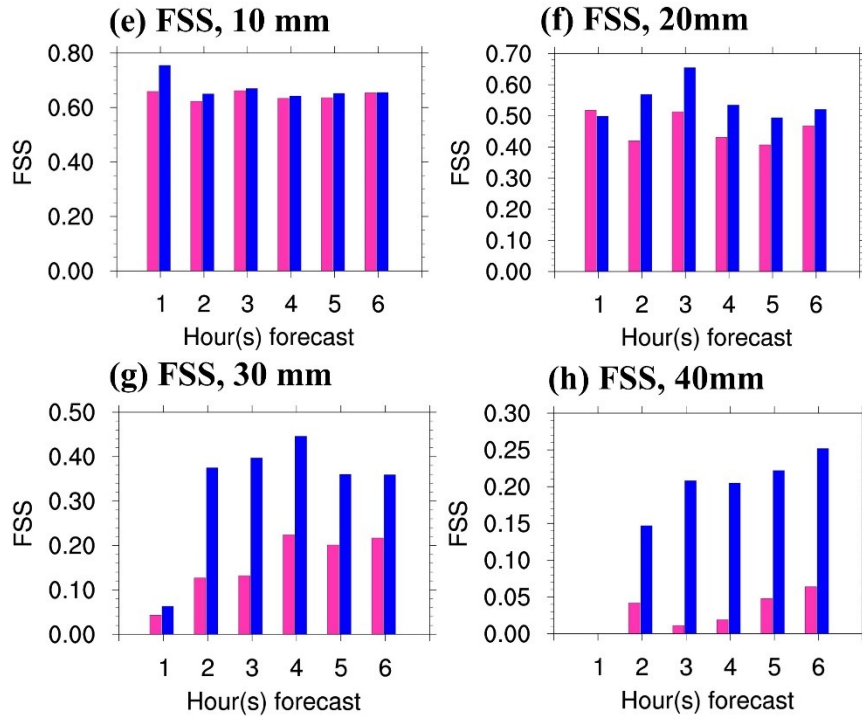


Figure 3.13: The FSS during 6-h accumulated rainfall of the first case (i.e., 02 June 2008; a–d) and the second case (i.e., 14 June 2008; e–h) for thresholds 10 mm (a,e), 20 mm (b,f), 30 mm (c,g), and 40 mm (d,h).

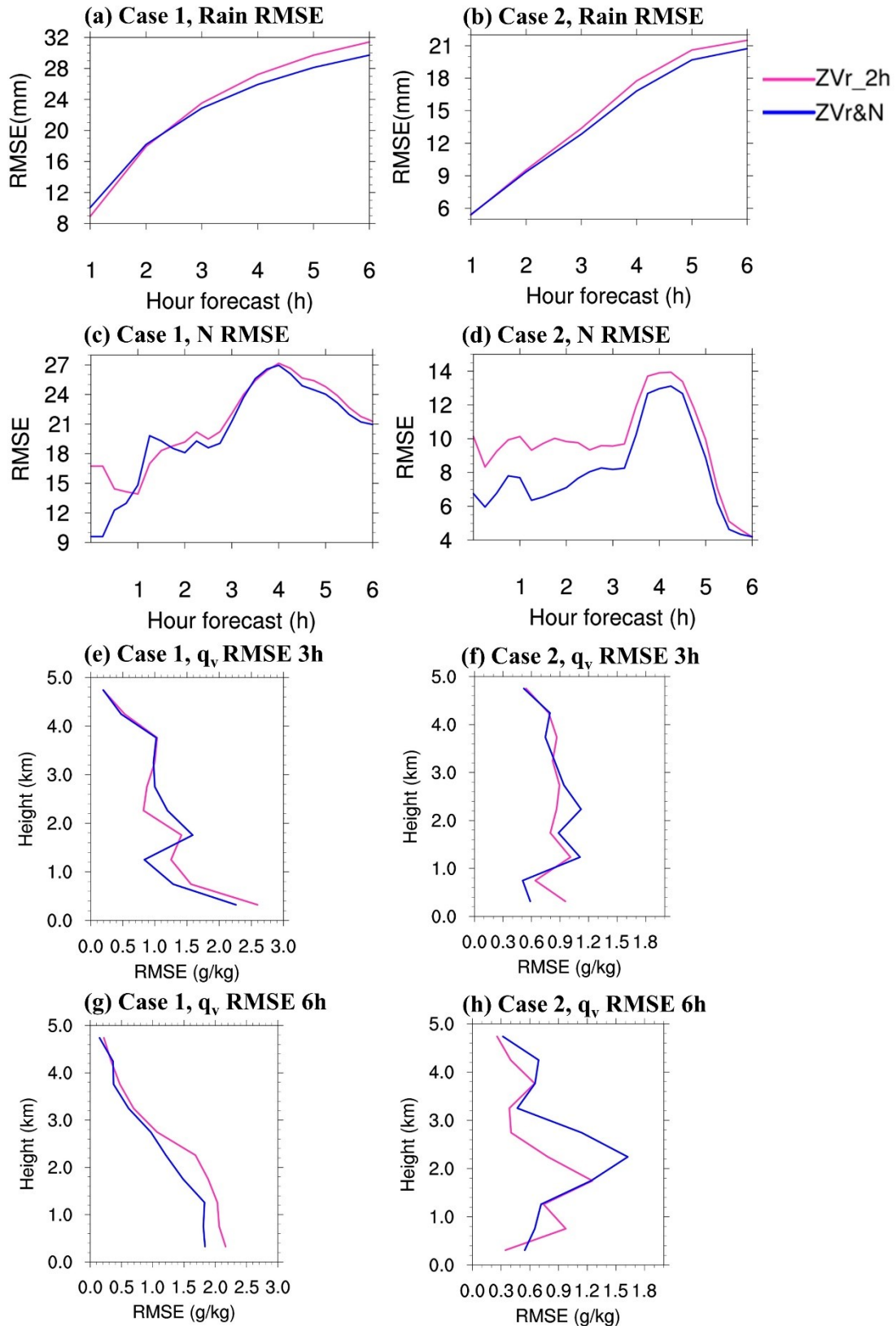


Figure 3.14: The RMSEs of rainfall (a,b), N (c,d) during 6-h forecast, and Q_v at 3- (e,f) and 6-h forecast (g,h) for the first case (i.e., 02 June 2008; a,c,e,g) and the second case (i.e., 14 June 2008; b,d,f,h).

3.4.2.2 Case 2: IOP 8

a. Results of the analysis

Similar to the first case, the ability to correct moisture, temperature, and wind field obtained by different assimilation experiments in the second case was investigated first (Fig. 3.15). Assimilating only Z and Vr in the first cycle (i.e., ZVr_2h) almost reduced moisture both over land and ocean. The positive increment locally appeared in some areas of the south coast, offshore, and mountain Taiwan (Fig. 3.15a). In experiment ZVr&N, assimilating additional N data could lessen the reduction of moisture inland and enhance the Q_v in the southwest offshore and mountain areas compared with assimilating only Z and Vr (Fig. 3.15b). For the temperature, the negative increment appeared almost over the domain in both experiments but the cooler field occurs in the southwest inland of ZVr&N (Fig. 3.15d versus Fig. 3.15c). With the same increment sign, the wind speed also decreased over the domain. However, assimilating additional N information could alleviate the reduction of wind speed in the southwest inland and coastal areas (Fig. 3.15e,f). The correction of moisture, temperature, and wind field by two experiments was evaluated based on the surface stations and detailed in Table 3.2. The lower RMSEs belonged to ZVr&N for all these three fields with the greatest reduction in RMSE of Q_v around 0.6 g kg^{-1} .

The benefit of assimilating additional N assimilation was further investigated by examining the analysis column maximum Z (larger than 35 dBZ) at the first cycle (Fig. 3.8b,d,f). The results revealed that the strong convection in the southwest inland (denoted by the dash black box in Fig. 3.8b) was better represented in ZVr&N (Fig. 3.8f) compared with ZVr_2h (Fig. 3.8d). The location of this convection was almost collocated with the areas that had wetter humidity, colder temperature, and stronger wind in Fig. 3.15b,d,f. In other words, assimilating extra N information was capable of better adjusting the moisture, temperature, and wind fields than assimilating only Z and Vr. The vertical distributions of the humidity, temperature, and wind field increment along three cross lines inside the strong convection (denoted by three black dash lines with characters C and D in Fig. 3.15a) were examined and illustrated in Fig. 3.16. Overall, assimilating additional N data could influence Q_v , T, and wind speed at all levels below 4 km, which was similar to the first case and reasonable with the vertical localization setting in this study. In particular, experiment ZVr&N lessened the negative and enhanced the positive of Q_v increment compared with ZVr_2h (Fig. 3.16a,b). The temperature was cooler over a broader range below 0.5 km in ZVr&N (Fig. 3.16c,d). Additionally, the increase in wind speed appeared near the surface and the levels from 0.5 to 2 km in the horizontal range of 0-24 km of ZVr&N (Fig. 3.16e,f).

CASE 1: IOP 8

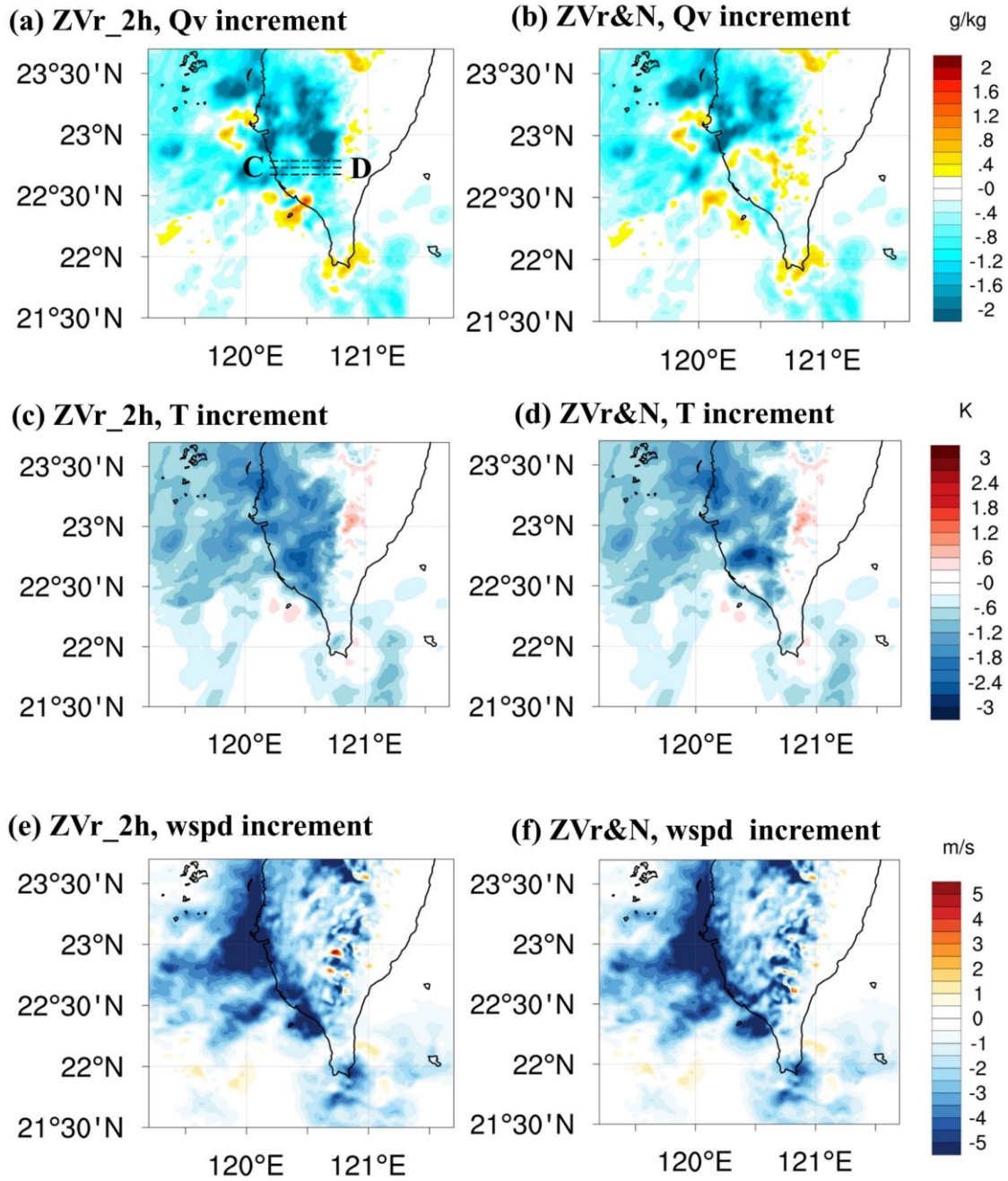
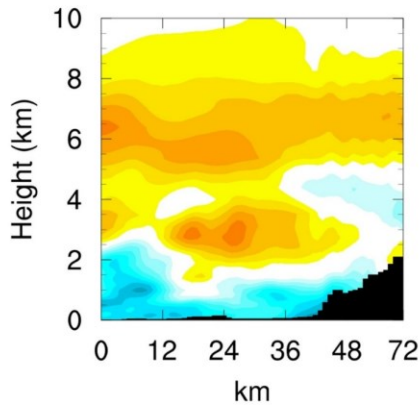


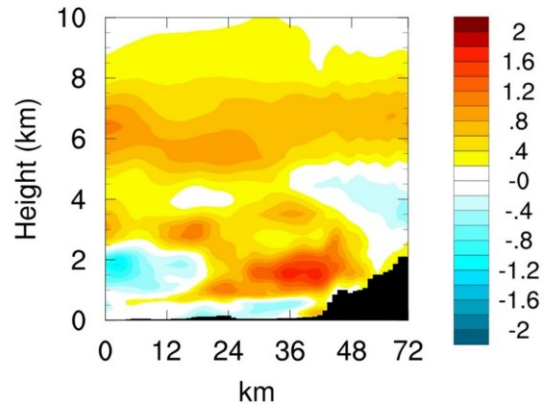
Figure 3.15: As in Fig. 3.7, but those for the second case (i.e., 1000 UTC 14 June 2008). The three black dash lines with characters C and D indicate the cross-sectional location for Fig. 3.16.

CASE 1: IOP 8

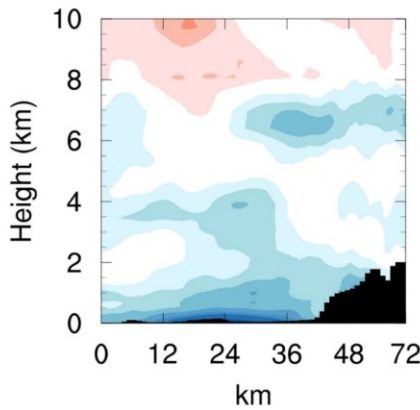
(a) ZVr_2h, Qv increment



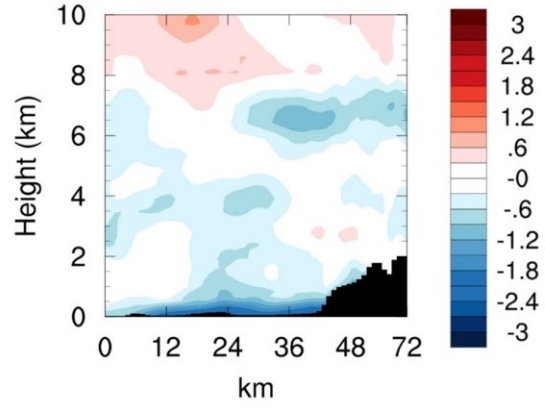
(b) ZVr&N, Qv increment g/kg



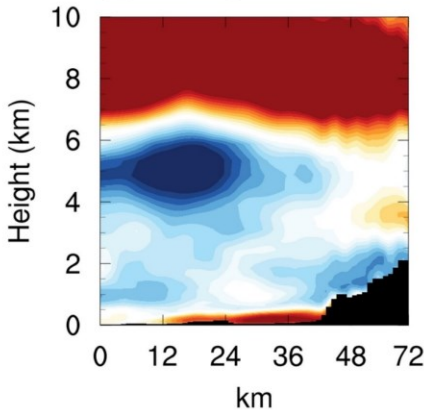
(c) ZVr_2h, T increment



(d) ZVr&N, T increment



(e) ZVr_2h, wspd increment



(f) ZVr&N, wspd increment

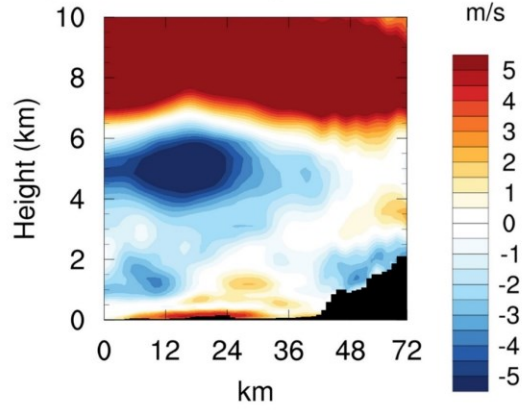


Figure 3. 16: As in Fig. 3.9, but those for the second case (i.e., 1000 UTC 14 June 2008) along 3 lines with characters C and D (illustrated in Fig. 3.15).

The difference between the observation and analysis mean of the N at the first cycle in the second case is depicted in Fig. 3.10c,d. Assimilating Z and Vr (i.e., ZVr_2h; Fig. 3.10c) overestimated N near the coastal area but underestimated N in land and near mountain regions compared with observation. Conversely, with the assimilation of N

information (i.e., ZVr&N; Figs. 3.10d), the moisture was drier near coastal and wetter over land and near mountain regions compared with ZVr_2h. Consequently, the N analysis in ZVr&N had more agreement with the observation. The RMSE of N (values in black boxes) in this experiment was reduced by more than 2 N-unit (0.4 g kg^{-1}) compared with that in ZVr_2h.

The Q_v analysis field of the second eta model level at the final cycle (i.e., 1200 UTC 14 June 2008) is detailed in Figs. 3.11e,f. The contribution of assimilating extra N information during nine cycles was presented in the Q_v enhancement in the land, near the southwest coast, and offshore. Figures 3.11g,h describe the convergence field of 1.5 km at the final cycle for the two experiments. The convergence was distributed over both land and ocean in ZVr_2h and ZVr&N. Compared with ZVr_2h, the more vigorous convergence occurred near the mountain in experiment ZVr&N. The analysis performance of the second case implied the positive impact of additional N assimilation on the moisture, temperature, and wind correction.

b. Results of the forecast

The 3- and 6-h accumulated rainfall of the second case (i.e., 14 June 2008) is drawn in Figs. 3.12g–l. For the 3-h forecast, compared with the observation, two experiments could forecast the heavy rain despite the underestimation of eastern Taiwan (Figs. 3.12h,i versus Fig. 3.12g). More agreement with observation appeared in experiment ZVr&N which significantly improves the amounts and locations of the precipitation by forecasting well the heavy rain in the mountain and coastal regions (Fig. 3.12i). This was the result inherited from the more precise moisture, temperature, and wind fields and stronger convergence analysis provided by ZVr&N in these areas. For the 6-h forecast, similar to the observation (Fig. 3.12j), two experiments tended to increase the rain over the southwest coastal and mountain areas (Figs. 3.12k,l). Compared with ZVr_2h, experiment ZVr&N better matched the observation in terms of the precipitation in the central mountain area and coastal of southwest Taiwan.

To provide a more thorough examination of the N assimilation impact, the FSSs of two experiments for various thresholds are detailed in Figs. 3.13e–h. As in the first case, the forecast performance became worse when increasing the rainfall thresholds. The results also indicated the beneficial impacts of additional N assimilation on the QPF. Compared with ZVr_2h, higher FSS was achieved for most of the thresholds in ZVr&N, with the most improvements recorded in heavy rain because of its more accurate rain forecast for the mountain and coastal areas. Additionally, the outperformance of this

experiment could prolong to 6 h. The further validation against other observations (i.e., rain gauges, S-Pol refractivity, and sounding data) was described in Figs. 3.13b,d,f,h. In terms of rainfall (Fig. 3.14b), with the extra N assimilation, ZVr&N generated more consistent forecasts to observation than ZVr_2h. For the N forecast (Fig. 3.13d), ZVr&N was more precise than ZVr_2h for the entire 6 h, the most improvement occurred in the first 3-h forecast. The Q_v sounding comparison reveals that ZVr&N produced the more accurate Q_v below 1 km in the 3-h forecast (Fig. 3.14f) but the forecast becomes worse in the 6 h compared with ZVr_2h (Fig. 3.14h).

3.4.2.3 Comparison of the two cases

In this study, two different cases were utilized to investigate the impact of N assimilation on the short-term forecast. The results revealed that assimilating additional N information generated the optimal correction for moisture, temperature, and wind fields and enhanced wind convergence, leading to the outperformance in QPF, especially for heavy rain. However, the level of the effect caused by N assimilation was different in the two cases. The impact of assimilating N in IOP 4 was more notably compared with IOP 8 for both light and heavy rain. This may link to the difference in the background moisture of the two cases. As mentioned in section 3.3.4, two different sets of initial and lateral boundary conditions were utilized to generate the dry-biased and wet-biased background moisture for IOP 4 and IOP 8, respectively. In the study of Gasperoni et al. (2013), the authors concluded that the more noteworthy advantage in N assimilation could be obtained in the dry-biased background moisture compared with the wet-biased background, which was consistent with the finding in our study. Furthermore, the background error correlations (BECRs) between N and Q_v both horizontal and vertical structures (Fig. 3.17) could be a reasonable explanation for the more significant effects of N assimilation in IOP4. The results showed that the BECRs between N and Q_v in IOP 4 had higher values and longer/deeper correlation lengths in the horizontal space/vertical structure than those in IOP 8. This pointed out that the N assimilation in IOP 4 could propagate the information to correct the moisture in broader ranges compared with IOP 8, resulting in the more noteworthy impacts when assimilating N in IOP 4. Additionally, as mentioned in section 3.2.2, IOP 4 had broader radar-retrieved N distribution than IOP 8, therefore, the moisture and wind correction occurred in wider ranges, which may lead to a more significant effect of N assimilation in IOP 4.

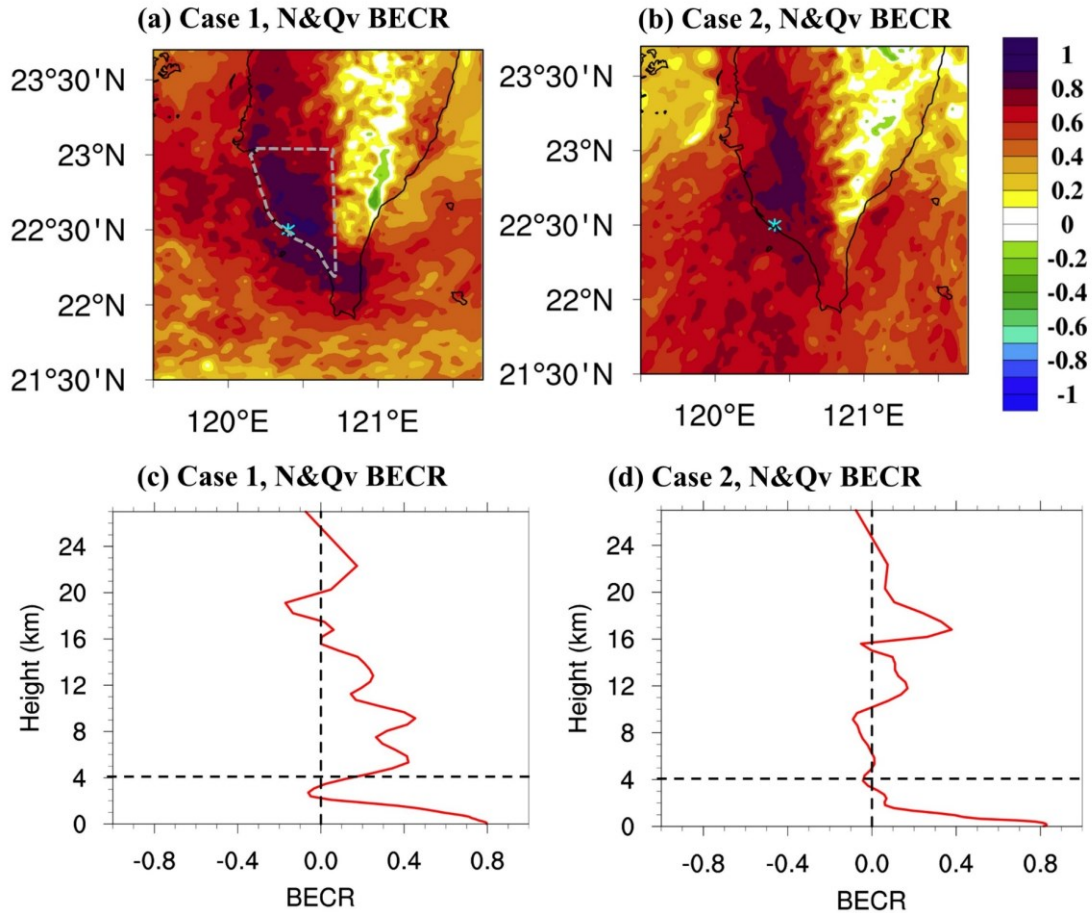


Figure 3.17: The second eta model level BECRs (a,b) and vertical BECRs (red curves; c,d) were estimated by the ensemble between N with Q_v for the first case (a,c) and the second case (b,d). The correlations are computed and averaged for all the reference points inside the area denoted by the gray dash line in (a) at the time of the first cycle before assimilating. The cyan stars stand for the S-Pol radar.

3.4.3 Results of the second experimental set

To study the impact of assimilating moisture information surrounding and inside the precipitation system, the second set of experiments was conducted for the 2-h assimilation periods (0300 to 0500 UTC and 0400 to 0600 UTC 02 June 2008). In each period, the analysis performance was examined first then the short-term forecast was assessed.

3.4.3.1 Assimilating refractivity before the precipitation system landed over the island (0300 UTC)

A comparison of the moisture and wind analysis at the final assimilation cycle (i.e., 0500 UTC) between N_ZVr and N_ZVrN was depicted in Figs. 3.18a,b. When only Z and Vr were assimilated in the second hour of the assimilation period (i.e., N_ZVr ; Fig. 3.18a), the high Q_v values were mainly located in the offshore and ocean. In contrast, the

additional N assimilation in the second hour in N_ZVrN enhanced the moisture inland and offshore in southwest Taiwan (Fig. 3.18b). Additionally, the southwest wind in these areas was strengthened compared with N_ZVr. Figures 3.18c,d present the 1.5-km convergence field at the final cycle in these two experiments. The results revealed that including the N information in the second hour of the assimilation period (i.e., N_ZVrN) could generate more vigorous convergences inland and near mountain areas to the southwest than without N assimilation (i.e., N_ZVr). The moisture analysis was evaluated by examining the N analysis (Figs. 3.19a,b). Compared with the observation (Fig. 3.4e), the N analysis in N_ZVr was underestimated and drier. On the contrary, the N analysis in N_ZVrN was wetter and closer to the observation. The RMSEs (values in black boxes) of N indicated that the moisture analysis in N_ZVrN was more accurate than that in N_ZVr with approximately 4 N-unit-reduction (e.g., 0.8 g kg^{-1}). Furthermore, the strong Z in southwestern near coastal areas (Fig. 3.4e; gray contours) was better captured in N_ZVrN compared with N_ZVr (Fig. 3.19b versus Fig. 3.19a; gray contours).

The 3- and 6-h accumulated rainfall from 0500 UTC is drawn in Figs. 3.20a–f. For the 3-h forecast, both experiments underestimated the rainfall near the south coast and a part of the north domain (Figs. 3.20b,c versus Fig. 3.20a). The more enhancement and precision in moisture analysis associated with the stronger wind convergence led to the well forecast of heavy rain for the mountain area in N_ZVrN (Fig. 3.20c). In contrast, N_ZVr (Fig. 3.20b) could not reach the heavy rain intensity in the mountain when verified against the observation. In the 6-h lead time forecast, both experiments (Figs. 3.20e,f) could catch the increasing trend of rainfall to the east domain as in the observation (Fig. 3.20d). The heavy rain in mountain regions was more accurately forecasted in N_ZVrN than in N_ZVr. The benefit of assimilating extra N in the second hour was more clear when investigating the FSS improvement rate (N_ZVrN compared with N_ZVr) for 3- and 6-h accumulated rainfall (Fig. 3.21, orange columns). The results pointed out that the improvement (positive values) appeared for most of the thresholds (except for 10 mm in the 3-h forecast). The most marked enhancement of N_ZVrN was obtained in the forecast of heavy rain larger than 40 mm (approximately 80 %).

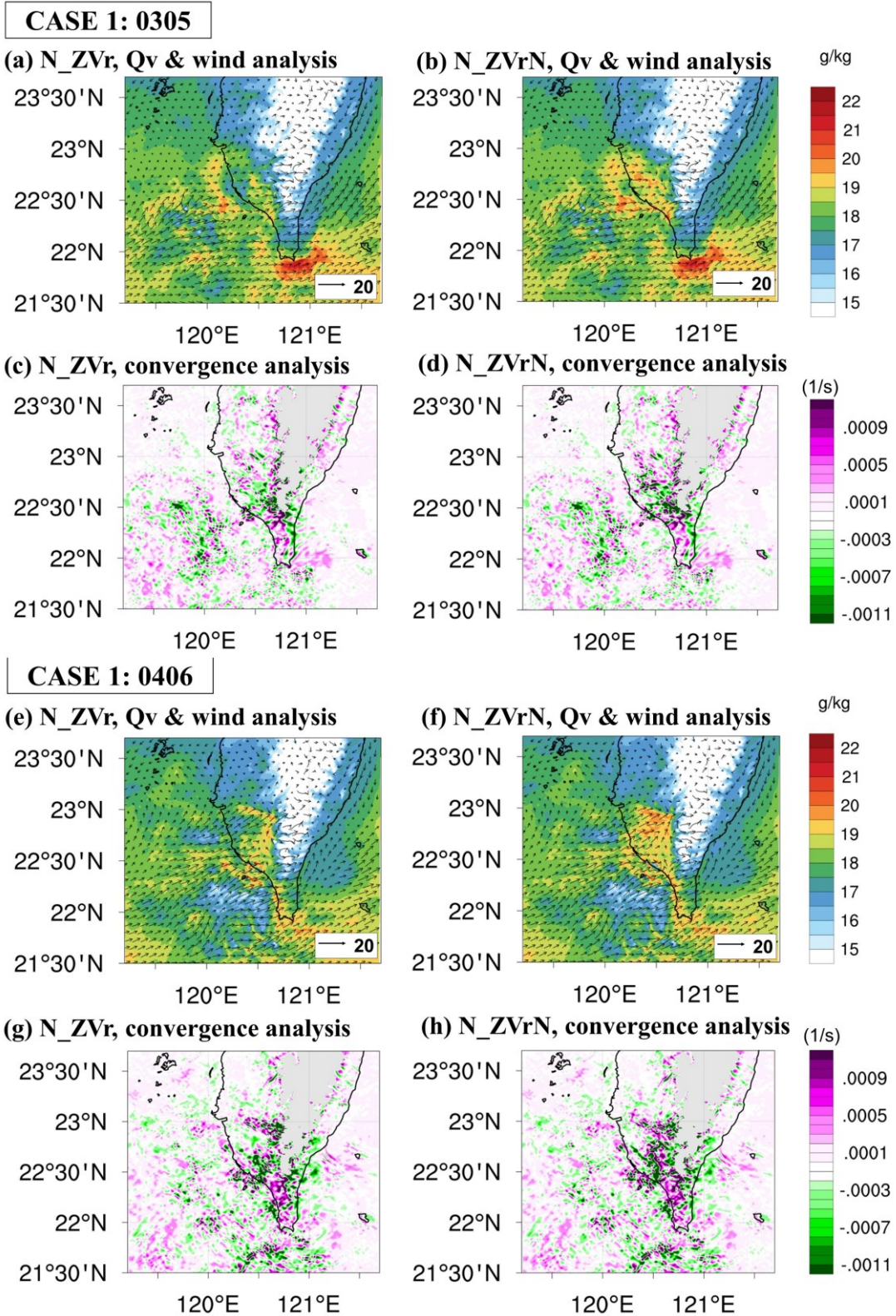
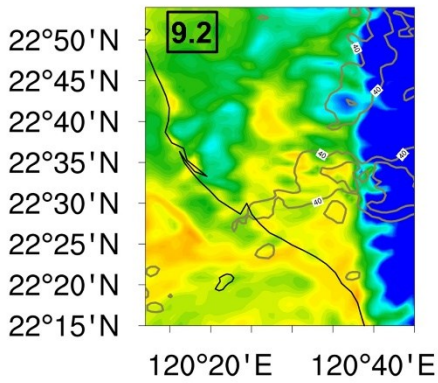


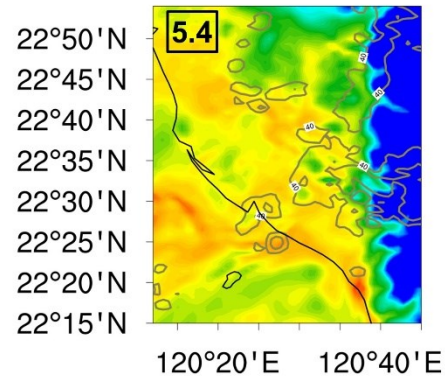
Figure 3. 18: As in Fig. 3.11, but those for the first case at 0500 UTC (a–d) and 0600 UTC (e–h) 02 June 2008 of experiments N_ZVr (a,c,e,g) and N_ZVrN (b,d,f,h).

CASE 1: 0305

(a) N_ZVr, N analysis

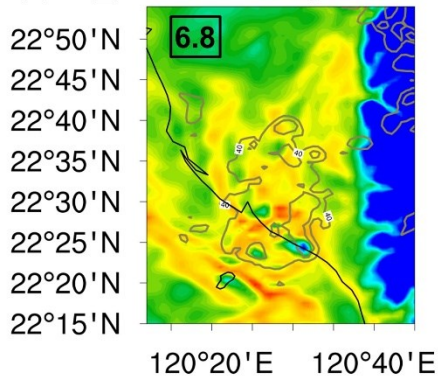


(b) N_ZVrN, N analysis



CASE 1: 0406

(c) N_ZVr, N analysis



(d) N_ZVrN, N analysis

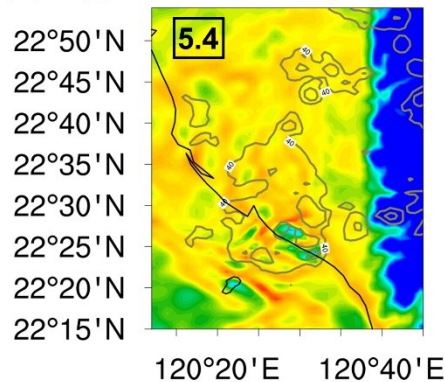
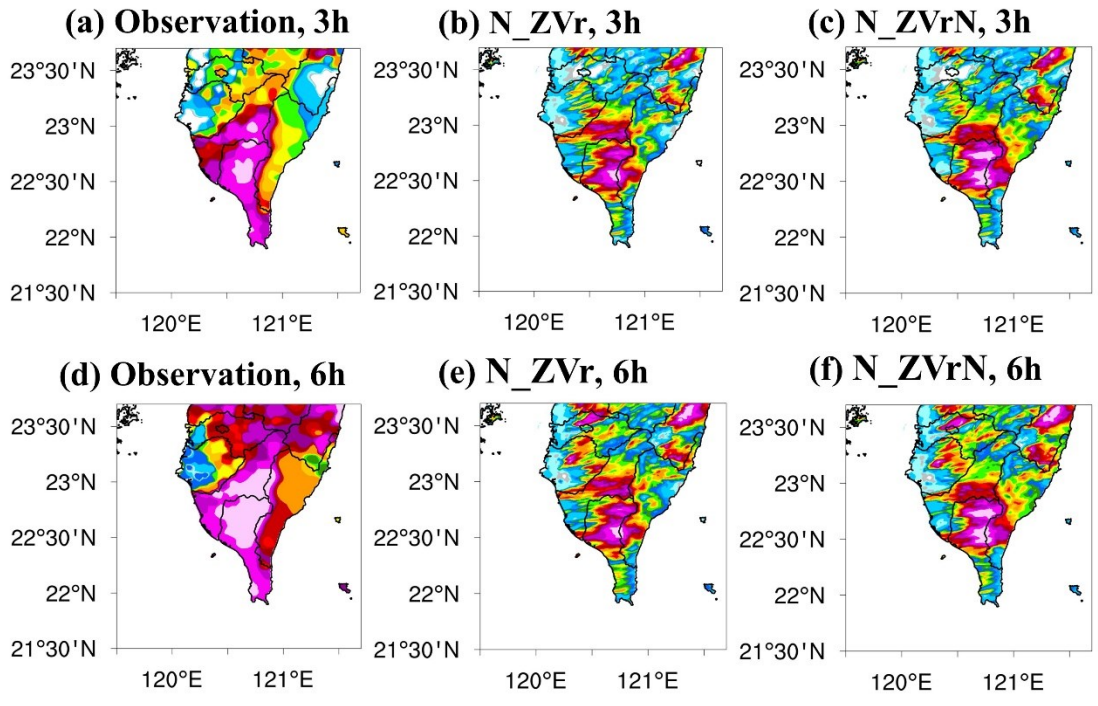


Figure 3. 19: The analysis of N of the first case at 0500 UTC (a,b) and 0600 UTC (c,d) 02 June 2008 for experiments N_ZVr (a,c) and N_ZVrN (b,d). The gray contours denote the maximum Z values larger than 40 dBZ. The numbers in the black boxes denote the RMSEs of N compared with the observation. The figures were plotted at the second eta model level.

CASE 1: 0305



CASE 1: 0406

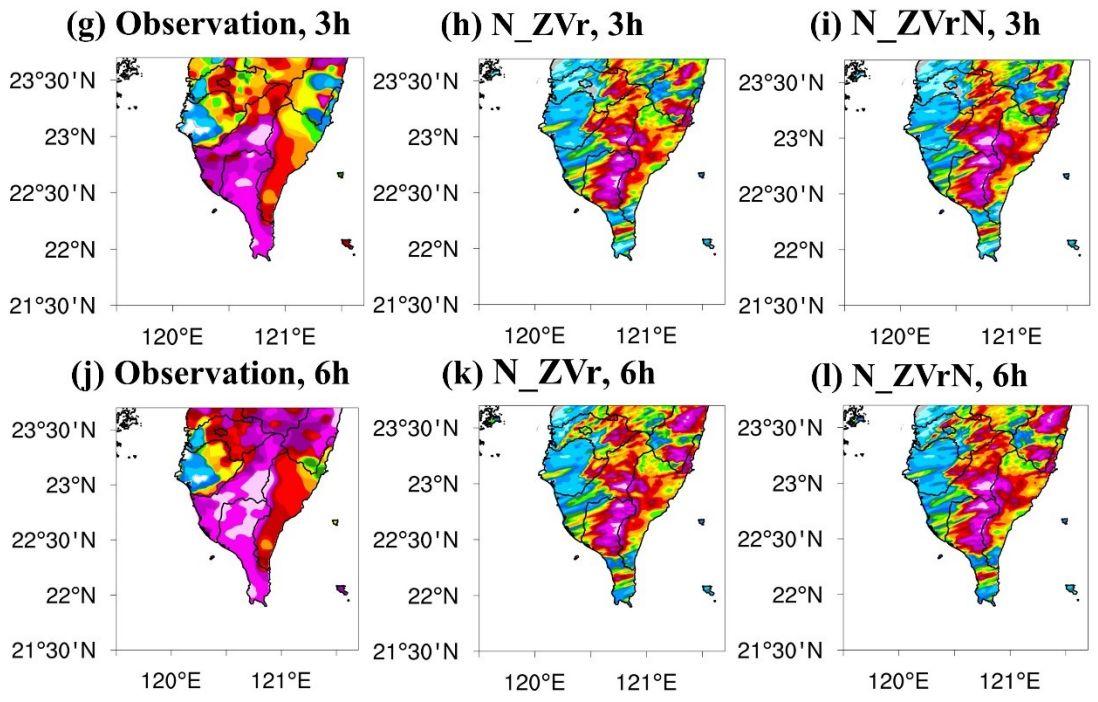


Figure 3. 20: As in Fig. 3.12, but those accumulated from 0500 UTC (a–f) and 0600 UTC (g–l) 02 June 2008 of the first case. Observation (a,d,g,j); N_ZVr (b,e,h,k); N_ZVrN (c,f,i,l).

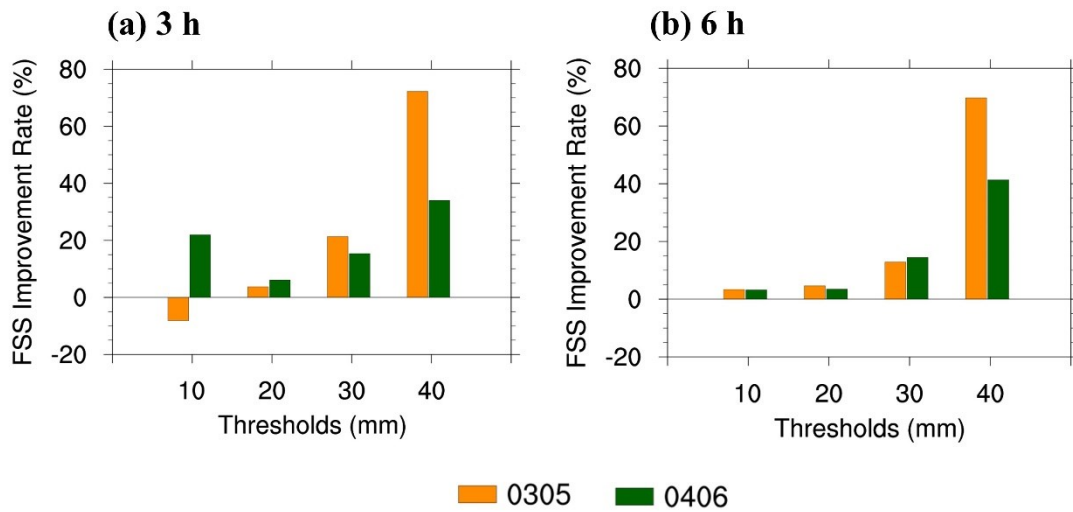


Figure 3. 21: The FSS improvement rate (%) for 3-h (a) and 6-h (b) accumulated rainfall from 0500 UTC (orange columns) and 0600 UTC (green columns) 02 June 2008 of the first case for thresholds 10 mm, 20 mm, 30 mm, and 40 mm.

3.4.3.2 Assimilating refractivity after the precipitation system landed over the island (0400 UTC)

The analyses of Q_v , wind, and convergence at the final cycle (0600 UTC) were illustrated in Figs. 3.18e–h. Compare with N_ZVr, the moisture analysis in N_ZVrN was much wetter inland and offshore in southwest Taiwan. Additionally, the wind near the mountain region in N_ZVrN was slightly strengthened (Fig. 3.18f versus Fig. 3.18e). The stronger convergence appeared in the inland and mountain areas in N_ZVrN than those in N_ZVr (Figs. 3.18g,h). For the N analysis at the final cycle, N_ZVr (Fig. 3.19c) presented drier N compared with the observation (Fig. 3.4g). By assimilating extra N information in the second hour, the N value increased inland and offshore in southwest Taiwan, resulting in a more agreement of N analysis with observation and an over 20% RMSE of N reduction compared with N_ZVr (Fig. 3.19d). Besides, N_ZVrN could better exhibit the strong convection near the mountain region (Fig. 3.4g; gray contours) than N_ZVr (Fig. 3.19d versus Fig. 3.19c; gray contours).

The accumulated rainfall in 3 and 6 h from 0600 UTC were depicted in Figs. 3.20g–l. In the 3-h forecast, because of the more accurate moisture and stronger convergence analysis, experiment N_ZVrN more precisely predicted the heavy rain in the mountain and eastern Taiwan compared with N_ZVr (Fig. 3.20i versus Fig. 3.20h). For the 6-h forecast, two experiments got increasing the rainfall to the east domain which was

consistent with the observed trend. The impact of additional N assimilation could prolong until 6-h, which was evident in the better agreement with observation in terms of heavy rain in N_ZVrN than those in N_ZVr (Figs. 3.20l and k). The outperformance of N_ZVrN was further proved when examining its FSS improvement rate compared with N_ZVr (Fig. 3.21, green columns). The results revealed that with the extra N assimilation in the second hour, the QPF in N_ZVrN was better than N_ZVr . The positive values of the FSS improvement rate occurred in all thresholds of the 3- to 6-h forecast.

The results of the analysis and short-term forecast in two different periods concluded that continuing the assimilation of N field after the precipitation system landed over the island generated more precise moisture and more vigorous convergence analyses, brought more benefit for the rain forecast compared with only assimilating Z and Vr . For the comparison between the two periods of assimilation, the RMSE improvement rate of N field (N_ZVrN versus N_ZVr) from the sixth to ninth analysis cycle was calculated and listed in Table 3.3; the higher improvement is indicated in bold font. The results reveal that assimilating N information earlier was capable to optimize the humidity modification (higher positive values) throughout the final three analysis cycles. This may lead to the more notable benefit of heavy rain forecast when the N assimilation started at 0300 UTC (before the precipitation system landed) than at 0400 UTC (after landing) as shown in Fig. 3.21 (orange columns versus green columns).

Table 3.3: The RMSE improvement rate (%) of the N (N_ZVrN versus N_ZVr) from the sixth to ninth analysis cycle for the two assimilation periods. The higher improvement in each assimilation period is indicated in bold font.

Assimilation period (UTC)	6 th cycle	7 th cycle	8 th cycle	9 th cycle
0300-0500	10.3	33.2	27.9	41.3
0400-0600	13.9	23.6	26.0	20.5

3.5 Summary and conclusions

The N data provides the moisture information near the surface which is critical for the heavy rain forecast. In this study, the impact of assimilating additional N information on the heavy rain forecast in the tropical region was evaluated. Additionally, the N assimilation before and after the weather system landed was investigated. Two heavy rain events from the SoWMEX (i.e., IOP 4 and IOP 8) were examined with two different sets of experiments in the LETKF system. For evaluating the role of additional N information, a comparison with assimilation of Z and Vr (ZVr_2h and $ZVr\&N$) was made. Because of the convection features, the second experimental group was conducted only in IOP 4 to study the N assimilation before and after convection approach the land. Two experiments (N_ZVr and N_ZVrN) were conducted with different starting assimilation times (beforehand and afterward the landing of the weather system at 0300 and 0400 UTC, respectively). All experiments performed 2-h assimilation with 15-min interval and 6-h deterministic forecast. Our major findings are summarized as follows:

- (1) The results of two cases in the first experimental group revealed that assimilating Z and Vr for the 2-h period could trigger the location of strong convergence but underestimated the moisture field. Therefore, experiment ZVr_2h captured well the rain pattern but underpredicted the heavy rain. In contrast, assimilating additional N data along with Z and Vr (i.e., $ZVr\&N$) generated the optimal corrections of moisture, temperature, and wind field and more enhancement in the convergence compared with assimilating only Z and Vr (i.e., ZVr_2h). Consequently, a better QPF was obtained in $ZVr\&N$ for both light and heavy rain. The higher FSSs occurred in $ZVr\&N$ during the 6-h forecast compared with ZVr_2h . The results also indicated that the first case (IOP 4) with dry-biased background moisture and broader N distribution gave more significant effects of assimilating N compared with IOP 8.
- (2) The results from the second experimental set implied that keeping assimilating extra N after the convection moving inland could enhance the convergence and more accurately present the moisture during the analysis, resulting in the better QPF compared with assimilating Z and Vr alone. In addition, the comparison between the two periods of assimilation suggested that starting N assimilation before the precipitation system landed (0300 UTC) generated more marked

improvements for the forecast of heavy rain than after it approached the land (0400 UTC). This result could be because of the better moisture adjustment obtained by the earlier N assimilation.

Overall, this study emphasized the positive impact of assimilating additional N information on the QPF. Moreover, our research also indicated that the effect of N assimilation is more notable in the case with dry-biased background moisture and broader N distribution. Therefore, more study cases with different kinds of synoptic systems and in various environments such as thunderstorms and typhoons should be investigated to examine the role of N information assimilation.

Chapter 4 Conclusions and Future Work

4.1 General conclusions

In the previous studies, researchers focus on utilizing radar data to adjust the state variables inside the precipitation system. This thesis further extended to assimilate the humidity information via the retrieved algorithm of scanning radar data. For the first time, the dual-wavelength-retrieved water vapor from S-Pol and Ka-band radar was assimilated and evaluated. Additionally, the approach of how to thin and assimilate this information was also figured out. Moreover, the assimilation of radar-retrieved N information was revisited in the dissertation but initially applied in the tropical region with the high-resolution assimilation system through the two real cases. On the other hand, based on the availability of N data, for the first time, the N assimilation before and after the landing of the weather system was investigated. The study also found a way to obtain the optimal QPF when applying N assimilation. The main conclusions are summarized below.

In Chapter 2 of this thesis, the S-PolKa-retrieved water vapor which stands for the environmental moisture information nearby the precipitation system was thinned into one averaged and four-quadrants Q_v profiles and then assimilated by two strategies relying on the characteristic of this retrieved information. The retrieved Q_v was assimilated along with Z and V_r for the entire assimilation period in the first strategy. The second strategy applied assimilating Q_v alone in the first hour and Z and V_r in the second hour of the assimilation period. Six experiments were conducted through the WLRAS in three real cases including two heaviest rain events and one scattered convection event in the DYNAMO campaign. The conclusions are as follows:

- The environmental moisture nearby the precipitation system was effectively adjusted by assimilating additional Q_v in both strategies. The optimal moisture correction occurred when the retrieved Q_v was assimilated alone in the first hour of the assimilation period. This strategy also generated more precise analysis fields compared with other experiments in regard to the observation.
- The positive effect of assimilating additionally S-PolKa-retrieved water vapor was illustrated in the qualitative and quantitative evaluation of the short-term

forecast. The verification showed that the QPF was improved and higher FSS was obtained by assimilating extra Q_v . In the strategy that only Q_v was assimilated in the first hour of the assimilation period, the rain intensity and pattern were better forecasted and the highest FSS were achieved. Moreover, the comparison with other observations comprised of surface, sounding, and S-PolKa-retrieved Q_v data also proved the improvement of wind, temperature, and humidity forecast by assimilating additionally retrieved Q_v .

- For the thinning method of S-PolKa-retrieved Q_v , the research pointed out that assimilating four-quadrant Q_v profiles provide more precise analysis and resulted in more noteworthy QPF improvement compared with the one averaged Q_v profile assimilation. This may link to the greater variety of moisture information given by the four-quadrant Q_v profiles.

Apart from the S-PolKa-retrieved water vapor, the assimilation of radar-retrieved N which represented the moisture information near the surface was also examined in our thesis (Chapter 3). By employing the WLRAS system and two heavy rain events from the SoWMEX (IOP 4 and IOP 8), two different experimental groups were conducted. The experiment results and related conclusions are summarized as follows:

- In the first experimental group of two cases, the assimilation of additional N exhibited the optimal corrections of moisture, temperature, and wind fields and obtained stronger convergence compared with assimilating Z and V_r alone. Consequently, both light and heavy rain were better forecasted with higher FSS during 6-h by assimilating N along with Z and V_r . The study also concluded that the more marked effect of N assimilation occurred in the case with dry-biased background moisture and broader N distribution.
- Relying on the characteristic of N , the second set of experiments was conducted in the IOP 4 to examine the N assimilation beforehand and afterward the landing of the convection system. The results pointed out that with the remaining additional N assimilation after the precipitation landed, a better QPF could be obtained compared with assimilating only Z and V_r in this period. On the other hand, the research suggested assimilating N assimilation before the weather system landed to achieve the optimal short-term forecast.

Overall, this dissertation proved the necessity of assimilating additional moisture information to improve the short-term forecast at convective scales.

4.2 Future Works

In this dissertation, the benefit of assimilating additional information from two radar-retrieved moisture sources on the QPF was proved. However, each kind of retrieved data has its limitation. For the S-PolKa-retrieved water vapor, the data is only available before the precipitation system approaches the radar location and distributes quite narrowly (within 25 km from the radar center). On the other hand, the effect of radar-retrieved N assimilation may be affected by the limited spatial distribution which depends on the stationary-point-like target at the ground. Besides, the N data only carries the moisture information near the surface. Taking into account the critical role of humidity in convection analysis and forecast, the assimilation of different moisture sources is worth further investigation.

Moisture information from micro-pulse differential absorption lidar (MicroPulse DIAL, MPD)

MPD has been developed by the collaboration of NCAR and Montana State University since 2011. Two separate laser wavelengths are utilized in the DIAL technique consisting of an absorbing wavelength and a non-absorbing wavelength. The amount of water vapor in the atmosphere is estimated based on the ratio of range-resolved backscattered signals between the two wavelengths. MPDs can provide the water vapor information in the lower troposphere at 150 m resolution and 1-5 min time intervals. The vertical range is from 300 m to 4 km above ground level in the daytime with broader ranges (up to 6 km) at night. During the Taiwan-Area Heavy rain Observation and Prediction Experiment (TAHOPE) 2022, three MPDs were deployed. The moisture data from these MPDs can be combined with the refractivity obtained from the S-Pol radar which was also employed during the TAHOPE to fully construct the moisture structures. Assimilating this completed data set can be further examined.

Moisture and temperature information from the ground-based microwave radiometer (MWR)

The MWR can provide the temperature and humidity profiles with a high temporal resolution (every 1 min) in the troposphere under all weather conditions. This kind of continuous and real-time accurate atmosphere observation can make up for the atmosphere information shortage and satisfy the requirement of the high-resolution NWP system. However, the assimilation of moisture and temperature obtained from MWR into the NWP is still in its early stage and needs further investigation, particularly in Taiwan.

During the TAHOPE 2022, one MWR was employed near the S-Pol radar location in Hsin-Chu. The impact of assimilating temperature and water vapor from MWR on the QPF can be examined by assimilating these data either alone or along with other moisture information such as radar-derived refractivity and water vapor from MPD.

The water vapor-related information from Himawari-8

Himawari-8 satellite was successfully launched in October 2014 by the Meteorological Satellite Center of Japan Meteorological Agency and started operation in July 2015. This satellite is located at the equator and 140.7°E with the observed range of 80°E to 160°W and 60°N and 60°S. The Advanced Himawari Imager (AHI) instrument on board Himawari-8 provides information very 10 min for the full dis of the globe and 2.5 min for the selected region with 0.5–2 km spatial resolution. AHI comprises multispectral imagers with 16 spectral bands in visible, near-infrared, and thermal infrared spectra. The high spatial-temporal resolution of Himawari-8 satellite data has been widely used in the meteorology and radiation field showing potential in weather forecast and disaster prevention. AHI has the capability to detect the humidity with three water vapor channels (6.2, 6.9, and 7.3 μm). These three bands are sensitive to the moisture in the middle and upper troposphere and can affect the lower troposphere. The assimilation of water vapor-related information obtained from the Himawari-8 satellite has not yet been comprehensively investigated in Taiwan. In the future, more research on assimilating alone moisture data from Himawari-8 or combining this information with radar data deserves further investigation.

Other further studies

In this thesis, the moisture information was assimilated along with Z and Vr only. In the future, the assimilation of water vapor information along with other radar data besides Z and Vr deserves to be comprehensively examined. On the other hand, prediciting the convection initialization (CI) is a very challenging issue, and Z and Vr data are limitedly observed before the development of the convection. The N field can be obtained both before and after the growth of the weather system. Therefore, the assimilation of N can be further investigated to study the convection initialization.

Bibliography

- Aksoy, A., D. C. Dowell, and C. Snyder, 2009: A multicas e comparative assessment of the ensemble Kalman filter for assimilation of radar observations. Part I: Storm-scale analyses. *Mon. Weather Rev.*, **137**, 1805–1824, <https://doi.org/10.1175/2008MWR2691.1>.
- Alpert, J. C., and V. K. Kumar, 2007: Radial wind super-obs from the WSR-88D radars in the NCEP operational assimilation system. *Mon. Weather Rev.*, **135**, 1090–1109, <https://doi.org/10.1175/MWR3324.1>.
- Anderson, J. L., 2001: An ensemble adjustment Kalman filter for data assimilation. *Mon. Weather Rev.*, **129**, 2884–2903, [https://doi.org/10.1175/1520-0493\(2001\)129<2884:AEAKFF>2.0.CO;2](https://doi.org/10.1175/1520-0493(2001)129<2884:AEAKFF>2.0.CO;2).
- Barker, D. M., W. Huang, Y. R. Guo, A. J. Bourgeois, and Q. N. Xiao, 2004: A three-dimensional variational data assimilation system for MM5: Implementation and initial results. *Mon. Weather Rev.*, **132**, 897–914, [https://doi.org/10.1175/1520-0493\(2004\)132<0897:ATVDAS>2.0.CO;2](https://doi.org/10.1175/1520-0493(2004)132<0897:ATVDAS>2.0.CO;2).
- Brotzge, J. A., and Coauthors, 2020: A technical overview of the New York state mesonet standard network. *J. Atmos. Ocean. Technol.*, **37**, 1827–1845, <https://doi.org/10.1175/JTECH-D-19-0220.1>.
- Caumont, O., V. Ducrocq, É. Wattrelot, G. Èv. Jaubert, and S. Pradier-Vabre, 2010: 1D+3DVar assimilation of radar reflectivity data: A proof of concept. *Tellus, Ser. A Dyn. Meteorol. Oceanogr.*, **62**, 173–187, <https://doi.org/10.1111/j.1600-0870.2009.00430.x>.
- Caya, A., J. Sun, and C. Snyder, 2005: A Comparison between the 4DVAR and the Ensemble Kalman Filter Techniques for. *Mon. Weather Rev.*, **133**, 3081–3094, <https://doi.org/https://doi.org/10.1175/MWR3021.1>.
- Chang, S. F., J. Sun, Y. C. Liou, S. L. Tai, and C. Y. Yang, 2014: The influence of erroneous background, beam-blocking and microphysical non-linearity on the application of a four-dimensional variational Doppler radar data assimilation system for quantitative precipitation forecasts. *Meteorol. Appl.*, **21**, 444–458, <https://doi.org/10.1002/met.1439>.

- , Y. C. Liou, J. Sun, and S. L. Tai, 2016: The implementation of the ice-phase microphysical process into a four-dimensional Variational Doppler Radar Analysis System (VDRAS) and its impact on parameter retrieval and quantitative precipitation nowcasting. *J. Atmos. Sci.*, **73**, 1015–1038, <https://doi.org/10.1175/JAS-D-15-0184.1>.
- Cheng, H. W., S. C. Yang, Y. C. Liou, and C. Sen Chen, 2020: An investigation of the sensitivity of predicting a severe rainfall event in northern Taiwan to the upstream condition with a WRF-based radar data assimilation system. *Sci. Online Lett. Atmos.*, **16**, 97–103, <https://doi.org/10.2151/SOLA.2020-017>.
- Chung, K. S., I. Zawadzki, M. K. Yau, and L. Fillion, 2009: Short-term forecasting of a midlatitude convective storm by the assimilation of single-doppler radar observations. *Mon. Weather Rev.*, **137**, 4115–4135, <https://doi.org/10.1175/2009MWR2731.1>.
- , W. Chang, L. Fillion, and M. Tanguay, 2013: Examination of situation-dependent background error covariances at the convective scale in the context of the ensemble Kalman filter. *Mon. Weather Rev.*, **141**, 3369–3387, <https://doi.org/10.1175/MWR-D-12-00353.1>.
- Crook, N. A., 1996: Sensitivity of moist convection forced by boundary layer processes to low-level thermodynamic field. *Mon. Wea. Rev.*, **124**, 1767–1785.
- Davis, C. A., and W. C. Lee, 2012: Mesoscale analysis of heavy rainfall episodes from SoWMEX/TiMREX. *J. Atmos. Sci.*, **69**, 521–537, <https://doi.org/10.1175/JAS-D-11-0120.1>.
- Dimet, F. Le, and O. Talagrand, 1986: Variational algorithms for analysis and assimilation of meteorological observations: theoretical aspects. *Tellus A*, **38 A**, 97–110, <https://doi.org/10.1111/j.1600-0870.1986.tb00459.x>.
- Do, P.-N., K.-S. Chung, P.-L. Lin, C.-Y. Ke, and S. M. Ellis, 2022: Assimilating Retrieved Water Vapor and Radar Data From NCAR S-PolKa: Performance and Validation Using Real Cases. *Mon. Weather Rev.*, 1177–1199, <https://doi.org/10.1175/mwr-d-21-0292.1>.
- Dowell, D. C., L. J. Wicker, and C. Snyder, 2011: Ensemble Kalman filter assimilation of radar observations of the 8 May 2003 Oklahoma city supercell: Influences of

- reflectivity observations on storm-scale analyses. *Mon. Weather Rev.*, **139**, 272–294, <https://doi.org/10.1175/2010MWR3438.1>.
- Dudhia, J., 1989: Numerical study of convection observed during the Winter Monsoon Experiment using a mesoscale two–dimensional model. *J. Atmos. Sci.*, **46**, 3077–3107.
- Ellis, S. M., and J. Vivekanandan, 2010: Water vapor estimates using simultaneous dual-wavelength radar observations. *Radio Sci.*, **45**, 1–15, <https://doi.org/10.1029/2009RS004280>.
- , and ———, 2011: Liquid water content estimates using simultaneous S and Ka band radar measurements. *Radio Sci.*, **46**, <https://doi.org/10.1029/2010RS004361>.
- Evensen, G., 1994: Sequential data assimilation with a nonlinear quasi-geostrophic model using Monte Carlo methods to forecast error statistics. *J. Geophys. Res.*, **99**, <https://doi.org/10.1029/94jc00572>.
- Fabry, F., and J. Sun, 2010: For how long should what data be assimilated for the mesoscale forecasting of convection and why? Part I: On the propagation of initial condition errors and their implications for data assimilation. *Mon. Weather Rev.*, **138**, 242–255, <https://doi.org/10.1175/2009MWR2883.1>.
- , and V. Meunier, 2020: Why are radar data so difficult to assimilate skillfully? *Mon. Weather Rev.*, **148**, 2819–2836, <https://doi.org/10.1175/MWR-D-19-0374.1>.
- Fabry, F., C. Frush, I. Zawadzki, and A. Kilambi, 1997: Extraction of near-surface index of refraction using radar phase measurements from ground targets. *IEEE Antennas Propag. Soc. AP-S Int. Symp.*, **4**, 2625–2628, <https://doi.org/10.1109/aps.1997.625552>.
- Feng, Y. C., and F. Fabry, 2018: Quantifying the error of radar-estimated refractivity by multiple elevation and dual-polarimetric data. *J. Atmos. Ocean. Technol.*, **35**, 1897–1911, <https://doi.org/10.1175/JTECH-D-18-0008.1>.
- , ———, and T. M. Weckwerth, 2016: Improving radar refractivity retrieval by considering the change in the refractivity profile and the varying altitudes of ground targets. *J. Atmos. Ocean. Technol.*, **33**, 989–1004, <https://doi.org/10.1175/JTECH-D-15-0224.1>.
- , H. W. Hsu, T. M. Weckwerth, P. L. Lin, Y. C. Liou, and T. C. C. Wang, 2021: The

- spatiotemporal characteristics of near-surface water vapor in a coastal region revealed from radar-derived refractivity. *Mon. Weather Rev.*, **149**, 2853–2874, <https://doi.org/10.1175/MWR-D-20-0425.1>.
- Gao, J., and D. J. Stensrud, 2014: Some observing system simulation experiments with a hybrid 3DEnVAR system for storm-scale radar data assimilation. *Mon. Weather Rev.*, **142**, 3326–3346, <https://doi.org/10.1175/MWR-D-14-00025.1>.
- , M. Xue, and D. J. Stensrud, 2013: The development of a hybrid 3DVAR-EnKF algorithm for storm-scale data assimilation. *Adv. Meteorol.*, **2013**, P7.4, <https://doi.org/https://doi.org/10.1155/2013/512656>.
- Gasperoni, N. A., M. Xue, R. D. Palmer, and J. Gao, 2013: Sensitivity of convective initiation prediction to near-surface moisture when assimilating radar refractivity: Impact tests using OSSEs. *J. Atmos. Ocean. Technol.*, **30**, 2281–2302, <https://doi.org/10.1175/JTECH-D-12-00038.1>.
- Ge, G., J. Gao, and M. Xue, 2013: Impacts of assimilating measurements of different state variables with a simulated supercell storm and three-dimensional variational method. *Mon. Weather Rev.*, **141**, 2759–2777, <https://doi.org/10.1175/MWR-D-12-00193.1>.
- Germann, U., and I. Zawadzki, 2002: Scale-dependence of the predictability of precipitation from continental radar images. Part I: Description of the methodology. *Mon. Weather Rev.*, **130**, 2859–2873, [https://doi.org/10.1175/1520-0493\(2002\)130<2859:SDOTPO>2.0.CO;2](https://doi.org/10.1175/1520-0493(2002)130<2859:SDOTPO>2.0.CO;2).
- , and ———, 2004: Scale dependence of the predictability of precipitation from continental radar images. Part II: Probability forecasts. *J. Appl. Meteorol.*, **43**, 74–89, [https://doi.org/10.1175/1520-0450\(2004\)043<0074:SDOTPO>2.0.CO;2](https://doi.org/10.1175/1520-0450(2004)043<0074:SDOTPO>2.0.CO;2).
- Grell, G. A., and D. Dévényi, 2002: A generalized approach to parameterizing convection combining ensemble and data assimilation techniques. *Geophys. Res. Lett.*, **29**, 10–13, <https://doi.org/10.1029/2002GL015311>.
- Ha, S. Y., and C. Snyder, 2014: Influence of surface observations in mesoscale data assimilation using an ensemble Kalman filter. *Mon. Weather Rev.*, **142**, 1489–1508, <https://doi.org/10.1175/MWR-D-13-00108.1>.
- Hamill, T. M., and C. Snyder, 2000: A hybrid ensemble Kalman filter-3D variational

- analysis scheme. *Mon. Weather Rev.*, **128**, 2905–2919, [https://doi.org/10.1175/1520-0493\(2000\)128<2905:ahekfv>2.0.co;2](https://doi.org/10.1175/1520-0493(2000)128<2905:ahekfv>2.0.co;2).
- Hanley, K. E., D. J. Kirshbaum, S. E. Belcher, N. M. Roberts, and G. Leoncini, 2011: Ensemble predictability of an isolated mountain thunderstorm in a high-resolution model. *Q. J. R. Meteorol. Soc.*, **137**, 2124–2137, <https://doi.org/10.1002/qj.877>.
- Hong, S. Y., Y. Noh, and J. Dudhia, 2006: A new vertical diffusion package with an explicit treatment of entrainment processes. *Mon. Weather Rev.*, **134**, 2318–2341, <https://doi.org/10.1175/MWR3199.1>.
- Houze, R. A., S. A. Rutledge, M. I. Biggerstaff, and B. F. Smull, 1989: Interpretation of Doppler weather radar displays of midlatitude mesoscale convective systems. *Bull. - Am. Meteorol. Soc.*, **70**, 608–619, [https://doi.org/10.1175/1520-0477\(1989\)070<0608:IODWRD>2.0.CO;2](https://doi.org/10.1175/1520-0477(1989)070<0608:IODWRD>2.0.CO;2).
- Hu, M., M. Xue, and K. Brewster, 2006: 3DVAR and cloud analysis with WSR-88D level-II data for the prediction of the Fort Worth, Texas, tornadic thunderstorms. Part I: Cloud analysis and its impact. *Mon. Weather Rev.*, **134**, 675–698, <https://doi.org/10.1175/MWR3092.1>.
- Hunt, B. R., E. J. Kostelich, and I. Szunyogh, 2007: Efficient data assimilation for spatiotemporal chaos: A local ensemble transform Kalman filter. *Phys. D Nonlinear Phenom.*, **230**, 112–126, <https://doi.org/10.1016/j.physd.2006.11.008>.
- Jacques, A. A., J. D. Horel, E. T. Crosman, and F. L. Vernon, 2017: Tracking mesoscale pressure perturbations using the USArray transportable array. *Mon. Weather Rev.*, **145**, 3119–3142, <https://doi.org/10.1175/MWR-D-16-0450.1>.
- Johnson, A., X. Wang, J. R. Carley, L. J. Wicker, and C. Karstens, 2015: A comparison of multiscale GSI-based EnKF and 3DVar data assimilation using radar and conventional observations for midlatitude convective-scale precipitation forecasts. *Mon. Weather Rev.*, **143**, 3087–3108, <https://doi.org/10.1175/MWR-D-14-00345.1>.
- Kawabata, T., T. Kuroda, H. Seko, and K. Saito, 2011: A cloud-resolving 4DVAR assimilation experiment for a local heavy rainfall event in the Tokyo metropolitan area. *Mon. Weather Rev.*, **139**, 1911–1931, <https://doi.org/10.1175/2011MWR3428.1>.
- Kong, R., M. Xue, and C. Liu, 2018: Development of a Hybrid En3DVar Data

Assimilation System and Comparisons with 3DVar and EnKF for Radar Data Assimilation with Observing System Simulation Experiments. *Mon. Weather Rev.*, **146**, 175–198, <https://doi.org/10.1175/MWR-D-17-0164.1>.

———, ———, ———, and Y. Jung, 2020: Comparisons of hybrid En3DVar with 3DVar and EnKF for radar data assimilation: Tests with the 10 may 2010 Oklahoma Tornado outbreak. *Mon. Weather Rev.*, **149**, 21–40, <https://doi.org/10.1175/MWR-D-20-0053.1>.

Lai, A., J. Gao, S. E. Koch, Y. Wang, S. Pan, A. O. Fierro, C. U. I. Chunguang, and M. I. N. Jinzhong, 2019: Assimilation of radar radial velocity, reflectivity, and pseudo-water vapor for convective-scale NWP in a variational framework. *Mon. Weather Rev.*, **147**, 2877–2900, <https://doi.org/10.1175/MWR-D-18-0403.1>.

Li, X., J. Ming, M. Xue, Y. Wang, and K. Zhao, 2015a: Implementation of a dynamic equation constraint based on the steady state momentum equations within the WRF hybrid ensemble-3DVar data assimilation system and test with radar T-TREC wind assimilation for tropical Cyclone Chanthu (2010). *J. Geophys. Res. Atmos.*, **120**, 4017–4039, <https://doi.org/10.1002/2014JD022706>.

Li, X., J. R. Mecikalski, J. Srikishen, B. Zavodsky, and W. A. Petersen, 2020: Assimilation of GPM Rain Rate Products With GSI Data Assimilation System for Heavy and Light Precipitation Events. *J. Adv. Model. Earth Syst.*, **12**, <https://doi.org/10.1029/2019MS001618>.

Li, Y., X. Wang Xuguang, and M. Xue, 2012: Assimilation of radar radial velocity data with the WRF hybrid ensemble-3dvar system for the prediction of hurricane Ike (2008). *Mon. Weather Rev.*, **140**, 3507–3524, <https://doi.org/10.1175/MWR-D-12-00043.1>.

Liebe, H. J., and N. Telecommunications, 1985: An updated model for millimeter wave propagation in moist air. **20**, 1069–1089.

Lindsey, D. T., D. Bikos, and L. Grasso, 2018: Using the GOES-16 split window difference to detect a boundary prior to cloud formation. *Bull. Am. Meteorol. Soc.*, **99**, 1541–1544, <https://doi.org/10.1175/BAMS-D-17-0141.1>.

Lindskog, M., K. Salonen, H. Järvinen, and D. B. Michelson, 2004: Doppler radar wind data assimilation with HIRLAM 3DVAR. *Mon. Weather Rev.*, **132**, 1081–1092,

[https://doi.org/10.1175/1520-0493\(2004\)132<1081:DRWDAW>2.0.CO;2](https://doi.org/10.1175/1520-0493(2004)132<1081:DRWDAW>2.0.CO;2).

Madaus, L. E., and G. J. Hakim, 2016: Observable surface anomalies preceding simulated isolated convective initiation. *Mon. Weather Rev.*, **144**, 2265–2284, <https://doi.org/10.1175/MWR-D-15-0332.1>.

Marshall, J. S., and W. M. Palmer, 1948: The distribution of raindrops with size. *J. Meteorol.*, **5**, 165–166.

Miyoshi, T., and Coauthors, 2016: Big data assimilation revolutionizing severe weather prediction. *Bull. Am. Meteorol. Soc.*, **97**, 1347–1354, <https://doi.org/10.1175/BAMS-D-15-00144.1>.

Mlawer, E. J., S. J. Taubman, P. D. Brown, M. J. Iacono, and S. A. Clough, 1997: Radiative transfer for inhomogeneous atmospheres: RRTM, a validated correlated-k model for the longwave. *J. Geophys. Res. Atmos.*, **102**, 16663–16682, <https://doi.org/10.1029/97jd00237>.

Montmerle, T., and C. Faccani, 2009: Mesoscale assimilation of radial velocities from Doppler radars in a preoperational framework. *Mon. Weather Rev.*, **137**, 1939–1953, <https://doi.org/10.1175/2008MWR2725.1>.

———, A. Caya, and I. Zawadzki, 2002: Short-term numerical forecasting of a shallow storms complex using bistatic and single-Doppler radar data. *Weather Forecast.*, **17**, 1211–1225, [https://doi.org/10.1175/1520-0434\(2002\)017<1211:STNFOA>2.0.CO;2](https://doi.org/10.1175/1520-0434(2002)017<1211:STNFOA>2.0.CO;2).

Pan, Y., and M. Wang, 2019: Impact of the Assimilation Frequency of Radar Data with the ARPS 3DVar and Cloud Analysis System on Forecasts of a Squall Line in Southern China. *Adv. Atmos. Sci.*, **36**, 160–172, <https://doi.org/10.1007/s00376-018-8087-5>.

———, ———, and M. Xue, 2020: Impacts of Humidity Adjustment Through Radar Data Assimilation Using Cloud Analysis on the Analysis and Prediction of a Squall Line in Southern China. *Earth Sp. Sci.*, **7**, 1–19, <https://doi.org/10.1029/2019EA000893>.

Roberts, N. M., and H. W. Lean, 2008: Scale-selective verification of rainfall accumulations from high-resolution forecasts of convective events. *Mon. Weather Rev.*, **136**, 78–97, <https://doi.org/10.1175/2007MWR2123.1>.

Sasaki, Y., 1958: An Objective Analysis Based on the Variational Method. *J. Meteorol.*

Soc. Japan. Ser. II, **36**, 77–88, https://doi.org/10.2151/jmsj1923.36.3_77.

- Shen, F., J. Min, and D. Xu, 2016: Assimilation of radar radial velocity data with the WRF Hybrid ETKF-3DVAR system for the prediction of Hurricane Ike (2008). *Atmos. Res.*, **169**, 127–138, <https://doi.org/10.1016/j.atmosres.2015.09.019>.
- , D. Xu, J. Min, Z. Chu, and X. Li, 2020: Assimilation of radar radial velocity data with the WRF hybrid 4DEnVar system for the prediction of hurricane Ike (2008). *Atmos. Res.*, **234**, 104771, <https://doi.org/10.1016/j.atmosres.2019.104771>.
- Snyder, C., and F. Zhang, 2003: Assimilation of simulated Doppler radar observations with an ensemble Kalman filter. *Mon. Weather Rev.*, **131**, 1663–1677, <https://doi.org/10.1175//2555.1>.
- Sugimoto, S., N. Andrew Crook, J. Sun, Q. Xiao, and D. M. Barker, 2009: An examination of WRF 3DVAR radar data assimilation on its capability in retrieving unobserved variables and forecasting precipitation through observing system simulation experiments. *Mon. Weather Rev.*, **137**, 4011–4029, <https://doi.org/10.1175/2009MWR2839.1>.
- Sun, J., 2006: Convective-scale assimilation of radar data: Progress and challenges. *Q. J. R. Meteorol. Soc.*, **131**, 3439–3463, <https://doi.org/10.1256/qj.05.149>.
- , and N. A. Crook, 1997a: Dynamical and microphysical retrieval from Doppler radar observations using a cloud model and its adjoint. Part II: Retrieval experiments of an observed Florida convective storm. *J. Atmos. Sci.*, **55**, 835–852, [https://doi.org/10.1175/1520-0469\(1998\)055<0835:DAMRFD>2.0.CO;2](https://doi.org/10.1175/1520-0469(1998)055<0835:DAMRFD>2.0.CO;2).
- , and ———, 1997b: Dynamical and microphysical retrieval from Doppler radar observations using a cloud model and its adjoint. Part I: Model development and simulated data experiments. *J. Atmos. Sci.*, **54**, 1642–1661, [https://doi.org/10.1175/1520-0469\(1997\)054<1642:DAMRFD>2.0.CO;2](https://doi.org/10.1175/1520-0469(1997)054<1642:DAMRFD>2.0.CO;2).
- Sun, J., and N. A. Crook, 2001: Real-time low-level wind and temperature analysis using single WSR-88D data. *Weather Forecast.*, **16**, 117–132, [https://doi.org/10.1175/1520-0434\(2001\)016<0117:RTLLWA>2.0.CO;2](https://doi.org/10.1175/1520-0434(2001)016<0117:RTLLWA>2.0.CO;2).
- Sun, J., and Y. Zhang, 2008: Analysis and prediction of a squall line observed during IHOP using multiple WSR-88D observations. *Mon. Weather Rev.*, **136**, 2364–2388, <https://doi.org/10.1175/2007MWR2205.1>.

- , and H. Wang, 2013: Radar data assimilation with WRF 4D-var. Part II: Comparison with 3D-var for a squall line over the U.S. great plains. *Mon. Weather Rev.*, **141**, 2245–2264, <https://doi.org/10.1175/MWR-D-12-00169.1>.
- , M. Chen, and Y. Wang, 2010: A frequent-updating analysis system based on radar, surface, and mesoscale model data for the Beijing 2008 forecast demonstration project. *Weather Forecast.*, **25**, 1715–1735, <https://doi.org/10.1175/2010WAF2222336.1>.
- , Y. Zhang, J. Ban, J. S. Hong, and C. Y. Lin, 2020: Impact of combined assimilation of radar and rainfall data on short-term heavy rainfall prediction: A case study. *Mon. Weather Rev.*, **148**, 2211–2232, <https://doi.org/10.1175/MWR-D-19-0337.1>.
- Tai, S. L., Y. C. Liou, J. Sun, S. F. Chang, and M. C. Kuo, 2011: Precipitation forecasting using Doppler radar data, a cloud model with adjoint, and the weather research and forecasting model: Real case studies during SoWMEX in Taiwan. *Weather Forecast.*, **26**, 975–992, <https://doi.org/10.1175/WAF-D-11-00019.1>.
- Tao, W. K., and Coauthors, 2003: Microphysics, radiation and surface processes in the Goddard Cumulus Ensemble (GCE) model. *Meteorol. Atmos. Phys.*, **82**, 97–137, <https://doi.org/10.1007/s00703-001-0594-7>.
- Thiruvengadam, P., J. Indu, and S. Ghosh, 2020: *Significance of 4DVAR Radar Data Assimilation in Weather Research and Forecast Model-Based Nowcasting System*. 0–3 pp.
- Tian, L., G. M. Heymsfield, L. Li, and R. C. Srivastava, 2007: Properties of light stratiform rain derived from 10- and 94-GHz airborne Doppler radars measurements. *J. Geophys. Res. Atmos.*, **112**, 1–12, <https://doi.org/10.1029/2006JD008144>.
- Tong, M., and M. Xue, 2005: Ensemble Kalman Filter Assimilation of Doppler Radar Data with a Compressible Nonhydrostatic Model: OSS Experiments. *Mon. Wea. Rev.*, 1789–1807.
- Tsai, C. C., and K. S. Chung, 2020: Sensitivities of quantitative precipitation forecasts for typhoon Soudelor (2015) near landfall to polarimetric radar data assimilation. *Remote Sens.*, **12**, 1–23, <https://doi.org/10.3390/rs12223711>.
- , S. C. Yang, and Y. C. Liou, 2014: Improving quantitative precipitation nowcasting with a local ensemble transform Kalman filter radar data assimilation system:

- Observing system simulation experiments. *Tellus, Ser. A Dyn. Meteorol. Oceanogr.*, **66**, <https://doi.org/10.3402/tellusa.v66.21804>.
- Wang, C., and Coauthors, 2021: Assimilation of X-Band Phased-Array Radar Data With EnKF for the Analysis and Warning Forecast of a Tornadic Storm. *J. Adv. Model. Earth Syst.*, **13**, 1–19, <https://doi.org/10.1029/2020MS002441>.
- Wang, H., J. Sun, S. Fan, and X. Y. Huang, 2013: Indirect assimilation of radar reflectivity with WRF 3D-var and its impact on prediction of four summertime convective events. *J. Appl. Meteorol. Climatol.*, **52**, 889–902, <https://doi.org/10.1175/JAMC-D-12-0120.1>.
- Wattrelot, E., O. Caumont, and J. F. Mahfouf, 2014: Operational implementation of the 1D13D-Var assimilation method of radar reflectivity data in the AROME model. *Mon. Weather Rev.*, **142**, 1852–1873, <https://doi.org/10.1175/MWR-D-13-00230.1>.
- Weckwerth, T. M., 2000: The effect of small-scale moisture variability on thunderstorm initiation. *Mon. Weather Rev.*, **128**, 4017–4030, [https://doi.org/10.1175/1520-0493\(2000\)129<4017:TEOSSM>2.0.CO;2](https://doi.org/10.1175/1520-0493(2000)129<4017:TEOSSM>2.0.CO;2).
- , C. R. Pettet, F. Fabry, S. Park, M. A. LeMone, and J. W. Wilson, 2005: Radar refractivity retrieval: Validation and application to short-term forecasting. *J. Appl. Meteorol.*, **44**, 285–300, <https://doi.org/10.1175/JAM-2204.1>.
- Wu, P.-Y., S.-C. Yang, C.-C. Tsai, and H.-W. Cheng, 2020: Convective-scale sampling error and its impact on the ensemble radar data assimilation system: A case study of heavy rainfall event on 16th June 2008 in Taiwan. *Mon. Weather Rev.*, 3631–3652, <https://doi.org/10.1175/mwr-d-19-0319.1>.
- Wulfmeyer, V., P. Di Girolamo, P. Schlüssel, J. Van Baelen, and F. Zus, 2015: Reviews of Geophysics of water and energy cycles. *Rev. Geophys.*, 819–895, <https://doi.org/10.1002/2014RG000476>.Received.
- Xiao, Q., and J. Sun, 2007: Multiple-radar data assimilation and short-range quantitative precipitation forecasting of a squall line observed during IHOP_2002. *Mon. Weather Rev.*, **135**, 3381–3404, <https://doi.org/10.1175/MWR3471.1>.
- , Y. H. Kuo, J. Sun, W. C. Lee, E. Lim, Y. R. Guo, and D. M. Barker, 2005: Assimilation of Doppler radar observations with a regional 3DVAR system: Impact of Doppler velocities on forecasts of a heavy rainfall case. *J. Appl. Meteorol.*, **44**,

768–788, <https://doi.org/10.1175/JAM2248.1>.

- Yang, S. C., M. Corazza, A. Carrassi, E. Kalnay, and T. Miyoshi, 2009: Comparison of local ensemble transform Kalman filter, 3DVAR, and 4DVAR in a quasigeostrophic model. *Mon. Weather Rev.*, **137**, 693–709, <https://doi.org/10.1175/2008MWR2396.1>.
- , Z. M. Huang, C. Y. Huang, C. C. Tsai, and T. K. Yeh, 2020: A case study on the impact of ensemble data assimilation with GNSS-zenith total delay and radar data on heavy rainfall prediction. *Mon. Weather Rev.*, **148**, 1075–1098, <https://doi.org/10.1175/MWR-D-18-0418.1>.
- Yokota, S., H. Seko, M. Kunii, H. Yamauchi, and E. Sato, 2018: Improving Short-Term Rainfall Forecasts by Assimilating Weather Radar Reflectivity Using Additive Ensemble Perturbations. *J. Geophys. Res. Atmos.*, **123**, 9047–9062, <https://doi.org/10.1029/2018JD028723>.
- Yoneyama, K., C. Zhang, and C. N. Long, 2013: Tracking pulses of the Madden-Julian oscillation. *Bull. Am. Meteorol. Soc.*, **94**, 1871–1891, <https://doi.org/10.1175/BAMS-D-12-00157.1>.
- Yussouf, N., and D. J. Stensrud, 2010: Impact of phased-array radar observations over a short assimilation period: Observing system simulation experiments using an ensemble Kalman filter. *Mon. Weather Rev.*, **138**, 517–538, <https://doi.org/10.1175/2009MWR2925.1>.
- Zhang, F., C. Snyder, and J. Sun, 2004: Impacts of initial estimate and observation availability on convective-scale data assimilation with an ensemble Kalman filter. *Mon. Weather Rev.*, **132**, 1238–1253, [https://doi.org/10.1175/1520-0493\(2004\)132<1238:IOIEAO>2.0.CO;2](https://doi.org/10.1175/1520-0493(2004)132<1238:IOIEAO>2.0.CO;2).
- Zhao, K., X. Li, M. Xue, B. J. D. Jou, and W. C. Lee, 2012: Short-term forecasting through intermittent assimilation of data from Taiwan and mainland China coastal radars for Typhoon Meranti (2010) at landfall. *J. Geophys. Res. Atmos.*, **117**, 1–20, <https://doi.org/10.1029/2011JD017109>.
- Zhu, L., Y. Bao, G. P. Petropoulos, P. Zhang, F. Lu, Q. Lu, Y. Wu, and D. Xu, 2020: Temperature and humidity profiles retrieval in a plain area from Fengyun-3D/HIRAS sensor using a 1D-VAR assimilation scheme. *Remote Sens.*, **12**, 1–20,

<https://doi.org/10.3390/rs12030435>.

Zuluaga, M. D., and R. A. Houze, 2013: Evolution of the population of precipitating convective systems over the equatorial Indian ocean in active phases of the Madden-Julian oscillation. *J. Atmos. Sci.*, **70**, 2713–2725, <https://doi.org/10.1175/JAS-D-12-0311.1>.